AD

AD 748424

FUNDAMENTAL STUDIES OF SEMICONDUCTOR HETEROEPITAXY

FOURTH SEMIANNUAL REPORT

R. P. Ruth, A. J. Hughes, J. L. Kenty, H. M. Manasevit
and A. C. Thorsen

Distribution of this document
is unlimited.

D D C

RECEIVED

SEP 15 1972

B

128

DOCUMENT CONTROL DATA - R & D

(Security classification of title, body of abstract and indexing annotation must be entered when the overall report is classified)

1. ORIGINATING ACTIVITY *(Corporate author)*	2a. REPORT SECURITY CLASSIFICATION
North American Rockwell Corp, Electronics Group Research and Technology Division Anaheim, California	Unclassified
	2b. GROUP

3. REPORT TITLE

Fundamental Studies of Semiconductor Heteroepitaxy

4. DESCRIPTIVE NOTES *(Type of report and inclusive dates)*

Semiannual Report, January 1972 through June 1972

5. AUTHOR(S) *(First name, middle initial, last name)*

Ralph P. Ruth, A. James Hughes, Joseph L. Kenty, Harold M Manasevit, Arthur C. Thorsen

6. REPORT DATE	7a. TOTAL NO. OF PAGES	7b. NO. OF REFS
July 1972	118	25 + 8 (Appendix)

8a. CONTRACT OR GRANT NO.	9a. ORIGINATOR'S REPORT NUMBER(S)
DAAH01-70-C-1311	
b. PROJECT NO.	C71-86.4/501
c.	9b. OTHER REPORT NO(S) *(Any other numbers that may be assigned this report)*
d.	

10. DISTRIBUTION STATEMENT

Distribution of this document is unlimited.

Details of illustrations in this document may be better studied on microfiche

11. SUPPLEMENTARY NOTES	12. SPONSORING MILITARY ACTIVITY
	Advanced Research Projects Agency, ARPA Order No. 1585 Washington, D.C.

13. ABSTRACT

Theoretical studies have been devoted to three main areas: (1) The Si/Al_2O_3 system has been modeled by means of interatomic Morse potentials and computer simulation, with only anion-anion and cation-anion potentials used for the Al_2O_3. (2) The electron-on-network technique has been used to calculate work functions and surface double-layer potentials of monovalent metals. (3) Theoretically calculated changes in mobility and resistivity in the plane of the film in the Si/Al_2O_3 system caused by stress effects arising at the interface due to differential thermal contraction and to the piezoresistance effect are in excellent agreement with experimental results. Theoretical formulas have been developed for Si and Ge and for Al_2O_3 and $MgAl_2O_4$ substrates, for a variety of crystallographic orientations. Experimental studies have been concentrated in the (221) $Si/(11\bar{2}2)$ Al_2O_3 and the (100) $Si/(01\bar{1}2)$ Al_2O_3 systems. The mobility anisotropy factor was found to be about 39 percent for the (221) plane and about 9 percent for the (100) plane. Results indicate that (221) Si probably exhibits higher electron mobilities than other more commonly used orientations.

Attempts have continued to optimize the Si deposition process for growth on $\sim(11\bar{2}0)$ and $(01\bar{1}2)$ Al_2O_3 surfaces. The effects of post-nucleation annealing have been examined, but no significant improvement in Si film quality has been demonstrated. The effects on film growth of gas-phase etching of Al_2O_3 surfaces prior to deposition have been evaluated further. No significant advantage to the Si growth process has been observed to result from cooled reactor chamber walls in the vertical systems used in this work.

Additional reactant analyses have been carried out by mass spectrometric techniques, with significantly impurity concentrations found in some of the reactants (especially SiH_4).

DD FORM 1473 *I NOV 65*

13. ABSTRACT (Cont)

Study of the chemistry and reaction kinetics of CVD processes used for growing Si and GaAs films in heteroepitaxial systems has been initiated.

Evaluation of polishing methods for $MgAl_2O_4$ surfaces has indicated that surface fill-in occurs for this material just as for Al_2O_3; gas-phase etching experiments have been initiated. N-type Si films with electrical properties at least as good as those grown on Al_2O_3 have been obtained on Czochralski-grown stoichiometric $MgAl_2O_4$ when He-H_2 gas mixtures are used for the growth environment; autodoping appears to be operative in the $Si/MgAl_2O_4$ system (in He-H_2 atmospheres) at approximately the same temperatures as for Si/Al_2O_3.

Ion-beam sputtering techniques have been developed for preparing ultra-thin ($\sim$200Å) Al_2O_3 wafers of (0001), ($10\bar{1}4$), and ($01\bar{1}2$) orientations as substrates in the _in situ_ CVD experiments with Si. Fabrication of the modified-design CVD microchamber is essentially complete. Numerous in situ PVD experiments have been carried out with Al and Au deposited onto amorphous carbon substrates to delineate experimental techniques required for the CVD experiments. Unusual nucleation effects were observed in Au films exposed to the electron beam.

The variation of the electrical properties of Si/Al_2O_3 with temperature has been studied; some effects attributed to high defect densities or inhomogeneous strains were observed. Photoelectric effects in the Si/Al_2O_3 system were studied further, verifying that the observed phenomena result from photoinjection of electrons from metal films into the Al_2O_3. The work functions of several metals and the heights of the metal-Al_2O_3 interface barriers were determined. High-field transport properties of heteroepitaxial films have been continued.

Work on the determination of carrier lifetimes using the MOS pulsed-capacitance technique and the fabrication of Schottky-barrier FET's in $GaAs/Al_2O_3$ has continued. An analysis was made to evaluate the effect of the impurity redistribution in the Si in the region near the oxide interface on the interpretation of lifetime data obtained by the MOS technique.

A summary of the work planned for the next six months is included.

AD

FUNDAMENTAL STUDIES OF SEMICONDUCTOR HETEROEPITAXY

FOURTH SEMIANNUAL REPORT

R. P. Ruth, A. J. Hughes, J. L. Kenty, H. M. Manasevit
and A. C. Thorsen

Research and Technology Division

Electronics Group

North American Rockwell Corporation

July 1972

Distribution of this document
is unlimited.

iik

ABSTRACT

The objective of this program is to carry out a fundamental study of nucleation and film growth mechanisms in heteroepitaxial semiconductor thin films, and to apply the results to the preparation of improved films and thin-film devices on insulating substrates. Both theoretical and experimental investigations are involved, with emphasis on chemical vapor deposition (CVD) techniques applied to the Si-on-Al_2O_3, Si-on-$MgAl_2O_4$, and GaAs-on-Al_2O_3 systems. The accomplishments of the fourth six-month period are described in terms of seven program subtasks.

Theoretical studies have been devoted to three main areas: (1) The Si/Al_2O_3 system has been modeled by means of interatomic Morse potentials and computer simulation, with only anion-anion and cation-anion potentials used for the Al_2O_3 and chosen to conform to constraints of the physical lattice. Investigation of surface reconstruction in basal-plane Al_2O_3 has also been initiated, using these potentials. (2) The electron-on-network technique has been used to calculate work functions and surface double-layer potentials of monovalent metals. (3) Theoretically calculated changes in mobility and resistivity in the plane of the film in the Si/Al_2O_3 system caused by stress effects arising at the interface due to differential thermal contraction and to the piezoresistance effect are in excellent agreement with experimental results. Theoretical formulas have been developed for Si and Ge and for Al_2O_3 and $MgAl_2O_4$ substrates, for a variety of crystallographic orientations.

The experimental studies of anisotropy of electrical properties have been concentrated in the (221)Si/$(11\bar{2}2)$$Al_2O_3$ and the (100) Si/$(01\bar{1}2)$$Al_2O_3$ systems. The mobility anisotropy factor A (defined as the ratio of the difference between the maximum and minimum values of carrier mobility in the plane of the film to the average value of the mobility in that plane) was found to be about 39 percent for the (221) plane and about 9 percent for the (100) plane. The calculations and experimental results indicate that (221) Si probably exhibits higher electron mobilities than other more commonly used orientations.

Attempts have continued to optimize the Si deposition process for growth on $\sim(11\bar{2}0)$ and $(01\bar{1}2)$ Al_2O_3 surfaces. The effects of post-nucleation annealing have been examined, but no significant improvement in Si film quality has been demonstrated. The effects on film growth of gas-phase etching of Al_2O_3 surfaces prior to deposition have been evaluated further. No significant advantage to the Si growth process has been observed to result from cooled reactor chamber walls in the vertical systems used in this work. Additional reactant analyses have been carried out by mass spectrometric techniques, with significant impurity concentrations found in some of the reactants (especially SiH_4). Study of the chemistry and reaction kinetics of CVD processes used for growing Si and GaAs films in heteroepitaxial systems has been initiated; the first experiments undertaken are directed toward determining the role of the Al_2O_3 surface in catalyzing the pyrolysis of SiH_4.

Evaluation of polishing methods for $MgAl_2O_4$ surfaces has indicated that surface fill-in occurs for this material just as for Al_2O_3. Gas-phase etching experiments with $MgAl_2O_4$ surfaces have been initiated. N-type Si films with electrical properties at least as good as those grown on Al_2O_3 can be obtained on Czochralski-grown stoichiometric spinel ($MgAl_2O_4$) when He-H_2 gas mixtures are used for the growth environment; autodoping appears to be operative in the Si/$MgAl_2O_4$ system (in He-H_2 atmospheres) at approximately the same temperatures as for Si/Al_2O_3.

Ion-beam sputtering techniques have been developed for preparing ultra-thin ($\sim$200 Å) $A\ell_2O_3$ wafers for use as substrates in the in situ CVD experiments with Si. Wafers of (0001), (10$\bar{1}$4), and (01$\bar{1}$2) orientations thinned to $\sim$0.002 in. by mechanical polishing techniques have been subsequently thinned by ion etching to the point of perforation in some areas, resulting in adjoining regions of thicknesses suitable for transmission electron microscopy. Fabrication of the modified-design CVD micro-chamber is essentially complete, with testing and the first CVD in situ experiments planned for early in the third year. Numerous in situ PVD experiments have been carried out with $A\ell$ and Au deposited onto amorphous carbon substrates to delineate experimental techniques and problems to be encountered in the CVD experiments. Unusual nucleation effects were observed in those portions of the Au films exposed to the electron beam.

The variation of the electrical properties of $Si/A\ell_2O_3$ with temperature has been studied; some effects attributed to high defect densities or inhomogeneous strains were observed. Photoelectric effects in the $Si/A\ell_2O_3$ system were studied further, verifying that the observed phenomena do result from photoinjection of electrons from metal films into the $A\ell_2O_3$. The work functions of several metals and the heights of the metal-$A\ell_2O_3$ interface barriers were determined. The high-field transport properties of heteroepitaxial films have been further studied.

The device effort has centered about the determination of carrier lifetimes using the MOS pulsed-capacitance technique and attempts to fabricate Schottky-barrier FET's in $GaAs/A\ell_2O_3$. An analysis was made to evaluate the effect of the impurity redistribution in the Si in the region near the oxide interface on the interpretation of lifetime data obtained by the MOS technique.

A summary of the work planned for the next six months is included.

CONTENTS

ILLUSTRATIONS

SECTION I

INTRODUCTION

This is the fourth Semiannual Technical Report for this contract. It describes work carried out during the period 1 January – 30 June 1972. Earlier semiannual reports (Refs 1-3) described work done in the first 18 months of the program.

1. PROGRAM OBJECTIVES

The overall objective of the program, unchanged from that originally proposed, is to carry out a fundamental study of the nucleation and film growth mechanisms in heteroepitaxial semiconductor thin films, leading to new knowledge and understanding of these processes, and then to apply these results to the preparation of improved semiconductor thin films and thin-film devices on insulating substrates.

The specific technical objectives of the three-year program are the following:

1. Investigation of the many aspects of the mechanisms of heteroepitaxial film growth, to establish (through accumulation of basic knowledge) sets of technical guidelines for the preparation of better films which can then be applied to real situations.

2. Preparation of improved, high-quality, device-grade heteroepitaxial films of Si and GaAs on insulating substrates by chemical vapor deposition (CVD) methods.

3. Development of methods of characterizing heteroepitaxial films as to their suitability for subsequent device fabrication.

4. Design and fabrication of selected thin-film devices which take advantage of the unique properties of such films.

The general plan for accomplishing these objectives involves as the primary effort the study of the fundamentals of heteroepitaxial semiconductor film growth on insulating substrates. Specialized device fabrication is used both as a means of evaluating certain properties of the films (and thus as a measure of film quality as the program progresses) and as a means of exploiting certain unique properties of heteroepitaxial semiconductor-insulator systems. The determination of which fundamental mechanisms, properties, and processes to investigate is based on extensive background knowledge of epitaxy and its problems and from the thin-film device difficulties encountered over a period of several years in many laboratories.

The problems studied are in no way restricted to those identified a priori; experimental (and theoretical) attention can be shifted as the program progresses in order to achieve the goal of a better understanding of heteroepitaxial processes and the resultant improvement in thin-film active semiconductor devices.

1

2. PROGRAM SCOPE

The program involves both theoretical and experimental investigation of the nucleation and growth mechanisms of heteroepitaxial films in semiconductor-insulator systems, the development of improved techniques for preparation of heteroepitaxial semiconductor films, and the fabrication of some devices utilizing these films, the latter primarily for the purpose of evaluating the heteroepitaxial film materials but also to exploit the special properties of the films.

The theoretical studies consist of two types of activity. First, there is direct interaction with the experimental program involving data analyses, suggestion of definitive experiments, and postulation of specific models to explain experimental observations. Second, there is development of original contributions to the theory of heteroepitaxial growth, the goal of which is the generation of significant advances in fundamental epitaxy theory.

The experimental investigations are also of two types. First, fundamental explorations are carried out to delineate mechanisms and general empirical principles of the heteroepitaxial growth process. Second, practical studies accompany the fundamental investigations so that useful developments can be immediately applied to the improvement of semiconductor films and thin-film devices on insulating substrates.

The work has emphasized the CVD method of growing semiconductor thin films because of its importance in the semiconductor industry. One of the unique aspects of the program is this emphasis on the study of fundamental mechanisms of CVD growth; most previous fundamental studies of epitaxy have concentrated upon physical vapor deposition (PVD) methods, partly because such studies are easier with PVD techniques.

The program emphasis is on films of Si and GaAs and substrates of sapphire (Al_2O_3) and spinel ($MgAl_2O_4$); nonstoichiometric spinel and beryllia (BeO) may also be included as substrate materials later in the program. The initial emphasis has been on the Si-on-Al_2O_3 system, with increasing attention being given to the Si-on-$MgAl_2O_4$ and GaAs-on-Al_2O_3 systems. Si and GaAs have been chosen because of the preeminence of the former in the semiconductor industry and the high-frequency and high-temperature attributes of the latter; in addition, they represent the elemental and compound semiconductors for which most comparative information exists.

The program as described is carried on primarily at facilities of the Electronics Group of North American Rockwell Corporation (NR) by NR personnel. Parts of several of the subtasks are performed by personnel of the University of California at Los Angeles (UCLA), in the Department of Electrical Sciences and Engineering and in the Chemistry Department. In addition, work on one of the subtasks is being done in part in the Department of Chemistry of California State University, San Diego (CSUSD). Both the ULCA and the CSUSD programs are supported by subcontracts from NR.

2

3. PROGRAM DESCRIPTION BY SUBTASK

The three-year program was originally divided into nine subtasks - two theoretical and seven experimental (Refs 1, 2). However, at the start of the second year it was decided that, on the basis of the way in which the work of the first twelve months had developed, the contract work would be more accurately described in terms of seven main subtasks - one theoretical and six experimental.

The seven subtasks are as follows:

Subtask 1: Theory of Epitaxy and Heteroepitaxial Interfaces. Theoretical examination of CVD kinetics and the processes of nucleation, surface migration, and film growth with emphasis on crystallographic relationships between overgrowth and substrate to attempt to identify mechanisms and establish general principles of heteroepitaxial growth; theoretical modeling of the heteroepitaxial interface using appropriate potentials to determine surface configurations and interfacial binding energies in real and/or simplified systems.

Subtask 2: Deposition Studies and Film Preparation. Investigation of the effects of various experimental parameters upon the properties of deposited semiconductor films; investigation of the delivery kinetics of CVD processes, to improve the detailed understanding and control of the chemical reactions involved in the preparation of heteroepitaxial semiconductor films by CVD; preparation of films for use in other parts of the program.

Subtask 3: Analysis and Purification of CVD Reactants. Analysis of impurity content of reactant materials used in metalorganic-hydride and other CVD processes; preparation of research-sample quantities of improved-purity reactants for use in film growth experiments.

Subtask 4: Preparation and Characterization of Substrates. Preparation of substrate wafers and characterization of surfaces and impurity content of substrates used for semiconductor heteroepitaxy; development of reproducible new and/or improved substrate polishing, cleaning, and handling methods.

Subtask 5: Studies of in situ Film Growth in the Electron Microscope. In situ observation and study of the early stages of growth of CVD films in the electron microscope, to develop additional fundamental knowledge of the epitaxy process. Results of these experimental observations will be incorporated into the theoretical studies wherever possible.

Subtask 6: Evaluation of Film Properties. Measurement of the electrical, optical, crystallographic, and thermal properties of heteroepitaxial semiconductor films on insulators, by a variety of measurement techniques. Standard techniques will be employed and new methods developed where required for measurement of those film properties which appear best to characterize ultimate device performance.

3

Subtask 7: Design and Fabrication of Devices. Design and experimental fabrication of certain types of devices, using heteroepitaxial films produced in the above studies. Some devices will be used to evaluate material properties and others to exploit semiconductor film characteristics unique to heteroepitaxial systems.

These subtasks will be modified as needed as the program progresses.

The results obtained during the fourth six-month period of the contract are discussed by subtask in Section II. An outline of the work planned for the next six months is contained in Section III. A program summary to date is given in Section IV.

Appendix I contains a pre-publication version of a paper based on theoretical studies at UCLA which were supported in part by this contract, as part of the effort on Subtask 1.

SECTION II

RESULTS AND DISCUSSION

The work of the fourth six-month period of the contract is discussed in this section. The effort of each of the seven subtasks is described separately. Because of the interrelationships among the various subtasks the discussion in several instances necessarily involves activities and results which primarily are part of another subtask.

1. SUBTASK 1. THEORY OF EPITAXY AND HETEROEPITAXIAL INTERFACES

Several possible approaches to the theoretical modeling of heteroepitaxial systems have been investigated to date under this contract. The general criteria originally adopted for determining suitability of a given technique are that the theoretical treatment and associated calculations should (1) relate explicitly to heteroepitaxy; (2) be as nearly as possible a "first-principles" approach; (3) relate as closely as possible to an actual system such as $Si/A\ell_2O_3$; and (4) represent an original contribution to the theory of heteroepitaxy.

Attempting to meet these criteria is both difficult and ambitious. However, the criteria are important in providing a general framework and goals for the theoretical studies. Although the $Si/A\ell_2O_3$ system is of considerable commercial and practical importance, theories and calculations available in the literature fall drastically short in that there is no real connection with systems such as $Si/A\ell_2O_3$. The emphasis of previous theories has instead been on simple and unrealistic one- or two-dimensional cubic lattices which unfortunately cannot be applied to $Si/A\ell_2O_3$. The intent of the theoretical studies of this contract is thus to develop an approach which relates specifically to the Si and the $A\ell_2O_3$ lattices.

During the first year of the contract a formal theoretical method of replacing overgrowth atoms on a substrate with Gaussian mass distributions was further developed for those cases where the effective interatomic potential is known. The technique, applicable to irregular-shaped islands or films of finite extent, was applied to a simplified model to determine preferred orientation relationships from calculated film-substrate interaction energies. The method was not pursued further, however, because it was not sufficiently adaptable to real systems. Several other possible approaches to the theoretical modeling of heteroepitaxial systems were critically reviewed, including the Frank-Van der Merwe model, a Green's function/ Wannier-function approach, a contrived potential-energy model, and the two-body interatomic potential method. It was concluded at that time that most existing theories are inadequate for application to real systems.

The feasibility of a molecular orbital development of the heteroepitaxial interface was then investigated. However, early in the second year it was determined infeasible to apply this technique in a manner directly relevant to heteroepitaxy, so this effort was terminated. The interatomic potential approach to heteroepitaxy was then re-instigated, with the goal being the computer simulation of growth of Si on $A\ell_2O_3$. Mechanical stability conditions for an $A\ell_2O_3$ lattice modeled with two-body potentials were investigated and determined to the depth required for these applications. Computer programming of the $A\ell_2O_3$ lattice energy and elastic constants was begun for use in determining appropriate empirical potentials required for modeling this

lattice. Successful modeling of the Al_2O_3 lattice is a major requirement for modeling Si growth on Al_2O_3.

In addition, during the first half of the second year the application of the electron-on-network theory to the problem of determining surface configurations and interfacial binding energies in heteroepitaxial systems where the surface structure is allowed to relax was investigated and initially appeared promising for real systems of interest. Normalized eigenvectors were developed as a basis for a secular equation whose solution is fundamental to the solution of the total problem.

During the past six months, the theoretical studies at NR and UCLA have been devoted to three main areas: (1) modeling of the Si/Al_2O_3 system by means of interatomic potentials and computer simulation; (2) use of the electron-on-network technique to calculate work functions and surface double-layer potentials of mono-valent metals; and (3) calculations relating the mobility of Si films on Al_2O_3 to stress effects arising at the heteroepitaxial interface and caused by the differential thermal contraction of film and substrate. These investigations will be discussed in sequence in this section.

a. Studies of the Si/Al_2O_3 System Using Interatomic Potentials

It now appears that a general solution to the heteroepitaxial Si/Al_2O_3 problem cannot be hoped for at this time and may indeed be several years in the future. What can be done is to incorporate the geometrical and structural features of the Si and Al_2O_3 crystal lattices into a simplified model based on interatomic potential modeling of Si and of Al_2O_3. This should represent a reasonable way of incorporating those structural features of Si growth on Al_2O_3 which are caused by the Al_2O_3 lattice.

In using interatomic potentials to represent the interaction between atoms in the Si/Al_2O_3 system, the cohesive energy of a given configuration is obtained by summing over all interaction atom pairs. As background, a few comments on the theoretical foundations of interatomic potentials will be included here.

The concept of an interatomic potential in the present context is best regarded as a phenomenological construct. While there are quantum mechanical foundations which provide a basis for interatomic potentials at the philosophical or qualitative level, there do not appear to be any quantitative and rigorous calculations of interatomic potentials, with the possible exception of the case of Na. Even if rigorous atomic potentials existed and were available for the bulk "perfect-crystal" materials of interest, these potentials would be specific to the bulk crystal and would have to be altered in the presence of defects or at a heteroepitaxial interface.

For interatomic potentials to be useful in practice it is necessary to assume that the basic interatomic interaction is unaffected by atomic rearrangement. This assumption is therefore fundamental in the present studies. A second consideration lies in the particular type of potential to be employed. These investigations assume a simple two-body central-force interaction between atoms. More complicated non-central potentials could be employed, in principle, but in practice they are out of the question, particularly for the complicated Al_2O_3 lattice. In this work the atomic potential modeling of Si and Al_2O_3 is regarded simply as a phenomenological treatment.

6

There are two attractive features which argue for application of atomic potentials to the Si/Al_2O_3 system: (1) Computer modeling with interatomic potentials has apparently been successful in the past for structural problems in simple metals. (2) There is at present no theory of epitaxy which makes it possible to predict the orientation of the overgrowth on the substrate in the Si/Al_2O_3 system. The orientation aspects of heteroepitaxy can be treated fairly directly in terms of interatomic potentials.

The theoretical modeling of the Si/Al_2O_3 system with interatomic potentials can be divided into five parts: (1) the modeling of the Al_2O_3 lattice by determination of phenomenological potentials meeting appropriate criteria or constraints; (2) the investigation of Al_2O_3 surface reconstruction on the basis of the determined potentials; (3) modeling of the Si lattice with an interatomic potential; (4) the parameterization, in lieu of useful empirical data, of the Si/Al_2O_3 adatom interaction; and (5) the simulation of Si growth on Al_2O_3 by computer computation of energy for small clusters of Si atoms.

The modeling of the Al_2O_3 lattice has been carried out in terms of Morse potentials. This choice was suggested by the following factors: (1) The Si is to be modeled by means of a Morse potential available in the literature (Ref 4). (2) The Si/Al_2O_3 adatom potential, which is to be treated essentially as a parameter, can be conveniently expressed with Morse potentials. (3) Analytical expressions for the atomic force can be easily obtained for Morse potentials.

Al_2O_3, which has two types of atoms, would in general require three Morse potentials:

1. $D_{CC} \{\exp(-2 \alpha_{CC}(R-R_{CC})) - 2\exp(-\alpha_{CC}(R-R_{CC}))\}$

2. $D_{AC} \{\exp(-2 \alpha_{AC}(R-R_{AC})) - 2\exp(-\alpha_{AC}(R-R_{AC}))\}$

3. $D_{AA} \{\exp(-2 \alpha_{AA}(R-R_{AA})) - 2\exp(-\alpha_{AA}(R-R_{AA}))\}$

The subscripts CC, AC, and AA denote cation-cation, anion-cation and anion-anion interactions, respectively. A general determination of these three interatomic potentials would require treatment of a nine-parameter system. A straightforward determination is therefore impractical. It thus becomes important to incorporate as much physical and empirical data as possible in order to simplify the problem.

The appropriate cohesive energy (energy of formation), elastic constants, and lattice parameters are known experimentally. Gieske and Barsch (Ref 5), in considering the elastic constants, have noted that Al_2O_3 is somewhat unusual compared with other oxides such as MgO in that the Cauchy relations $C_{12}=C_{16}$ and $C_{23}=C_{44}$ are approximately fulfilled. In addition, although Al_2O_3 is trigonal (rhombohedral), the second-order elastic constant data indicate that the deviation from pure hexagonal symmetry ($C_{14}=0$) is small. (C_{14} is about an order of magnitude smaller than the other elastic constants.) This suggests that the elastic properties are related primarily to the nearly-hcp oxygen framework.

Anderson (Ref 6) earlier expressed this same point of view - that the oxygen framework is dominant in determining elastic properties of this oxide. Since the Al atom sites in Al_2O_3 are believed to play an important role in heteroepitaxial

film-substrate orientation, a model based solely on anion-anion interactions would not be reasonable. Intuitively, the deviation from hcp symmetry would be exhibited most strongly through the cation-cation interaction, which relates explicitly to a non-hexagonal lattice with defects. It is therefore concluded that the cation-cation interactions do not play an important role in the lattice and that the exclusion of cation-cation interactions is a reasonable and important simplification. Consequently, only anion-anion and cation-anion potentials have been employed throughout the modeling.

The phenomenological potentials have been determined by requiring that the modeled lattice provide (1) the correct cohesive energy of about 34.54 eV per rhombohedral unit cell; (2) that the lattice energy be a local maximum and the derivative vanish at the observed lattice spacing; (3) that the forces on each of the cations in the unit cell vanish; and (4) that the forces on each of the anions in the unit cell also vanish.

Potentials meeting these four constraints have been determined. To facilitate more detailed discussion of the procedure used in establishing these potentials the first few interatomic distances in the Al_2O_3 lattice (anion-anion, cation-anion, and cation-cation distances) are given in Table I. The first four anion-anion distances and the first two cation-anion distances relate to what would be first-neighbor interactions in an idealized Al_2O_3 lattice.

TABLE I.
Interatomic Distances for Al_2O_3 Lattice (Å)

Anion-Anion	Cation-Anion	Cation-Cation
2.524	1.857	2.649
2.619	1.969	2.792
2.725		3.222
2.869	3.223	3.499
	3.430	3.843
3.790	3.560	4.762
3.957	3.862	5.148
4.334	4.162	5.449
	4.325	
4.616	4.380	
4.762	4.429	
4.813	4.675	
4.945	5.064	
5.072	----	
----	5.244	
5.128	5.366	
5.252		

As a first attempt, only the four first-neighbor anion-anion and two first-neighbor cation-anion interactions were included in the analytical expression for cation and anion forces. Potentials were determined which gave the required zero forces. However, examination of the derivative of the cell energy showed that a

maximum could never be obtained with only first neighbors. All subsequent discussion therefore relates to a model including 13 different anion-anion separations (up to 5.072 Å) and 12 different cation-anion separations (up to 5.064 Å). This cutoff point in the model is arbitrary but is believed to be reasonable for present purposes.

Potentials meeting the four constraints and including the interactions listed above were then determined for a range of values of the potential parameters R_{AC} and R_{AA}. It was originally planned that the remaining parameters R_{AC} and R_{AA} would be further restricted by calculation of elastic constants. The $A\ell_2O_3$ lattice, viewed as rhombohedral, contains 10 atoms per unit cell and involves internal (unequal) displacements or strains of the various atoms in the unit cell. The accurate calculation of elastic constants is an extremely involved task in the case of internal displacements. A calculation could be made in the approximation which neglects internal strain, and this was begun. Subsequent considerations indicated that such a procedure is regarded as providing only an order-of-magnitude estimate. Therefore, elastic constant calculations have not been pursued further, since they would divert the effort from the main task as related to heteroepitaxy.

One aspect of the use of elastic constant data should, however, be discussed. In interatomic potential calculations for simple cubic metals, as found in the literature, the calculation of elastic constants and the requirement that the strain energy be positive-definite is usually imposed for lattice stability. In such cases this is an important constraint, because the force on an atom vanishes identically due to lattice symmetry and therefore imposes no constraint at all in determining an appropriate potential. The $A\ell_2O_3$ lattice is, perforce, unstable unless the potentials are determined such that the required forces are zero.

As mentioned above, potentials for $A\ell_2O_3$ have been determined for a range of values of the parameters R_{AC} and R_{AA}. On general grounds and from examination of the constraint analytical expressions, it appears that R_{AA} and R_{AC} both would lie in the range of 1.969 Å $\leq R_{AA}$ and $R_{AC} \leq 2.524$ Å. The plan is to carry through subsequent investigations with perhaps two different potentials. For example, two different acceptable potentials can be distinguished from one another on the basis of the relative amounts of anion-anion and anion-cation energy represented in the energy per unit rhombohedral cell. At present, the lattice potentials being employed for surface reconstruction investigations to be discussed subsequently are for $D_{AC} = 0.77352$ eV, $\alpha_{AC} = 1.31819$ Å^{-1}, $R_{AC} = 2.32$ Å for the anion-cation interaction and $D_{AA} = 0.14484$ eV, $\alpha_{AA} = 1.99225$ Å^{-1}, $R_{AA} = 2.32$ Å for the anion-anion interaction.

Early work in heteroepitaxy, rather naturally but without other foundation, made extensive use of the concept of minimum mismatch as a determining factor in establishing relative film-substrate orientations. However, low-energy electron diffraction (LEED) studies of a number of film and/or substrate materials have already established that some sort of surface "reconstruction" sufficient to yield modified LEED patterns is the rule rather than the exception. Thus, the surface periodicity and/or symmetry can be altered from that of the bulk crystal.

9

An investigation of surface reconstruction in basal-plane Al_2O_3 has been initiated, using the potentials just discussed. Although basal-plane Al_2O_3 is not the substrate orientation of greatest practical importance, it is particularly convenient for beginning studies of reconstruction. The probable goal of these studies is to predict or calculate the relative energies of the various (1x1), $\sqrt{3}$, $3\sqrt{3}$, and $\sqrt{31} \pm 9$ deg LEED patterns described by Chang (Ref 7). However, it is not clear if all of these patterns can fit within the framework of the present model. Also, there is some evidence that impurities and/or surface stoichiometry may be determining factors producing the various LEED patterns. Thus, additional experimental information would be helpful in establishing which atomic surface configuration should be examined theoretically and in identifying the necessary theoretical ingredients.

Somewhat more basic but still related to surface stoichiometry is the question of the composition of the Al_2O_3 substrate at Si deposition temperatures. Early workers, in applying mismatch concepts at the interface, generally considered the deposited Si atoms to bond onto a bare plane of O atoms with the Si atoms occupying the missing Al atom sites. On the other hand, since each O plane in Al_2O_3 is separated by two Al planes with long and short bonds to the O planes, Chang (Ref 7) suggests that mathematical cleavage could most easily take place between two A planes, leaving one Al plane at the surface of each of the cleaved half-crystals. Intuitively, it appears that there would be considerable rearrangement of Al surface atoms if this is the case. Thus, one goal of the present work will be to examine both simple alternatives for the surface configuration and determine what conclusions can be reached.

Studies of surface reconstruction of basal-plane Al_2O_3 have been started by considering the relaxation of the four planes nearest to the surface. Table II lists the planes, atom type, and hexagonal coordinates of the 15 atoms which can be considered to represent the upper half of a 30-atom hexagonal unit cell. For this half cell the origin of coordinates is at an Al atom hole (i.e., the site of a missing atom). The upper boundary of the half cell then also contains an Al hole and defines a hexagonal network of holes.

In treating surface reconstruction it will be assumed for definiteness that the surface is an O plane, labeled plane 2 in Table II. Plane 1 is therefore excluded and planes 2, 3, 4, and 5 are included in the relaxation treatment.

Next, consider a mathematically-cleaved ideal (0001) Al_2O_3 crystal. Since this half-crystal still possesses three-fold symmetry normal to the surface and along the z (c-axis) direction and in addition still retains translational periodicity in directions lying in the surface, it is clear that there must be appreciable relaxation taking place which possesses this rotational and translational symmetry. There will also probably be relaxation which is not symmetric, but its origin is somewhat obscure and may relate to impurities or surface stoichiometry.

Consider relaxations of atoms in planes 2-5 which are consistent with symmetry. Two such relaxations are possible. The first type is associated with the parameter x in Table II, which defines the positions of O atoms in the unit cell and is equal to 0.306 for bulk Al_2O_3. With the absence of translational symmetry in the $\bar{a}_4$ or z direction, an allowable change would be for each O plane to relax toward a new value of x differing from the bulk value. Intuitively, it appears that the O plane at the surface would show the largest change. The magnitude of this type of relaxation has not yet been numerically determined. Preliminary indications are, however, that it is small.

10

TABLE II
Hexagonal Half-Cell Data for Al_2O_3

Plane No.	Atom Type	Hexagonal Coordinates a_1, a_2	$\bar{a}_4$ Initial Coordinate	$\bar{a}_4$ Relaxed Coordinate
-	Al hole	(0, 0)	0.5000	-
1	Al	(2/3, 1/3)	0.481333	-
2	O	(1/3-x, 2/3); (1/3, 2/3-x); (x+1/3, x+2/3)	0.41666	0.43853
3	Al	(0, 0)	0.3520	0.34913
4	Al	(1/3, 2/3)	0.31466	0.31629
5	O	(x, 0); (0, x); (1-x, 1-x)	0.250	0.24300
6	Al	(2/3, 1/3)	0.18533	-
7	Al	(0, 0)	0.1480	-
8	O	(2/3-x, 1/3); (2/3, 1/3-x); (2/3+x, 1/3+x)	0.0833	-
9	Al	(1/3, 2/3)	0.01866	-
-	Al hole	(0, 0)	0.0000	-

The second type of relaxation is that in which each of the various planes considered is allowed to move individually in the $\bar{a}_4$ or z direction. This type of relaxation appears significant for (0001) Al_2O_3, and numerical results have been obtained. The relaxed-plane positions were determined by an iterative procedure which relaxed planes 2, 3, 4 and 5 in turn toward the position of maximum energy until convergence was obtained. The results obtained are nearly as expected and are shown in the last column of Table II. Plane 2, the surface plane of O atoms in this case, shows the greatest (outward) displacement. Planes 3 and 4 are displaced only slightly and tend to move somewhat closer together. Plane 5 is seen to move inward and away from the surface a moderate amount. This negative displacement could have been expected on general grounds from the work of Tick and Witt (Ref 8), who found a similar negative displacement for Ni-like metal systems.

Other types of relaxation are to be investigated in the near future. The next case already being examined is identical to that reported above in that the constraint of symmetry is imposed. However, in this instance the surface plane will be an Al plane. These two atomic configurations determined with the constraint of symmetry will then be employed as the basis for more complicated types of surface reconstruction in which symmetry is not maintained. In this way, it is hoped that energetics of various types of substrate surface reconstruction can be determined. These reconstructions may play a major role in achievement of the goal of predicting the Si overgrowth orientation on Al_2O_3 substrates.

b. Application of Electron-on-Network Technique

In the theoretical studies at UCLA the possible application of the electron-on-network technique of Montroll et al (Ref 9) to heteroepitaxial systems has been under investigation (Ref 3). The procedure for adapting the technique to cases where lattice parameters near the surface are allowed to vary was developed and applied to calculations for the metal Na;* the plan was to then apply the procedure to the case of Al_2O_3.

Although the method is simple in principle, it became clear that significant difficulties would be encountered in applying it to heteroepitaxial systems. For example, in the Na case the evaluation of electron density using network wave functions was found extremely difficult in view of the transcendental distribution of parameters indexing the wave functions, although the computation was completed in spite of this. However, this cast considerable doubt on the feasibility of using the method for an accurate assessment of interfacial binding.

Further investigation of the method for use in heteroepitaxial systems has led to the conclusion that it is not adequate and should not be further pursued for this purpose. However, the use of the technique for computing variations in work function and surface double-layer potentials for single-crystal monovalent metals has led to a technical paper on the subject, and this is reproduced in Appendix I.

In summary, the model uses an electronic wave function which is defined to be nonzero only along the lines connecting first nearest neighbors in the metallic lattice. The electrons are summed to move freely along the lines between nearest neighbors. No electron-electron or electron-nucleus force is included in the model calculations (except for forces arising from the Pauli exclusion principle).

The work function is defined as the amount of energy required to move an electron from a point slightly inside the crystal to a point slightly outside. The contribution of the electronic double layer is included in the calculation of the work function as well as the dependence of the double-layer potential on the surface geometry. Surface states, where the electron is localized in the neighborhood of the face of the crystal, are found to have energies sufficiently above the Fermi level to eliminate the possibility that they make any contribution to the double-layer potential for the case of the (100) crystal plane. Consequently, surface states were ignored in all the calculations.

The surface double layer is assumed to be caused by the presence of a finite potential barrier at the surface of the crystal. Bulk electronic wave functions can penetrate this barrier and decay exponentially outside the crystal. The only parameters required by the model are the nearest-neighbor distance for the lattice and the height of the potential barrier at the surface. The former quantity is fixed by the lattice structure (body centered cubic for the alkali metals) and by the density, while the latter quantity can be adjusted to give the best agreement between the model calculations and experiment.

---

*The specific calculations for Na were carried out at UCLA on a separately-funded study not related to this contract.

For the alkali metals, Li through Na, the best value of the barrier height is about 50 percent of the sum of the ionization potential energy, the heat of vaporization, and the calculated Fermi level for the corresponding metal. In addition, the value of the double-layer potential found for Na agrees very well with a more sophisticated calculation in the literature and is reasonably close to the experimental measurement. Further details are given in Appendix I.

c. Calculations of Substrate-Induced Anisotropy in Electrical Properties of Si/Al_2O_3

It has long been recognized that differential thermal contraction between Si film and Al_2O_3 substrate will produce substantial stress in the Si film. Through the piezo-resistance effect, this stress acts to modify the electrical properties of the semi-conductor, including the carrier mobility.

An assumption which is usually implicit in most semiconductor thin-film material evaluations is that the electrical properties are isotropic and thus do not depend upon orientation in the plane of the film. However, within this reporting period, it was determined experimentally that most Si/Al_2O_3 films exhibit some degree of mobility anisotropy in the plane of the film. The experimental results are reported in detail under Subtask 6 in a subsequent section of the report.

In order to explain theoretically the anisotropy in carrier mobility, the changes in mobility and resistivity due to the stress originating in the differential thermal contraction of film and substrate have been calculated. For the sake of completeness, the difference in thermal expansion coefficients parallel and perpendicular to the c-axis in Al_2O_3 has also been taken into account. Theoretical formulae have been developed which are valid and applicable for both Si and Ge films and for Al_2O_3 and spinel sub-strates. The theory has been formulated generally, and (100), (110), (111) and (221) Si film orientations have been treated specifically as well as certain "off-orientation" cases.

Some of the numerical results are presented in the discussion of the work of Subtask 6. A comprehensive theoretical paper will be submitted for publication within the next few months, so the detailed description of the theory will not be reported here at this time. Some of the results obtained from the theory of (100)- and (221)-oriented Si films are, however, contained in Ref 10 and Ref 11, respectively.

While effects of stress on carrier mobility in heteroepitaxial films have been previously recognized (e.g., Ref 12), the investigations reported here are the first which have explicitly recognized and treated the orientational anisotropy in mobility which arises from differential thermal contraction and the relative orientation of film and substrate.

This study of mobility anisotropy is potentially very significant in that it promises a more detailed understanding of mobility in heteroepitaxial semiconductor films than it has been possible to obtain from previous investigations of the mobility.

13

2. SUBTASK 2. DEPOSITION STUDIES AND FILM PREPARATION

During the first year of the program the emphasis on this subtask was placed on determining the effect of experimental growth parameters on the quality of Si epitaxial films grown by the CVD method of pyrolysis of SiH_4 on substrates of various orientations of $A\ell_2O_3$ and $MgA\ell_2O_4$. It was established for the growth system used that autodoping occurs in Si on $A\ell_2O_3$ at temperatures greater than about 1050 C, so a concerted study was made which considered the effects of such factors as growth temperature, growth rate, and nucleation phenomena at or below this temperature (Ref 2).

Much of this work was rendered invalid by a very important effect which had not previously been reported in the technical literature dealing with the properties of heteroepitaxial semiconductor films. Specifically, it was found that the electrical properties of Si films on insulators with carrier concentrations $< 10^{16}$ cm^{-3} are dominated by surface-state conduction. Consequently, further studies were made on n-type films doped to $> 10^{16}$ cm^{-3}.

Simultaneous-growth studies on substrates which produced (100) Si and (111) Si below the autodoping temperature revealed the electrical properties of the films to be very dependent on substrate orientation. Although (111) Si growth on (10$\bar{1}$4) $A\ell_2O_3$ was found to be essentially equivalent electrically to (100) Si growth on (01$\bar{1}$2) $A\ell_2O_3$ below the autodoping temperature (~1050 C), changing the substrate orientation to near the (11$\bar{2}$0) $A\ell_2O_3$ plane (not previously used in epitaxy studies) increased the mobility of (111) Si films by about 20 percent for 2 μm-thick films and even more (~50 percent) for 5 μm-thick films, for the 10^{16}-10^{17} cm^{-3} carrier concentration range (Ref 2). It was suggested at the time that the better match of the thermal expansion coefficients for this $A\ell_2O_3$ orientation and for Si may have been responsible for the improvement.

Analysis of the data obtained during the third six-month period (Ref 3) further emphasized the strong interrelationships existing among the various parameters selected as most meaningful for optimizing Si growth on insulators. Evaluation of the electrical properties of Si films on $A\ell_2O_3$ orientations identified several years ago as providing reflective Si overgrowths demonstrated that growth conditions (1) must be optimized for each substrate orientation chosen; (2) differ for those $A\ell_2O_3$ orientations which lead to the same Si orientation; (3) are dependent upon reactor geometry and gaseous atmosphere; and (4) should be optimized for the particular film thickness desired.

The effects of annealing during film growth and the use of water-cooled reactors were investigated. Preliminary studies of Si growth by SiH_4 pyrolysis at reduced pressures (1 to 10 torr) were carried out and were very encouraging, indicating single-crystal growth can be obtained over a fairly wide temperature range, when conditions are optimized, on both $A\ell_2O_3$ and $MgA\ell_2O_4$ substrates. Brief investigation of the growth of Si films on both $A\ell_2O_3$ and $MgA\ell_2O_4$ using He as the growth atmosphere and as the carrier gas showed that epitaxial growth could be achieved, but the conditions for good quality growth were not established.

14

The work on this subtask during the fourth six-month period, described herein, was concentrated on continued attempts to optimize the Si deposition process for growth on ~(11$\bar{2}$0)-oriented and (01$\bar{1}$2)-oriented Al_2O_3 surfaces. These efforts involved (1) examination of the effects of post-nucleation annealing on ultimate film properties; (2) evaluation of the effects on film growth of gas-phase etching of the Al_2O_3 surface prior to deposition; (3) investigation of the effect on the growth process of using a water-cooled reactor chamber; and (4) preparation of a variety of Si/Al_2O_3 film composites for the study of the anisotropy of electrical properties in this system (see Subtask 6). In addition, an extensive study of the growth and properties of Si films on Czochralski-grown stoichiometric spinel ($MgAl_2O_4$) substrates was begun.

It should be noted that film properties and CVD growth conditions described in the preceding semiannual report (Ref 3) were indicative of the achievement of near-optimum conditions for Si growth on several Al_2O_3 orientations, using the vertical reactor system. There was considerable spread in the results obtained to that date, but much of that can now be explained based on the discovery and subsequent investigation of strong anisotropy effects in the Si/Al_2O_3 system. (See Subtasks 1 and 6.)

a. Effect on Film Properties of Annealing during Growth

To examine further the effects of annealing Si films at early stages of growth a group of Si/Al_2O_3 samples was prepared with the deposition process interrupted at various stages to permit a 20-minute annealing period followed by resumption of growth to the desired final thickness. Electrical measurements were then made on the Si films to evaluate the results of the annealing process. Preliminary studies, described in earlier monthly reports, had indicated this treatment was not detrimental to a 2000 Å-thick film, but its effect on the ~1000 Å-thick films grown in the more recent experiments was not known.

The data obtained are presented in Table III, in which it can be seen that a 0.67 μm-thick (111) Si film annealed at 800 C exhibited a carrier mobility of 490 cm2/V-sec, considerably better than the mobility of 190 cm2/V-sec measured for another film which was annealed at 1100 C. The data, although sparse, seem to indicate that 1100 C is better than 1050 C as the growth temperature for (111) Si on ~(11$\bar{2}$0) Al_2O_3.

Further studies of the effects of annealing at intermediate stages during the growth of Si films on Al_2O_3 involved the growth and anneal of ~2000 Å of Si at a growth rate of ~4 μm/min followed by further growth at the same rate. The results, shown in Table IV, confirm that the annealing of very thin Si films on Al_2O_3 followed by additional film growth does not impair the ultimate mobilities of films so grown. The best films in this series of depositions, annealed or unannealed, were grown on ~(11$\bar{2}$0)-oriented Al_2O_3 substrates; mobilities >400 cm2/V-sec were obtained in films only 0.6-0.7 μm thick.

However, the annealing studies to date have not demonstrated a significant improvement in the overall quality of Si films grown by this deposit-anneal-deposit technique realtive to those prepared by the conventional single-deposition method. On this basis, it was determined that no further studies of this technique would be pursued during the second-year program.

15

TABLE III.
Electrical Properties of Si Films Annealed for 20 min after Growth of ~1000 Å Thickness on Al_2O_3 Substrates (Growth Rate ~2μm/min)

Growth Temperature (C)	Film Orientation	Annealing Temperature (C)*	Measured Final Thickness† of Film (μm)*	Resistivity (ohm-cm)**	Carrier Conc. (cm^{-3})**	Mobility (cm^2/V-sec)**
1050	(100)	800	0.55	1.01	2.9×10^{16}	210
1050	(111)	800	0.61	$>10^4$	-	-
1050	(100)	1050	0.53	0.41	4.0×10^{16}	380
1050	(111)	1050	0.48	2.58	1.4×10^{16}	180
1100	(100)	800	0.64	0.87	3.3×10^{16}	220
1100	(111)	800	0.67	0.55	2.3×10^{16}	490
1100	(100)	1100	0.50	0.59	3.2×10^{16}	330
1100	(111)	1100	0.55	1.49	2.2×10^{16}	190

† Thickness measured at two locations on main segment of Hall bridge.

* Growth of final portion of film to thickness given carried out after annealing first ~1000 Å at specified temperature.

** Numbers represent single determination of electrical parameter by standard techniques.

Use of these substrates for Si growth clearly demonstrated that, just as for mechanically polished $A\ell_2O_3$, the appearance of the surface can be very misleading. Some surfaces that look scratch-free really contain scratches that are filled in by polishing powder and debris. This condition was revealed during attempts to clean $MgA\ell_2O_4$ surfaces for Si growth; it was found that after about 10 to 30 min in hot HF, most of the "fill-in" material is removed. Figure 3 shows adjacent regions of the surface of a broken slice of (111) $MgA\ell_2O_4$; the right side was "etched" for 30 min in hot HF. The defects shown are apparent in $MgA\ell_2O_4$ polished by either of the two principal vendors* as well as by NR laboratories.

Just as was the case for $A\ell_2O_3$ substrate surfaces, it was not evident from the quality of Si films grown on these polished but defective substrates that the surfaces were as poor as later scrutiny showed them to be. The explanation for the high quality of Si films that can be grown on relatively poor substrate surfaces, both for $A\ell_2O_3$ and for $MgA\ell_2O_4$. is yet to be found. It seems clear that chemical or combined chemical-mechanical polishing processes, probably used in conjunction with various annealing procedures, should be studied further as means for removing or minimizing surface work damage on $MgA\ell_2O_4$ substrates intended for epitaxy use.

It is important to note that, in the studies on this program to date, higher quality Si films have been grown on $MgA\ell_2O_4$ substrates than on $A\ell_2O_3$ substrates. Numerous variables remain, however, and this is not necessarily regarded as a final conclusion.

a   b

Figure 3.   (111) Czochralski $MgA\ell_2O_4$ (a) before Etching;
(b) after Etching in Hot HF for 30 min

*Union Carbide Corp. and Crystal Technology, Inc.

TABLE IV.

Electrical Properties of Si Films Annealed for 20 min after Growth of
~2000 Å Thickness on Al_2O_3 Substrates (Growth Rate ~4μm/min)

Growth Temperature (C)	Substrate Orientation	Annealing Temperature (C)	Measured Final Thickness of Film (μm)	Resistivity (ohm-cm)*	Carrier Conc. (cm^{-3})*	Mobility (cm^2/V-sec)*
1100	$(01\bar{1}2)$	750	0.56	0.71	3.3×10^{16}	270
1100	$(10\bar{1}4)$	750	0.56	0.76	4.2×10^{16}	200
1100	$\sim(11\bar{2}0)$	750	0.61	0.52	2.9×10^{16}	420
1100	$(01\bar{1}2)$	850	0.53	0.64	3.4×10^{16}	285
1100	$(10\bar{1}4)$	850	0.58	1.0	3.0×10^{16}	200
1100	$\sim(11\bar{2}0)$	850	0.59	0.76	2.3×10^{16}	360
1100	$(01\bar{1}2)$	940	0.59	0.57	3.9×10^{16}	280
1100	$(10\bar{1}4)$	940	0.61	0.98	3.1×10^{16}	207
1100	$\sim(11\bar{2}0)$	940	0.68	0.58	2.8×10^{16}	390
1100**	$(01\bar{1}2)$	–	0.60	0.43	4.7×10^{16}	311
1100**	$(10\bar{1}4)$	–	0.62	0.96	3.5×10^{16}	187
1100**	$\sim(11\bar{2}0)$	–	0.68	0.31	4.2×10^{16}	478

*Numbers represent single determination of electrical parameter by standard techniques.

**No intermediate annealing step used.

17

b. Effect of Gas-Phase Etching of Substrates on Film Properties

Gas-phase etching has revealed the presence of considerable surface and subsurface work damage on Al_2O_3 that is caused by the mechanical processing of the substrate in preparing a surface conducive to epitaxy. Yet it is striking that such damaged surfaces are being used in the industry for the epitaxial growth of Si and other semiconductors.

Experiments were carried out with the various substrate surfaces shown in Figures 6 and 7 of the Third Semiannual Report (Ref 3): Si films were grown and their electrical properties were measured. The data are shown in Table V and are somewhat surprising. Essentially identical carrier mobilities were found for films grown on unetched substrates and for those etched for as long as 100 min ($\sim 20~\mu m$ of thickness removed), for both Czochralski-and Verneuil-grown Al_2O_3. This was taken to indicate that (1) the work damage is even greater than 20 μm deep in these substrates (which were prepared by commercial vendors), or (2) that the Si overgrowth is able to "overcome" much of the substrate surface imperfection during its growth, with the actual mobility-limiting factor being the stress-producing thermal contraction and/or lattice mismatch between the two materials, or (3) that there is a third species present on the substrate surface in this CVD reaction and that it provides the real growth-influencing sites.

Further experiments are needed to examine this important question in more detail.

c. Effect of Use of Water-Jacketed Reactors

Si growth experiments were performed in a water-jacketed reactor chamber, to compare the electrical properties of films grown in a water-cooled reactor with those of films grown without the reactor walls water-cooled. The results are given in Table VI for films grown both with and without water cooling. These results show that there is no apparent advantage in the use of a water-jacketed reactor in the vertical reactor system used in these experiments; in fact, the additional handling necessary to detach and attach the reactor from and to the system was found to be a distinct disadvantage.

At low growth rates the amount of reactor wall deposit appeared to be less in the case of the cold-wall reactor than for the uncooled reactor. However, because of the additional handling required and in view of the fact that the electrical properties were essentially the same for the two cases, no further studies are presently contemplated with the cold-wall reactor.

d. CVD Growth of Si on Spinel

Studies of the growth of Si on spinel were continued during this six-month period, with "6-9's" grade He as the major carrier gas. Films have been grown primarily on polished wafers of Czochralski spinel*

---

*Spinel boules and polished wafers obtained from Union Carbide Corporation and from Crystal Technology, Inc.

18

TABLE V.

Effect of Gas-Phase Etching of (01$\bar{1}$2) Aℓ_2O$_3$ on Si Film Properties*

Film Growth Temperature (C)	Etching Time (min)	Final Film Thickness (μm)	Resistivity (ohm-cm)	Carrier Concentration (cm^{-3})	Mobility (cm^2/V-sec)
1075**	0	2.13	0.45	2.7×10^{16}	510
	25	2.28	0.32	3.6×10^{16}	540
	50	2.13	0.46	2.8×10^{16}	490
	100	2.05	0.57	2.1×10^{16}	530
1075***	0	2.25	0.31	4.4×10^{16}	460
	25	2.28	0.28	4.7×10^{16}	470
	50	2.20	0.31	4.2×10^{16}	480
	75	2.23	0.31	4.4×10^{16}	460
	100	2.23	0.28	4.7×10^{16}	490

*Nominal growth rates ~5 μm/min

**High quality Verneuil-grown Aℓ_2O$_3$ substrates

***Czochralski-grown Aℓ_2O$_3$ substrates

TABLE VI.
Properties of Si Films Grown in Jacketed Reactor

Film Orientation	Film Thickness (μm)	Resistivity (ohm-cm)	Carrier Concentration (cm^{-3})	Mobility (cm^2/V-sec)
Without Water Cooling				
(100)	1.7	0.71	1.9×10^{16}	460
(111)	1.8	0.78	1.3×10^{16}	630
With Water Cooling				
(100)	2.0	0.26	5.0×10^{16}	490
(111)	1.9	0.35	2.9×10^{16}	620

In these studies, Pd-purified H_2 was added to the He carrier gas in order to reduce the wall deposits and improve the reaction efficiency. At growth temperatures of 1025 C, for example, Si growth rates in He (even with the H_2 addition) were reduced considerably with respect to those obtained with only H_2 as the carrier gas. For example, a SiH_4 flowmeter setting of 5 (25 ccpm pure SiH_4) resulted in a Si growth rate of ~2 μm/min in H_2 but only 0.4 μm/min in He containing small amounts of added H_2.

The effect of H_2 additions to He at high SiH_4 concentrations is shown in Figure 1. The SiH_4 flow was kept constant at 150 ccpm and the Si growth temperature was 1025 C. The data show that essentially a linear increase in growth rate results when H_2 is added to the He carrier gas, at least up to the indicated flow rate of 2000 ccpm (33 percent of the total carrier gas). Since the growth rate in pure H_2 has been found to be ~15 μm/min, the dependence on H_2 percentage is not linear throughout the range, leveling off at higher concentrations of H_2.

It was also established that for a given He-H_2 ratio the growth rate is very temperature-dependent. This is shown in Figure 2 for a constant SiH_4 flow (nominally 150 ccpm) and 0.8 percent H_2 in He. Over the 100-degree temperature span investigated the growth rate is seen to change by a factor of 4, being lower at the higher temperature.

It is difficult to understand how higher temperatures cause such a large decrease in the growth rate. The behavior is very different from that observed in a pure H_2 carrier gas atmosphere; distinct mechanisms appear to be operative in the two cases. The phenomenon may be similar to that observed in preliminary experiments with growth of GaAs on GaAs substrates by the pyrolysis of trimethylgallium and arsine (AsH_3); in that case the growth rate is greater on the (111) "A" face than on the ($\bar{1}\bar{1}\bar{1}$) "B" face of GaAs, a difference presumably caused by a difference in the charge on the surfaces of the {111} faces.

Since it was earlier found that the net carrier concentration in As-doped Si films is growth-rate dependent when H_2 is the carrier gas (Figure 19, Ref. 3), it was expected that similar effects would be observed in the He-H_2 system. The results obtained in an examination of this question are shown in Table VII. The data indicate
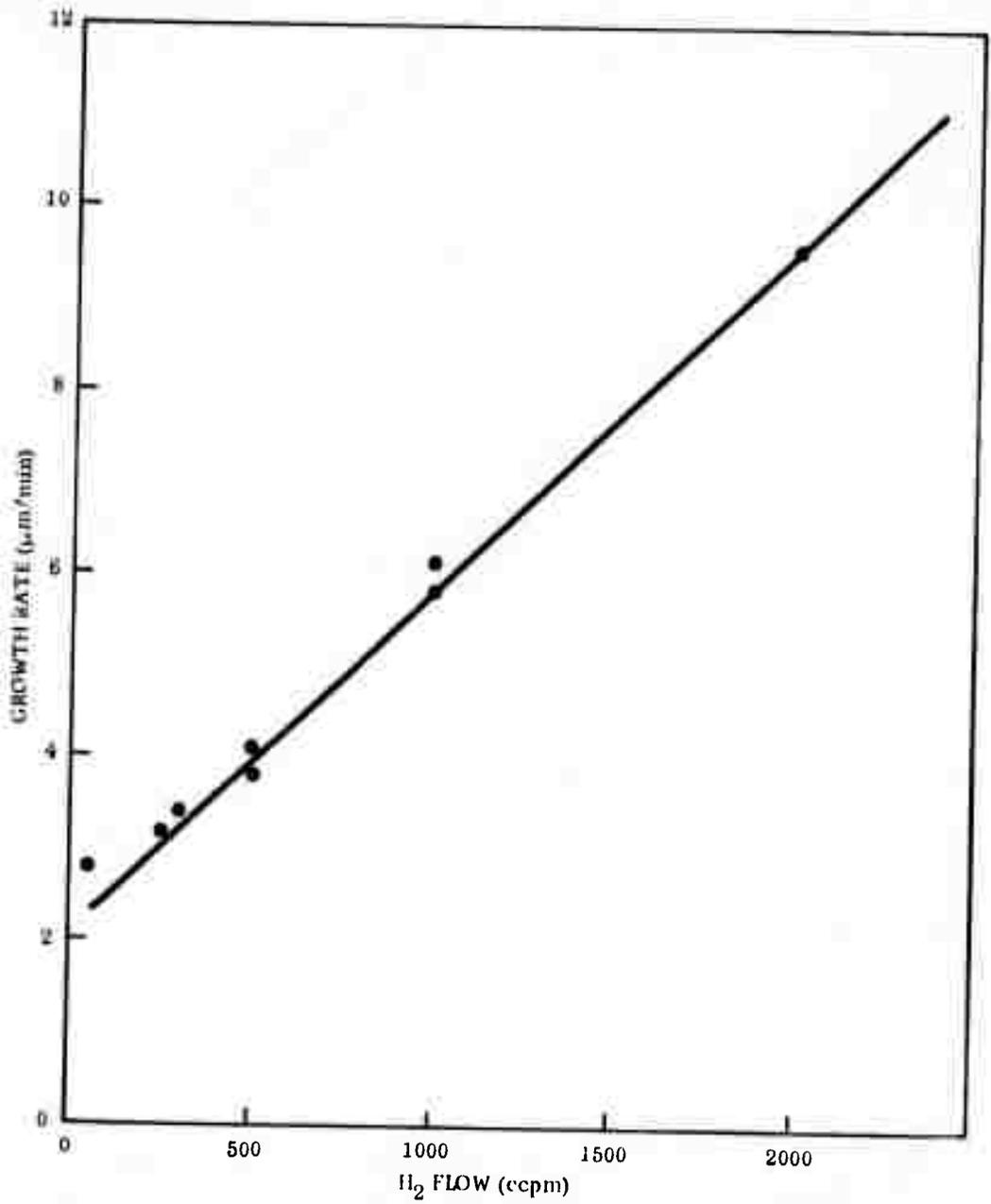
Figure 1. Changes in Si Growth Rate at 1025 C Caused by H_2 Additions to He Carrier Gas (SiH_4 Flow Rate 150 ccpm)

21
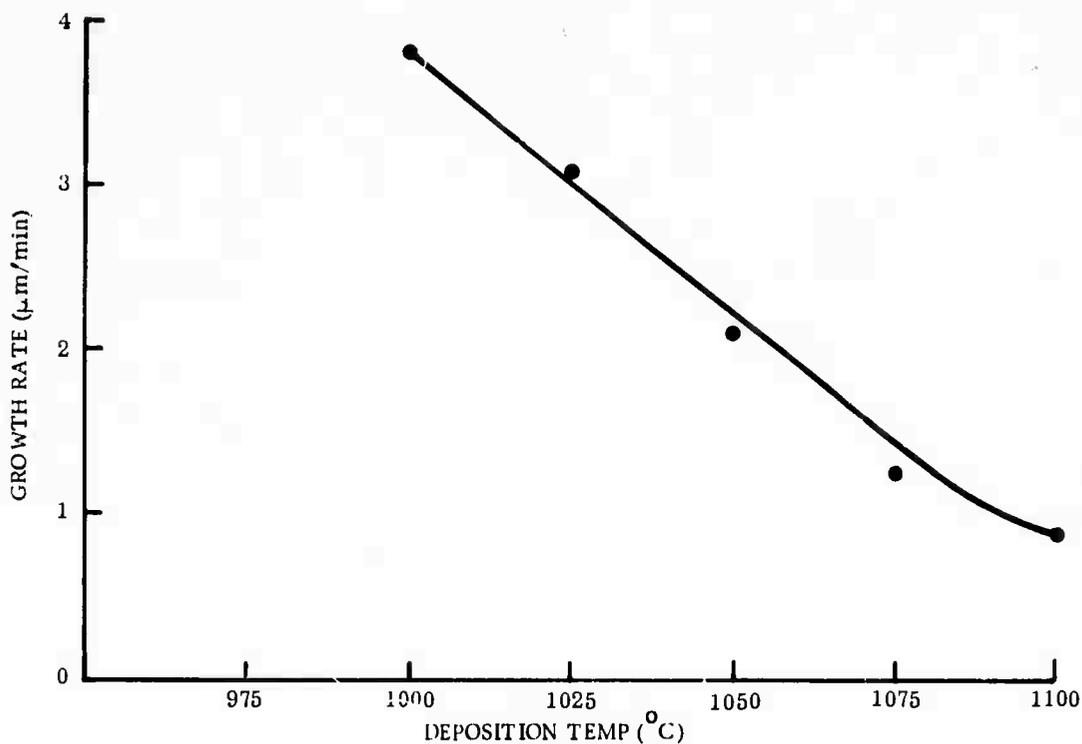
Figure 2.   Effect of Growth Temperature on Si Growth Rate for SiH_4 Flow Rate of 150 ccpm and $H_2/He = 0.8$ Percent

TABLE VII.
Effect of Growth Rate on Doping Level for Si Films Grown on (111) Spinel at 1025 C in He-H_2 Atmospheres (Constant Dopant Gas Flow Rate)

H_2 in He (%)	Film Thickness (μm)	Growth Rate (μm/min)	Resistivity (ohm-cm)	Carrier Concentration (cm^{-3})	Mobility (cm^2/V-sec)
0.8	1.90	2.8	0.33	2.6×10^{16}	747
4.2	1.87	3.2	0.41	1.9×10^{16}	792
8.4	2.05	4.1	0.46	1.5×10^{16}	900
16.8	1.85	5.8	0.56	1.6×10^{16}	718
33.3	2.10	9.7	0.23	3.0×10^{16}	925

22

that the doping level does not change appreciably with growth rate in He-H$_2$ atmospheres at 1025 C. The dependence of doping level on growth temperature has not yet been determined.

The question of the extent of autodoping in the Si/spinel system has been examined in preliminary experiments. Undoped Si films were grown on spinel at various deposition temperatures (1000 to 1100 C) using a constant amount of SiH$_4$ and H$_2$-He mixture.

As shown in Table VIII, films grown in the 1000 to 1050 C range were n-type; at 1075 C and 1100 C they were p-type before annealing. Annealing in O$_2$ and N$_2$ caused the films to become more strongly n-type, suggesting the removal of acceptor impurities and/or defects by the annealing process. It thus appears that the autodoping phenomenon is operative for Si/spinel in the He-H$_2$ atmosphere at approximately the same temperatures as for the Si/Aℓ_2O$_3$ system (Ref 3).

TABLE VIII.
Autodoping in Si/(111) Spinel Using 0.8 Percent H$_2$-in-He as Carrier Gas

Deposition Temp (C)	Film Thickness (μm)	Growth Rate (μm/min)	Film Resistivity* and Type**	
			Before Anneal (ohm-cm)	After Anneal (ohm-cm)
1000	2.1	3.8	4.2×10^2 (n)	1.3 (n)
1025	2.0	3.1	25.4 (n)	0.4 (n)
1050	1.8	2.1	3.2 (n)	0.28 (n)
1075	1.8	1.2	4.8×10^2 (p)	76. (n)
1100	4.4	0.9	1×10^3 (p)	1. (n) (Reflective edge reg'on) 6.6×10^2 (p) (Gray central region)

 * Four-point-probe measurement
 ** Thermoelectric probe determination

Because of the importance of the phenomenon it is planned that further investigation of autodoping in the Si/spinel system, as a function of both H$_2$-He ratio and temperature, will be carried out during the next six months.

3. SUBTASK 3. ANALYSIS AND PURIFICATION OF CVD REACTANTS

During the first year, techniques of gas chromatography were developed for analysis of the reactants used for semiconductor heteroepitaxy by CVD. A general-purpose gas-handling system was constructed for the highly volatile and reactive gases studied, with silicone oil and polymer columns used for the chromatography. Several extraneous impurity peaks were observed in the chromatograms of SiH_4 samples; diborane (B_2H_6) was tentatively identified as a significant impurity (~ 10 ppm), although not confirmed by mass spectrometer techniques. Small quantities of purified SiH_4, free of diborane, were prepared by successive injections in the chromatograph; quantities were too small, however, for use in laboratory CVD experiments. A summary of this work, which was carried out at UCLA, was given in Appendix A of the Third Semiannual Report (Ref 3).

In the first six months of the second year the emphasis of the work of this subtask was changed. Analyses of the reactants used in the CVD experiments were continued, primarily by sensitive mass spectrometric techniques with the assistance of external analytical service laboratories. Samples of SiH_4 and of trimethylgallium (TMG) used for Si and GaAs CVD experiments were analyzed for impurity content. Disilane and trimethylsilane, together with several other impurities of less concern, were found in various SiH_4 samples. The analyses of TMG samples were subject to various uncertainties, some of which still remain unresolved.

During the past six months additional reactant analyses have been carried out, and a significant new study of the chemistry and reaction kinetics of the CVD processes used for depositing Si and GaAs films in heteroepitaxial systems has been initiated in the Department of Chemistry at California State University, San Diego. These two aspects of the subtask will be described in sequence.

a. Analysis of CVD Reactants for Impurity Content

Four different tanks of "pure" SiH_4 have been used in the studies of Si deposition on spinel ($MgAl_2O_4$) during the past six months. Three of these were analyzed for impurity content before use in these experiments by an analytical service laboratory[*] using sensitive mass spectrometric techniques. One of the four tanks was also reanalyzed after the pressure had dropped in use to 35 psi from an original value of 85 psi.

These data are given in Table IX, together with an independent analysis performed by another laboratory[**] and supplied with one of the SiH_4 tanks by the vendor. First, the discrepancies in the data of the two analyses obtained for the tank of SiH_4 supplied by Vendor B are significant. The analytical procedures used in the supplied analysis apparently are not able to detect, for example, less than 3000 ppm of O_2, an impurity of importance in SiH_4 which could lead to the formation of SiO_2 (and resulting pinholes) in deposited Si films. The other differences in the analytical data for this tank indicate insufficient sensitivity in the mass spectrometer methods used in the analysis to properly establish the concentrations of those impurities which could be detrimental to high-purity Si growth.

---

[*]West Coast Technical Service, Inc. (WCTS), San Gabriel, CA.
[**]Gollob Analytical Service, Berkeley Heights, NJ

TABLE IX.

Mass Spectrometric Analyses† of SiH_4 from Three Vendors

Constituent	SiH_4 Cyl. RR32277 (Vendor A)⊕ (ppm)**	SiH_4 Cyl. 15-1796 (Vendor B)⊕ (ppm)**	(ppm)**	SiH_4 Cyl. C1018 (Vendor C)⊕ (85 psi) (ppm)**	(35 psi) (ppm)**
Hydrogen	115	470	ND 1×10^3	38	18
Water	1	2	NR	4	<1*
Argon	26	97	ND 10	68	46
Hydrocarbons as butane	1	1	NR	<1*	<1*
Disilane	195	28	70	10	8
Boron Compounds	<1*	<1*	NR	<1*	<1*
Carbon dioxide	<1*	39	ND 10	<1*	2
Monochlorosilane	<1*	<1*	NR	<1*	<1*
Oxygen	<5*	<5*	ND 3×10^3	<5*	<1*
Helium	<2*	<5*	ND 20	<5*	<1*
Siloxane	<5*	<5*	ND 10	<5*	<1*
Silane	Balance	Balance	Balance	Balance	Balance

* Limits of detection.

**ND: None detected, so less than.

NR = Not reported.

†Analyses performed by West Coast Technical Service, Inc., unless otherwise noted.

††Analysis supplied with tank, done by Gollob Analytical Service

⊕A: Will Ross, Inc., Matheson Gas Products Div.

 B: Scientific Gas Products, Inc.

 C: Synthatron Corp.

25

Note also the relatively high concentrations of H_2 and disilane in the tanks obtained from Vendors A and B compared with those in the SiH_4 prepared by Vendor C. The effects of these impurities on Si growth seem to be minimal in a growth system using H_2 as the carrier gas. However, if He is the carrier it is difficult to predict how these impurities might affect the nucleation mechanism. Another source of concern is the CO_2 content in the tank from Vendor B. This impurity also could lead to SiO_2 formation in a H_2 atmosphere by a "water-gas" reaction,

$$CO_2 + H_2 \underset{\Delta}{\rightleftharpoons} CO + H_2O, \tag{1}$$

the water then reacting with SiH_4 to form SiO_2. The impurity levels indicated in the table preclude further use of SiH_4 from this vendor until significant improvement in purity is achieved.

The remeasurement of the impurity levels in the SiH_4 from Vendor C was prompted by a sudden inability to control Si film growth rates within reasonable limits (~10 percent) with either He or H_2 carrier gases. The second analysis, however, did not provide an indication of the cause of this difficulty. A change in SiH_4 tanks apparently solved the problem of growth-rate control, although the electrical properties of the films grown on $MgAl_2O_4$ with the first tank of SiH_4 were quite good; mobilities were between 700 and 925 cm^2/V-sec for films with carrier concentrations of 10^{16}-$10^{17}/cm^3$.

The change to the other tank of SiH_4 (supplied by a fourth vendor* for evaluation) was coincident with the growth of films with reduced mobilities - lower than 700 cm^2/V-sec. With the change of SiH_4 tanks growth and dopant control had to be re-established; Si films were grown on (111) $MgAl_2O_4$ with mobilities similar to those obtained on (01$\bar{1}$2) Al_2O_3 (~400-500 cm^2/V-sec) but inferior to those obtained previously on (111) $MgAl_2O_4$ (700-925 cm^2/V-sec). To explore the situation further the condensable component of the reactant was trapped in the SiH_4 line at -78 C and transferred to a specially prepared sampling cylinder for mass spectrometer analysis. The presence of H_2O and tetrahydrofuran (THF) in this sample was established and was consistent with the fact (determined subsequently) that the manufacturer used THF as a solvent in the preparation of the SiH_4. The low mobilities, however, were not consistent with the fact that a 100 μm-thick film of Si grown on p-type Si had reasonable electrical properties ($\rho = 24.8$ ohm-cm, $n = 1.98 \times 10^{14}/cm^3$, and $\mu = 1270$ cm^2/V-sec). It appears that something in the SiH_4 is affecting the growth quality on insulating substrates. The results also suggest that SiH_4 and H_2O can coexist in a closed container but that their reaction is catalyzed by exposure to air.

This impurity problem has prevented an accurate evaluation of the effects of deposition parameters on Si film properties. It will probably be necessary to perform such studies with sufficient quantities of starting materials to complete the entire investigation, with the hope that the gas purity is not affected by changes in total tank pressure. In view of this, a 200-gm quantity of SiH_4 has been obtained from Synthatron Corporation for further studies of Si growth on $MgAl_2O_4$. It has not yet been evaluated for impurity content, however.

---

*Liquid Carbonic Corporation

A tank of AsH_3-in-He (nominally 10 percent AsH_3) was obtained from Airco for GaAs growth studies. In evaluating it by means of GaAs growth on Al_2O_3, using a good source of trimethylgallium, it was found that considerable condensate was obtained at -45 C. The tank was returned to the vendor, and it was analyzed by West Coast Technical Service, Inc. The gas was found to contain the following:

AsH_3	12.2 mole percent	CO_2	4 ppm
Water	15 ppm	H_2S	4 ppm
N_2	56 ppm	He	balance
Oxygen	15 ppm		
Argon	17 ppm		

The high concentration of water, O_2, CO_2, and H_2S could be expected to affect the quality of the GaAs films. A replacement tank is now being prepared by the vendor.

Another tank of 10 percent AsH_3-in-H_2, obtained as a research sample from Phoenix Research Corporation for similar evaluation by GaAs deposition, was described in the vendor's analytical report as containing no impurity greater than 1 ppm. No condensate was obtained at -45 C, and thick undoped GaAs films were found to be p-type; this indicates a low donor impurity content in the reactant. Several GaAs films were grown at various AsH_3-TMG ratios, with H_2Se added as dopant. However, the electrical data obtained for films grown on Al_2O_3 using this AsH_3-in-H_2 were inconclusive; it was found that the dopant levels in the Se-doped films were not in the 10^{15}-10^{16} cm^{-3} range, desirable for permitting mobilities which are more meaningful for evaluation of the GaAs film quality. Additional GaAs films on Al_2O_3 have been grown for evaluation of this particular tank of AsH_3-in-H_2, but the results are not yet complete.

b. Study of Chemistry and Reaction Kinetics of CVD Processes

During the past six months arrangements have been made for fundamental studies of the chemistry and reaction kinetics of the CVD processes used for growing Si and GaAs films in heteroepitaxial systems to be carried out by scientists in the Department of Chemistry at California State University, San Diego (CSUSD). This group* is experienced in studies of chemical reactions of the Si hydrides and related systems and is in a position, in terms of present work and past experience, to make important contributions to the fundamental studies of this contract program and to thereby permit further improvements in the manner of application of these chemical reactions to the practical growth of semiconductor thin films for device use. For example, the long-standing question as to whether the release of Si by the pyrolysis of SiH_4 occurs in the gas phase near a substrate surface or on the substrate surface itself can probably be answered by the experiments to be undertaken at CSUSD. This point is of major importance to the planned in situ CVD experiments in the electron microscope (Subtask 5).

---

*The studies will be carried out by Prof. M. A. Ring and associates.

In these studies, an investigation will be initiated into the basic chemistry involved in the formation of GaAs from the metalorganic-hydride reaction of tri-methylgallium ($Ga(CH_3)_3$) and AsH_3 and in the deposition of Si by the pyrolysis of SiH_4.

The flow pyrolysis of trimethylgallium (TMG) with AsH_3 will be examined over an inert surface (Si mirror) to determine the requirements for the formation of pure GaAs. The parameters to be varied will be the pyrolysis temperature, the TMG-AsH_3 ratio, and the partial pressure of H_2. In addition, the volatile products will be determined. The decomposition modes of AsH_3 and TMG will be examined to determine what radicals are produced in the pyrolyses of AsH_3 and of TMG and in the co-pyrolysis. The reaction of these radicals with TMG and AsH_3 will be investigated.

The pyrolysis of SiH_4 and Si_2H_6 over Al_2O_3 will be investigated. The Al_2O_3 will be preheated to various temperatures (400 to 1100 C) prior to each pyrolysis to determine effects due to heat treatment. The pyrolysis of Si_2H_6 over Al_2O_3 will be carried out in the presence of CH_3SiD_3 to determine whether the Al_2O_3 has changed the mechanism of decomposition from the 1,2-hydrogen shift observed in the homogenous decomposition.

$$Si_2H_6 \longrightarrow SiH_2 + SiH_4 . \tag{2}$$

The possibility of SiH_4 decomposition initiated by H atoms from molecular hydrogen decomposition above 600 C will also be examined.

All of these reactions will be carried out in flow systems with low-temperature traps which will remove the heavier less stable products from the stream. This will allow for the determination of the effect of pyrolysis temperature on the yield of Si_2H_6 in the pyrolysis of SiH_4:

$$2 \, SiH_4 \longrightarrow Si_2H_6 + H_2. \tag{3}$$

This last point will provide some information concerning the species which are present at the point of Si deposition.

The first experiments to be undertaken are directed toward determining the role of the Al_2O_3 surface in catalyzing the decomposition of SiH_4 and other Si hydrides. Apparatus has been fabricated and assembled, and experimental work is in progress.

4. SUBTASK 4. PREPARATION AND CHARACTERIZATION OF SUBSTRATES

In the first year of the program it was demonstrated that Al_2O_3 surfaces prepared by mechanical polishing techniques and used routinely for semiconductor heteroepitaxy typically have severe surface and subsurface damage, with many scratches often several microns deep and rendered invisible to close inspection by amorphous or fine-grained debris embedded in the scratches in the final polishing stages. Some improvement in mechanical polishing procedures was achieved in terms of the density and depth of such damage. Gas-phase etching/polishing procedures using SF_6 and various fluorinated halocarbons in the 1350 to 1500 C temperature range

28

produced essentially scratch-free surfaces on $(01\bar{1}2)$ and near-$(11\bar{2}0)$ Al_2O_3 substrates. Extensive gas-phase etch-rate data were obtained as a function of crystallographic orientation in this temperature range.

During the first half of the second year a much improved technique for polishing $(10\bar{1}4)$ Al_2O_3 was developed, and excellent surfaces in this orientation can now be obtained. Gas-phase etching/polishing techniques were further developed and exploited for (1) thinning Al_2O_3 substrates to thicknesses the order of 1 mil; (2) evaluating the effects of prolonged etching on $(01\bar{1}2)$, (0001), and $\sim(11\bar{2}0)$ Al_2O_3; and (3) assessing the subsurface damage caused by various mechanical polishing procedures. Routine characterization of substrate surfaces at various stages of preparation continued using techniques of X-ray and electron diffraction analysis and optical and electron microscopy.

In the past six months the improved polishing procedure (Ref 3) for $(10\bar{1}4)$-oriented Al_2O_3 has been verified as a reproducible process; polishing methods for preparing $MgAl_2O_4$ surfaces have been applied to wafers used for Si heteroepitaxy experiments; considerable effort has been devoted to the development of ion-beam sputtering techniques for thinning Al_2O_3 wafers for use in the in situ CVD studies (Subtask 5); gas-phase etching experiments with $MgAl_2O_4$ surfaces were initiated; experiments with Rutherford backscattering of charged-particle beams as a means of characterizing substrate surface conditions were resumed; and preliminary experiments with Auger electron spectroscopy were undertaken to evaluate the technique as a means for characterizing substrate surface impurities. A number of the investigations planned for this subtask in this report period were started late because of increased emphasis on other subtasks of the program; only the first three of the above activities will be discussed further below.

a. Mechanical Polishing of $(10\bar{1}4)$-Oriented Al_2O_3

Si deposition experiments using $(10\bar{1}4)$ Al_2O_3 substrates prepared by the improved polishing procedure (Ref 3) for this orientation indicated that better films can now be obtained on these improved surfaces than had been realized previously. This is consistent with the observation that gas-phase etching in freon at 1400 C revealed a reduced amount of surface and subsurface damage on these substrates relative to others prepared by the earlier polishing methods. The improved procedure was shown to be a reproducible process; several groups of wafers in this orientation were prepared in the same way, and Si film deposition experiments indicated that the surfaces were consistently the best yet achieved on this orientation.

b. Polishing Methods for $MgAl_2O_4$

Polishing methods being developed on a separately-funded program* for a variety of crystallographic orientations of stoichiometric spinel ($MgAl_2O_4$) were applied to some of the substrates used for Si heteroepitaxy experiments in this contract program.

---

* Subcontract for Crystal Technology, Inc., Mountain View, CA, as part of AFML Contract No. F33615-70-C-1544.

c. Ion-Beam Sputtering Techniques for Thinning Al_2O_3 Substrates

Ion-beam sputtering, also called ion-beam machining, ion thinning, ion sputtering, or ion etching, is a technique whereby material is removed from the surface of a sample by controlled sputtering caused by an incident ion beam. The process may be used for (1) etching, to clean substrates prior to epitaxial deposition; (2) polishing, in which a scratched or work-damaged surface layer typically 1 to $10\mu m$ deep is removed; or (3) thinning, in which bulk samples prepared to the thickness limits of conventional mechanical polishing are thinned to ~200 Å as required for transmission electron microscopy. Although both (1) and (2) have been investigated, the emphasis to date has been placed on producing thin Al_2O_3 "wafers" or membranes for use as substrates for the in situ chemical vapor deposition studies of this contract (Subtask 5).

The ion beam sputtering is performed in an Edwards ion-beam machining apparatus (IBMA), shown in the photograph of Figure 4. It consists of a conventional high-vacuum system containing two opposed ion guns and appropriate feedthroughs. The sample, normally 0.125 inch in diameter, is held as shown in the schematic diagram of Figure 5, so that each side is struck by an ion beam at a glancing angle of 5 to 30 deg. Argon ions are used, with energies typically 5-10 kV. The sample is rotated in its plane at 15 rpm. Appropriate shutters are used to measure the ion-beam current.
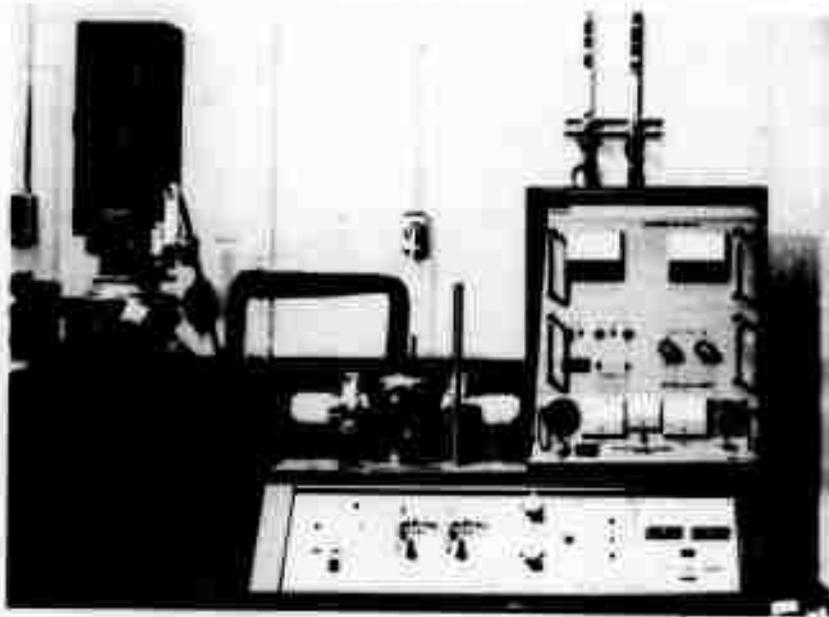
Figure 4. Ion Beam Machining Apparatus (IBMA)

31
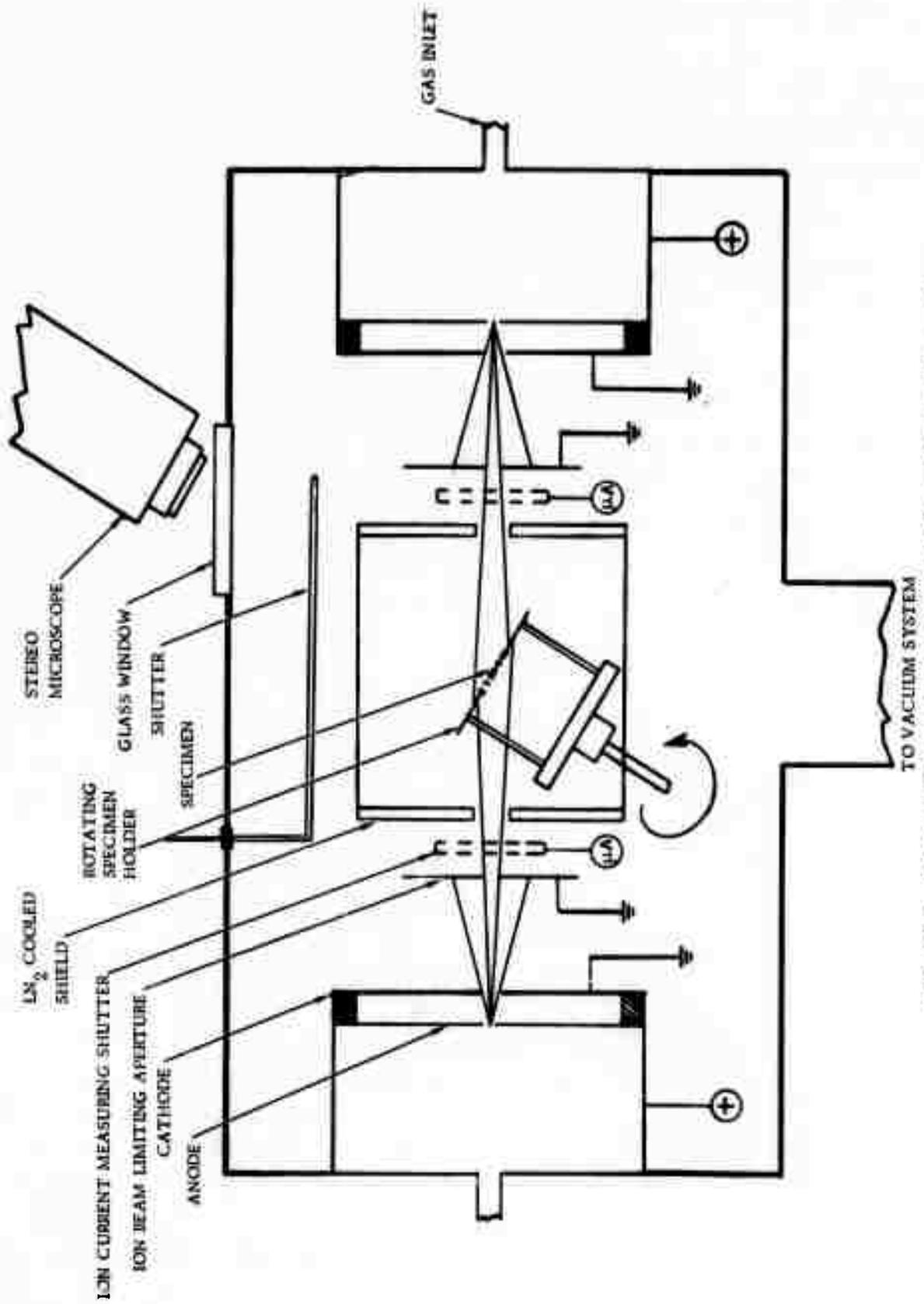
Figure 5. Configuration of IBMA-Working Chamber (not to scale)

32

The IBMA has been extensively modified to overcome certain operational difficulties and to improve the operating convenience. A new sample holder was built to hold specimens up to 0.75 in. in diameter and to permit tilting the sample for a beam angle down to 5 deg instead of the standard 10 deg.

A new gas metering system was built by replacing the original-equipment leak valves with more precise vernier metering valves for control of the low gas flow ranges required. Vacuum-tight on-off toggle valves were also installed so the gas flow could be shut off without disturbing the vernier valve setting.

A new viewing flange has been built and installed on the top of the working chamber (Figure 5). This and other modifications permit more accurate and convenient operation in the following ways:

1. A larger recessed window permits viewing the sample with a stereo microscope during ion bombardment even at large sample tilt angles. Considerable time is saved as the flange no longer must be removed periodically for sample examination during an extended thinning operation.

2. A shield protects the ion-current measuring shutters from all but the central portion of the beam. Only the current actually used for ion-beam thinning is measured, not the total current.

3. A movable shutter prevents the window from being coated with material sputtered from the sample and its holder.

4. A larger liquid-nitrogen shield was installed, increasing the shielding efficiency.

The first step in preparing Al_2O_3 for transmission electron microscopy is mechanical lapping and polishing of the wafer to as small a thickness as possible, typically 0.002 to 0.003 inch. Below this thickness the samples fracture during polishing or removal from the polishing jig because of the large residual stress present. The thinned slices are then cut into 0.125 inch or smaller circular discs, a process in which some additional samples may fracture. Because the IBMA thinning rate is so low, considerable effort has been expended to develop a procedure for mechanically polishing Al_2O_3 to less than 0.002 inch, but the yield has been quite low. Al_2O_3 wafers commercially polished* behave similarly, fracturing during polishing or when being cut into disks.

The small thinned disks are installed in the IBMA sample holder sandwiched between two 75-mesh grids. The 0.0007-inch thick grid protects the Al_2O_3 below the grid bars from being sputtered until the grid itself is sputtered away. The Al_2O_3 sample after thinning has a "waffled" surface, with the ridges providing mechanical strength so that very thin regions will not break during handling. The grid serves a second purpose by providing a number of individual thinned areas rather than one larger thinned region, thus increasing the yield by a factor of 4 to 100. Thinning usually is continued until a perforation is noted in one area; then the sample is examined in the transmission electron microscope. Ideally, thinning proceeds until

---

*Insaco, Inc., Quakertown, PA.

a suitable electron-transparent region first appears. It is impossible to judge with an optical stereo microscope the precise moment to stop the thinning process, so in practice it is continued until a small hole is visible in one grid square. At this point some grid squares will have only thicker regions, while other grid squares will have sizable holes.

The appearance of a sample thinned beyond the customary stopping point is shown in Figure 6a, photographed with monochromatic light to reveal thickness contours by means of interference fringes. Since this sample was only 5.5 μm thick initially, perforation occurred before the shielding grid was completely sputtered away.

Three different orientations of Al_2O_3 have been successfully thinned by ion-beam sputtering for transmission electron microscopy — (0001), (10$\bar{1}$4), and (01$\bar{1}$2). With the exception of samples 1, 2 and 8, for which complete thinning was not attempted, each sample listed in Table X provided thin (~200 Å) areas which could be examined directly and which were at least marginally suitable for use as substrates for the in situ CVD experiments. The electron diffraction spot patterns and Kikuchi patterns obtained from samples in these three orientations are shown in Figures 7 through 11. It is believed that these are the first such patterns obtained from single-crystal Al_2O_3. The spot patterns are from thin regions ($\lesssim$500 Å thick); the Kikuchi patterns are from thicker regions ($\lesssim$10,000 Å).

Electron micrographs representative of the samples of Table X are shown in Figures 12 through 20. The samples are of relatively high quality single-crystal Al_2O_3, so no internal defect structure is visible. The ideal, uniformly-thinned crystal would appear featureless on an electron micrograph. However, three characteristics are clearly visible in these figures — extinction contours, surface structures, and a thickness gradient. The combination of these factors is least noticeable in Figures 17, 18, and 19, which accordingly would be the most desirable substrates for in situ CVD. The other samples would be marginally suitable as substrates. The importance of each of the above three factors will be discussed, and then other features of specific interest in certain of the micrographs will be described.

The extinction contours, observable in all of the micrographs but especially pronounced in Figures 12, 13, 14, and 20, are the result of constructive and destructive interference of the electron waves passing through the crystal. Extinction contours in electron microscopy are analogous to interference fringes in optical microscopy, but unlike the latter their spacing is not simply related to the thickness of the crystal. Slight tilts of the crystal will dramatically change the contour spacing. Extinction contours are quite sensitive to crystal orientation and thus will reflect minor amounts of strain or buckling in the crystal. When those characteristics are absent, as in Figure 13, the extinction contours give a qualitative indication of local thickness variations. The combination of a thickness gradient and local strains and buckling can result in rather interesting combinations, as shown in Figures 12 and 14.

a
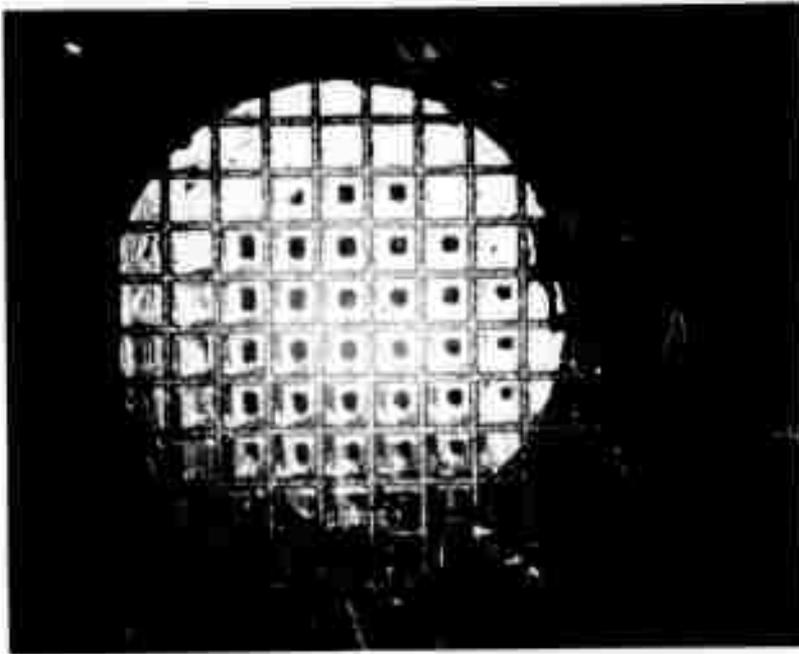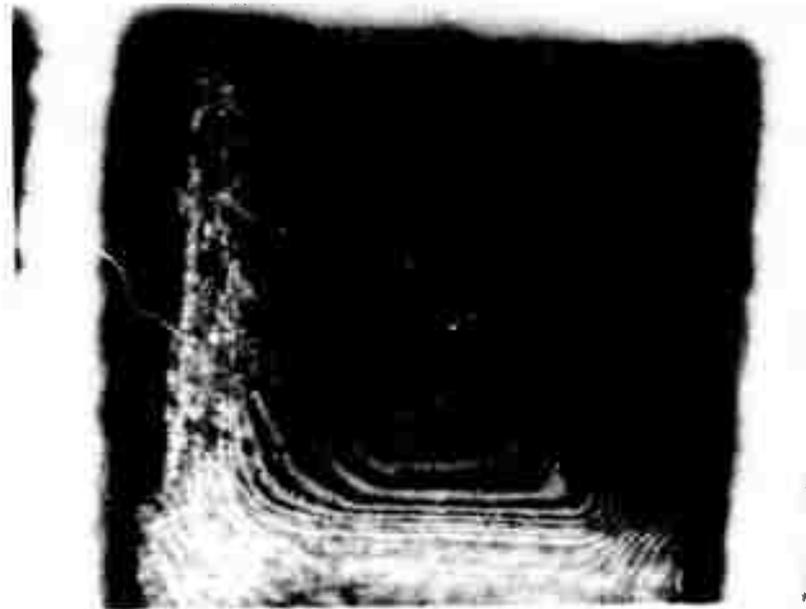
b

Figure 6. Optical Micrograph of Thinned (0001) Aℓ$_2$O$_3$ (Sample No. 4, Sodium Light) (a) 25X, (b) 450X

TABLE X.
Samples Thinned by Ion-Beam Sputtering.
(All samples are Al_2O_3 unless noted otherwise)

Sample Number	Orientation	Ion Energy (kV)	Incidence Angle (degrees)	Average Thinning Rate (μm/hr)	Thickness Change (μm)	Actual Sputtering Time (hours)	Total Time Involved in Run (days)
1	$(10\bar{1}4)$	4	30	0.13	21.5	164	56
2	$(01\bar{1}2)$	8	30	0.29-1.4	49	35	8
3	(0001)	6	30	0.45	5.2	11.6	2
4	(0001)	6	30	0.56	5.5	9.8	1
5	(0001)	6	30	0.53	5.3	10.0	1
6	$(10\bar{1}4)$	8	30	0.81	84	104	16
7	$(10\bar{1}4)$	6	10	0.30	84	281	23
8	(111) (Spinel)	6	30	0.57	6.4	11.2	2
9	$(10\bar{1}4)$	8	10	0.22	84	381	43
10	$(01\bar{1}2)$	6	30	0.54	58.5	108	14
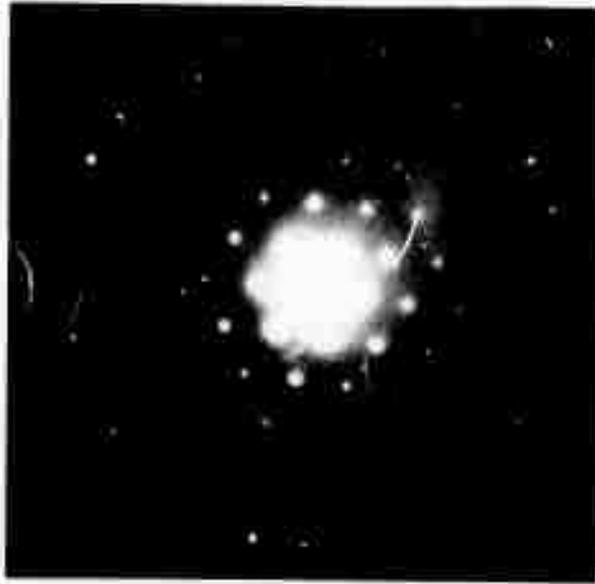
Figure 7. Electron Diffraction Spot Pattern from (0001) Al_2O_3 (Neg. 1362)
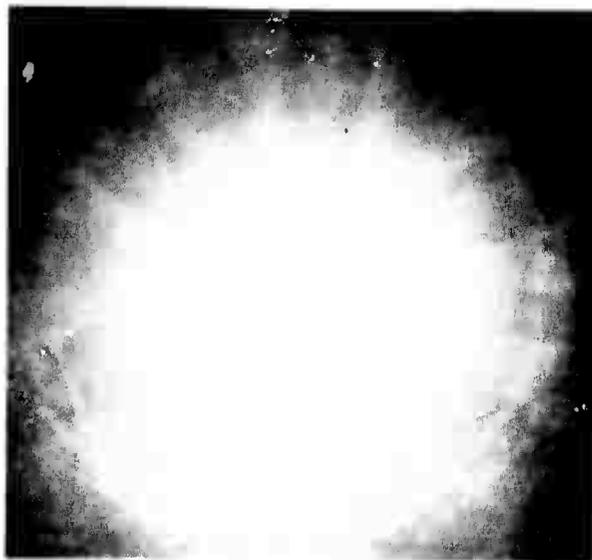
Figure 8. Electron Diffraction Kikuchi Pattern from (0001) Al_2O_3 (Neg. 1360)

Figure 9.   Electron Diffraction Spot Pattern from (01$\bar{1}$2) Aℓ_2C$_3$ (Neg. 1506)

Figure 10.   Electron Diffraction Kikuchi Pattern from (01$\bar{1}$2) Aℓ_2O$_3$ (Neg. 1510)
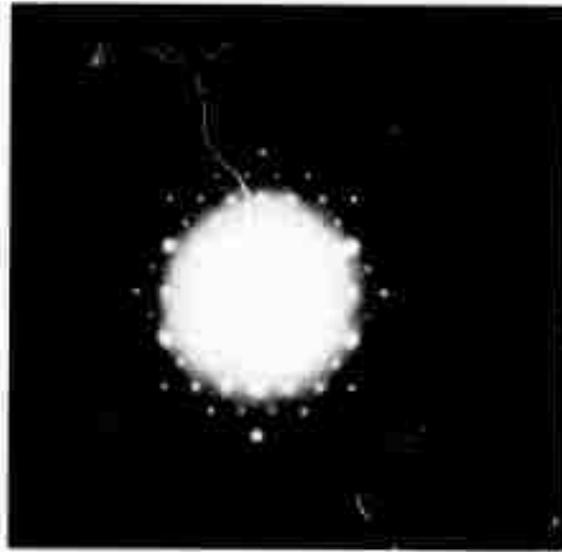
Figure 11. Electron Diffraction Spot and Kikuchi Pattern from $(10\bar{1}4)$ Al_2O_3 (Neg. 1504)

1.0µ
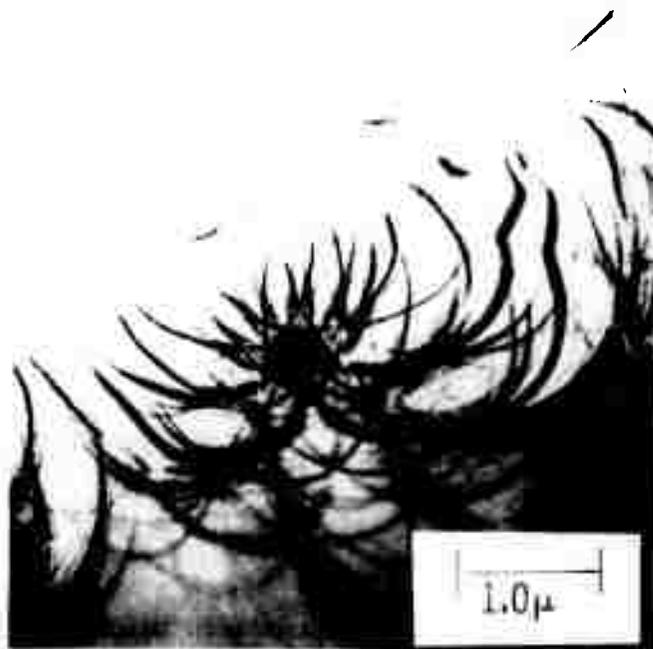
Figure 12. Electron Micrograph of (0001) Al_2O_3, Sample No. 3 (Neg. 1346)

Figure 13.   Electron Micrograph of (0001) $A\ell_2O_3$, Sample No. 3 (Neg. 1356)

Figure 14.   Electron Micrograph of $(10\bar{1}4)$ $A\ell_2O_3$, Sample No. 7 (Neg. 1450)
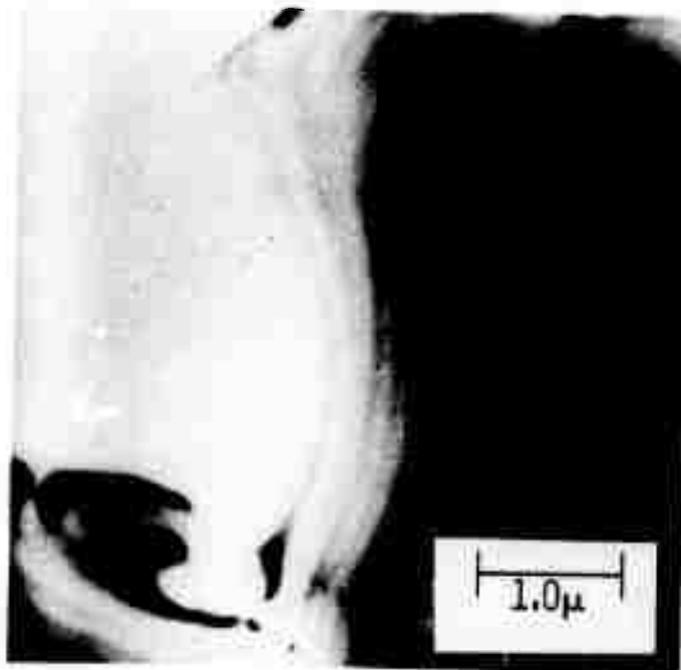
Figure 15. Electron Micrograph of (10$\bar{1}$4) Aℓ_2O$_3$, Sample No. 7 (Neg. 1453)
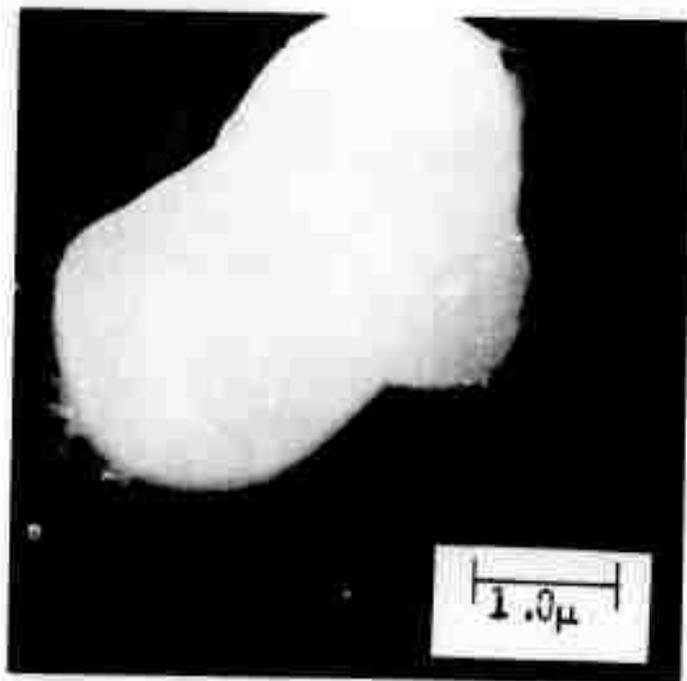
Figure 16. Electron Micrograph of (10$\bar{1}$4) Aℓ_2O$_3$, Sample No. 9 (Neg. 1455)
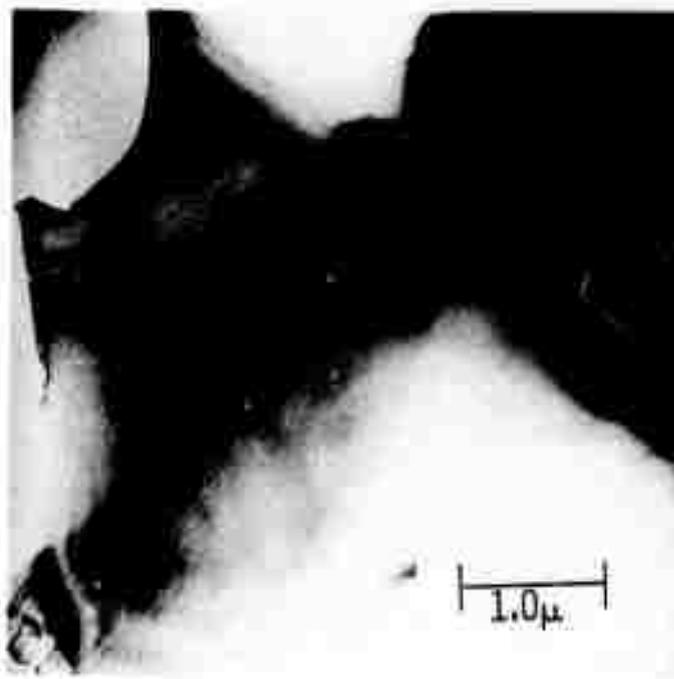
Figure 17. Electron Micrograph of (10$\bar{1}$4) Aℓ_2O$_3$, Sample No. 9 (Neg. 1456)

Figure 18. Electron Micrograph of (10$\bar{1}$4) Aℓ_2O$_3$, Sample No. 9 (Neg. 1517)
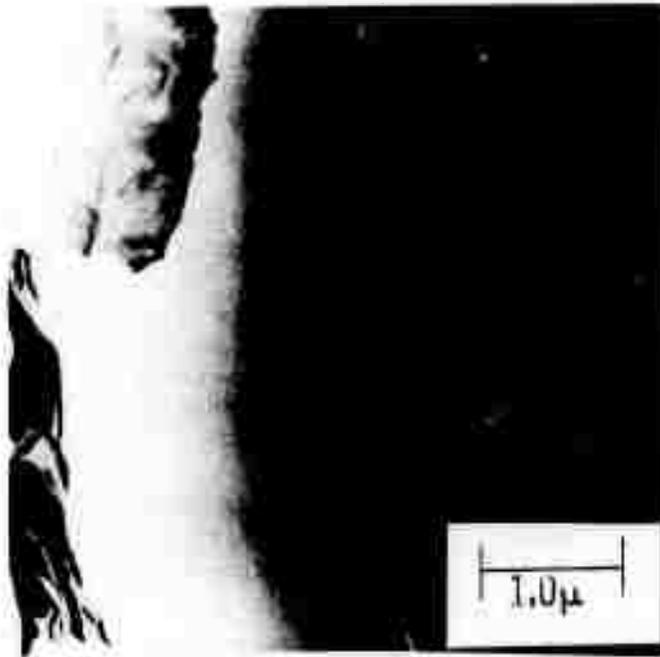
Figure 19. Electron Micrograph of (01$\bar{1}$2) Aℓ_2O$_3$, Sample No. 10 (Neg. 1514)

Figure 20. Electron Micrograph of (01$\bar{1}$2) Aℓ_2O$_3$, Sample No. 10 (Neg. 1515)

It is emphasized that the circular semisymmetrical patterns in these figures are not objects in the crystal but rather intersections of the extinction contours. This can be readily demonstrated by tilting the sample slightly during examination; the circular intersections then move about the crystal. The obscuring presence of extinction contours is best eliminated by producing uniformly thin, strain-free, unbuckled crystals by the ion-beam sputtering process.

Certain samples exhibit a surface structure after thinning; this is particularly noticeable in Figures 17 and 20. This semiregular, wavy or terraced structure is noticed on $(10\bar{1}4)$ and $(01\bar{1}2)$ orientations, but not on (0001) samples, which suggests crystallographic origin. However, their direction in Figure 17 does not appear to be crystallographic, and the structure does not appear on all samples or in all thin areas of the same sample. The surface structure is more pronounced in areas where the thickness gradient is least, suggesting a complex interaction between the crystalline sample and the ion-sputtering mechanism. The structure does not appear to be simply related to ion-beam energy or incidence angle. The origin of the structure is currently being investigated.

Many regions in the samples examined to date have a thickness gradient that is larger than desirable and hence are marginally suitable as substrates for in situ CVD. Thin regions with suitable large areas, such as shown in Figures 17 through 19, are seldom observed more than once per sample.

The magnitude of the thickness gradient has been analyzed by optical interferometry. The central thin region of a sample appears as in Figure 6b, when examined by monochromatic sodium light. The asymmetrical shape is the result of the bottom grid being slightly misaligned with respect to the top grid during thinning, as in Figure 6a. The thickness variation has a slope of 1:50, which appears to persist down to the thinnest regions, typified in Figures 12, 15 and 16. The thickness will vary from zero to 200 Å over a transverse distance of $\sim 1 \mu m$. In practice, the thinnest regions (0 to 50 Å) near a hole break off during handling.

One potential source of an excessive thickness gradient is obvious from Figure 6a. The grid partially shields some areas of the sample, the exact area being determined by the incidence angle and the thickness of the grid. If a hole becomes enlarged and the region examined is in the shadowed area, the thickness gradient will naturally be greater. This problem can be avoided simply by limiting electron microscopic examination to the unshadowed center of the grid square.

The area of the sample always exposed to the ion beam within a grid square during the thinning process may be calculated as follows. The 75-mesh grid has a repeat spacing of 338 μm, with open areas 268 μm wide not covered by the grid bars. The height of the grid (18 μm) causes some of the sample to be shadowed a portion of the time. At a beam angle of 30 deg, the area never in shadow is 205 μm x 205 μm, or 59 percent of the open area. At a beam angle of 10 deg the corresponding figure is 5 percent. If for some reason the grid is not in contact against the sample but is instead raised another 18 μm, for example, there is no region within a grid square that would be exposed at all times to a beam incident at 10 deg. The figures for other angles are listed in Table XI.

44

TABLE XI.
Size of Completely Unshadowed Area for Various Beam Incidence Angles in IBMA

Grid Height (μm)	Incidence Angle (degrees)	Length of Unshadowed Part of Grid Square (μm)	Percent of Total Grid Square Length Unshadowed (%)	Percent of Total Grid Square Area Unshadowed (%)
18	90	268	100	100
18	30	205	77	59
18	25	190	71	50
18	20	169	63	40
18	15	133	50	25
18	10	62	23	5
18	5	0	0	0
36	30	143	53	28
36	25	103	38	15
36	20	69	26	7
36	15	8	0.03	0.001
36	10	0	0	0
36	5	0	0	0

It is possible that a limiting but relatively steep thickness gradient is imposed on the sample by the ion sputtering process itself. Thin areas are more rapidly eroded than thick areas, and this fact alone may set the lower limit on the gradient attainable. A "thin" area would be one in which the sample thickness is the same order of magnitude as the ion penetration depth. The liklihood of a steep limiting gradient from the ion sputtering process itself is less because adequately thinned regions have indeed been obtained (e.g., Figures 17 and 19).

One feature found on both optical and electron micrographs of Al_2O_3 samples has been conclusively identified as an artifact of the ion etching technique, and that is the so-called protuberances. These approximately hemispherical bumps are visible in the optical photomicrographs of Figures 6 and 21 and the electron micrograph of Figure 13. These features range from 50 to fractions of a m ron in diameter, and about as high. They are caused by some form of contamination shielding the sample surface from the ion beam, thus preventing sputtering in that location. Figure 21 clearly shows that one source of such contamination is the wire grid used during thinning. Protuberances will form even if a grid is not used, however, for the sample holder is an unavoidable source of contamination. Protuberances are undesirable if present in large quantities because they create an irregular surface on the thinned sample. Their incidence can be reduced but not entirely eliminated by thorough cleaning, appropriate shields, and use of a small incidence angle. It is emphasized that the "objects" visible in Figures 12 and 14 are not protuberances but are intersections of extinction contours.

Figure 21. Optical Photomicrograph of Thinned (10$\bar{1}$4) Al_2O_3
(Sample No. 6, Sodium Light, 110X)

An interesting feature was observed in the micrograph of sample 9 (Figure 18). The large oblong particle and two smaller particles are inclusions originally present in the Al_2O_3 as a second phase. That they are inclusions and not particulate matter resting on the surface is determined by examining the extinction contours in the Al_2O_3 around the inclusion; at higher magnifications the strain brought about by their presence is revealed. The "fuzzy" appearance of the micrograph is not due to poor focus but rather to a contamination layer which had built up on the sample during the prolonged time it was examined. Residual hydrocarbon vapors from the microscope were polymerized by the electron beam into a carbonaceous deposit.

The thinning of a crystal by ion-beam sputtering is a slow process, with removal rates from 0.1 to 2.0 μm/hr. Variables affecting the removal rate include sample material, crystallographic orientation, ion-beam energy, incidence angle of beam with respect to sample, alignment of beam and sample, and stability of the ion beam. The limited number of samples thinned to date cannot provide definitive conclusions, but preliminary results suggest the differences due to the first three variables are not of major importance.

The thinning rates of samples 7 and 9 (Table X) indicate a definite trend toward reduced thinning rates at lower angles of incidence. If it is desired to minimize the presence of protuberances on the sample, a smaller incidence angle is necessary, but this has the practical disadvantage of increasing considerably the required processing time.

The profile of the ion beam has been determined by thinning a large Al_2O_3 wafer (sample 2 in Table X). The beam has conical symmetry, with the most intense region along the axis of the ion gun. The 1.3 cm dia sample had a saucer-shaped surface after thinning, with a 3.5-mm dia region 49 μm deep approximately in the center, tapering to 10 μm deep near the edges. In the deepest region the removal rate was 1.4 μm/hr, while at the edges the rate was 0.3 μm/hr.

The deepest region was located ~1 mm from the geometric center of the sample, indicating a misalignment by this amount of the center of rotation of the sample and the axis of the ion beam. For most samples this misalignment is unimportant; however, for samples smaller than 1 mm dia it means the sample will be out of the most intense portion of the ion beam for a fraction of the time during rotation, making the effective thinning rate lower than normal.

From an operational standpoint, beam stability is an important factor, for it determines the degree to which the machine will run unattended. As thinning proceeds, sputtering occurs not only from the sample but also from the holder, beam shields, and cathode as well, and the sputtered material is deposited elsewhere in the system. In particular, material from the cathode may deposit between the anode and cathode, causing a short circuit and automatic shut-off of the apparatus. When this occurs during attended operation the machine can be turned on again and will operate for 5 to 120 min before again arcing, but during unattended operation this operating time is lost. Arcing can be prevented by thoroughly cleaning the ion gun, but since this requires ~1 hr of down-time for every 20 to 50 operating hours, an economical operating "duty-cycle" must be selected.

Sputtering of the cathode occasionally generates a more serious problem. The original cylindrical beam exit canal normally becomes conical in operation due to the erosion by the beam but it may become skewed. In this case the most intense portion of the ion beam does not strike the sample and the thinning rate is reduced. The reduced thinning rate of sample 9 (Table X) is partially the result of this effect. The cathode canal normally increases in size until the cathode must be replaced (typically after 100 to 200 hr of operation), but replacement may be required earlier if the canal becomes skewed.

5. SUBTASK 5. STUDIES OF IN SITU FILM GROWTH IN THE ELECTRON MICROSCOPE

In the first year of the program many of the modifications required in the electron microscope for in situ observation of the nucleation and early-stage growth of CVD semiconductor films on insulating substrates were completed. Provision for motion picture recording of film growth was assembled and tested, and the heated specimen stage was installed and tested. The first in situ PVD experiments were carried out. During the first half of the second year a series of electron microscope modifications and tests was completed, culminating in a series of successful PVD experiments inside the electron microscope. $A\ell$ was deposited onto a heated carbon substrate and a sequence of micrographs taken during the growth process, demonstrating the feasibility of performing in situ nucleation and growth studies in this equipment.

A transmission phosphor screen (for the motion picture camera) was installed, permitting motion picture photography which does not interfere with the normal still photography. The auxiliary vacuum pumping system for the specimen chamber was fabricated, installed and tested. The basic vacuum system of the microscope itself was improved by addition of a cooled baffle, by polishing numerous O-ring grooves, and by thoroughly cleaning the microscope interior. A PVD source assembly was fabricated, installed, and used in conjunction with the specimen heater to perform the above PVD experiments. Calculations and design for the CVD microchamber were completed and fabrication of the chamber and the differential pumping apertures was begun. Work was also begun on the production of thin (200 Å) $A\ell_2O_3$ crystals required as substrates for the in situ CVD studies.

Effort on this subtask has been divided between two major areas during the past six months: (1) design and construction of the CVD microchamber and associated hardware, and (2) conducting a large number of PVD experiments to test and demonstrate various experimental situations to be encountered in the in situ chemical vapor deposition experiments. A new design for the CVD microchamber was completed, superior in many respects to that described in the previous semiannual report (Ref 3). Fabrication and assembly of the microchamber is essentially complete, with testing scheduled for the first month of the third-year program. A CVD flange to provide the gas inlet and electrical feedthroughs for the microchamber has been fabricated and leak tested.

Numerous in situ PVD experiments have been conducted during this period, with both $A\ell$ and Au being deposited onto amorphous carbon substrates. These experiments are still not fully satisfactory, so have not been documented on motion picture film. The major problems have been the result of shortcomings in the PVD heating stage, coupled with a contamination problem in the microscope and the lack of a suitable transmission phosphor screen.

a. Design and Construction of <u>in situ</u> CVD Microchamber

The present design of the CVD microchamber is shown in a cutaway drawing in Figure 22 and a photograph in Figure 23. The substrate is held between two resistively heated grids which are held by screws in contact with inner and outer electrodes. The sample and the grids are totally enclosed in a thin cylindrical region, vacuum-tight except for the gas inlet and two apertures (for the electron beam entrance and exit). The SiH_4 gas enters the microchamber through a coiled gas inlet tube, surrounds the sample, and exits via the two apertures. The microchamber has a gas layer thickness of 1.6 mm through which the electron beam must pass.

Certain constructional details (Figure 22) of the CVD microchamber are of interest. The center electrode contains a 0.004-in. drilled hole to permit the electron beam to enter and a limited amount of gas to exit. A raised projection contains a tapped hole for the No. 40 National Miniature (NM) screw (0.016-in. dia, 254 threads per in.) which holds one end of the heating grid. The center electrode is brazed into a base which is an extensively modified AEI-EM6 electron microscope specimen holder.

One end of a coiled copper gas inlet tube is brazed into the center electrode base, and the other end is joined to the CVD flange by a "Swaglok" tubing connector. The flat portion of the base is slotted to permit gas to flow from the inlet tube to the annular space between the inner and outer electrodes and then to the specimen. The center electrode is beryllium copper, selected for its superior machining characteristics over those of pure copper, which is unsuitable for drilling and tapping the miniature holes required. As anticipated, some difficulty occurred in brazing the beryllium copper to the pure copper base, but the problem has been adequately solved.

The outer electrode is attached, by means of three No. 80 NM flat-head screws (0.032 in. dia, 127 threads per in.), to the lava insulator which in turn is fastened to the base with four No. 80 NM fillister-head screws. The lava insulator was machined somewhat oversize in the unfired, soft condition, then fired, ground flat, and lapped to a 2-microinch surface finish. The bottom of the outer electrode and the flat portion of the center electrode base were also lapped to a 2-microinch surface finish so that the assembly is gas tight at these joints when assembled. This portion of the microchamber need not be disassembled to load or unload specimens.

The outer electrode has a projection containing a small tapped hole which accepts the No. 40 NM screw holding the other end of the heating grid. A threaded cap over the outer electrode holds a thin removable copper aperture disc in place. The outer electrode and cap are made of Ti, selected for its machinability, nonmagnetic properties, and low vapor pressure at elevated temperatures.

It was originally anticipated that stainless-steel screws would be used to attach the heating grid to the electrodes. However, use of similar screws in the PVD experiments has revealed a small trace of ferromagnetic material in the essentially nonmagnetic screws; this creates a distorted magnetic field in the vicinity of the specimen and prevents attainment of maximum resolution of the electron microscope above 20,000X. Various heat treatments have failed to reduce the ferromagnetic content of the stainless-steel screws, so specially machined Ti screws have been made.

49
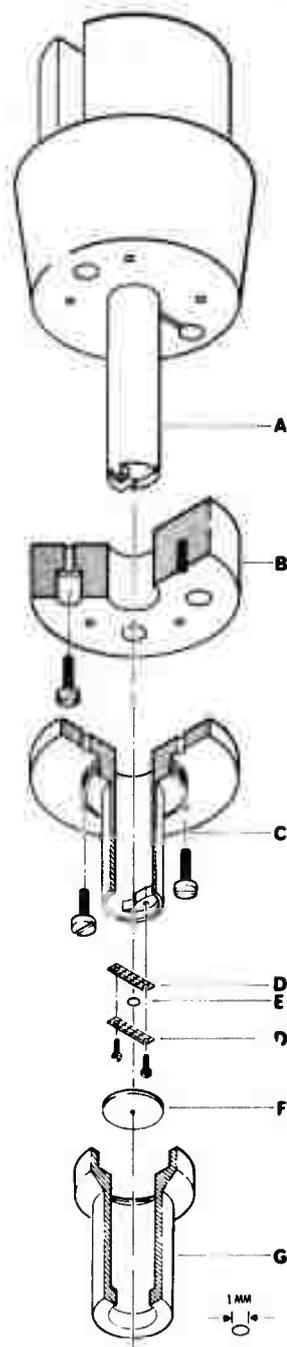
Figure 22. <u>In Situ</u> Chemical Vapor Deposition Microchamber.
(A, center electrode and gas limiting aperture; B, lava insulator; C, outer electrode;
D, heating grids; E, sample; F, removable aperture; G, aperture cap.)

50
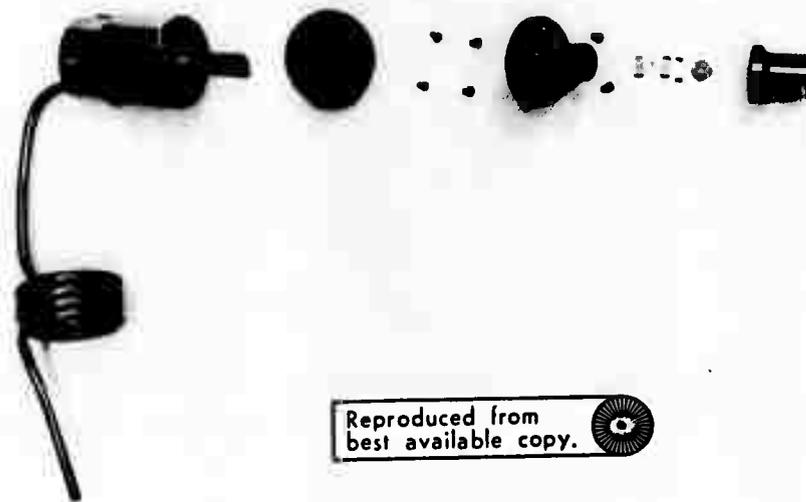
Figure 23. Microchamber for in situ CVD Experiments

b. In situ PVD Experiments with Aℓ

The Aℓ PVD experiments initiated in the first six months of the second year have been continued. The Aℓ is evaporated from a specially constructed filament mounted inside the microscope onto an amorphous carbon film heated to ~300 C by a resistively-heated stainless-steel support grid. A sequence of electron micrographs taken during the course of one such in situ experiment is shown in Figure 24a through 24f. The first photograph in the series is that of the original substrate prior to nucleation; the particles visible are dust particles, not Aℓ nuclei. They act as reference points so that exactly the same area can be located in the subsequent photographs.

Several important aspects of thin-film growth can be observed in these micrographs. Locations A and B in Figures 24b and 24c illustrate the formation of a grain boundary in a large crystal formed from several smaller crystals. Various contrasts visible at A in Figure 24b indicate that a number of differently oriented crystals are present. (The loss of resolution in reproducing the original photographs here may make discrimination of individual nuclei difficult, but they are readily discernible in the original micrographs.) Only three of the orientations survived the coalescence process; the remainder not visible in Figure 24c have been absorbed, atom by atom, by their neighbors. Note that at A both orientations have apparently grown at approximately the same rate.

51
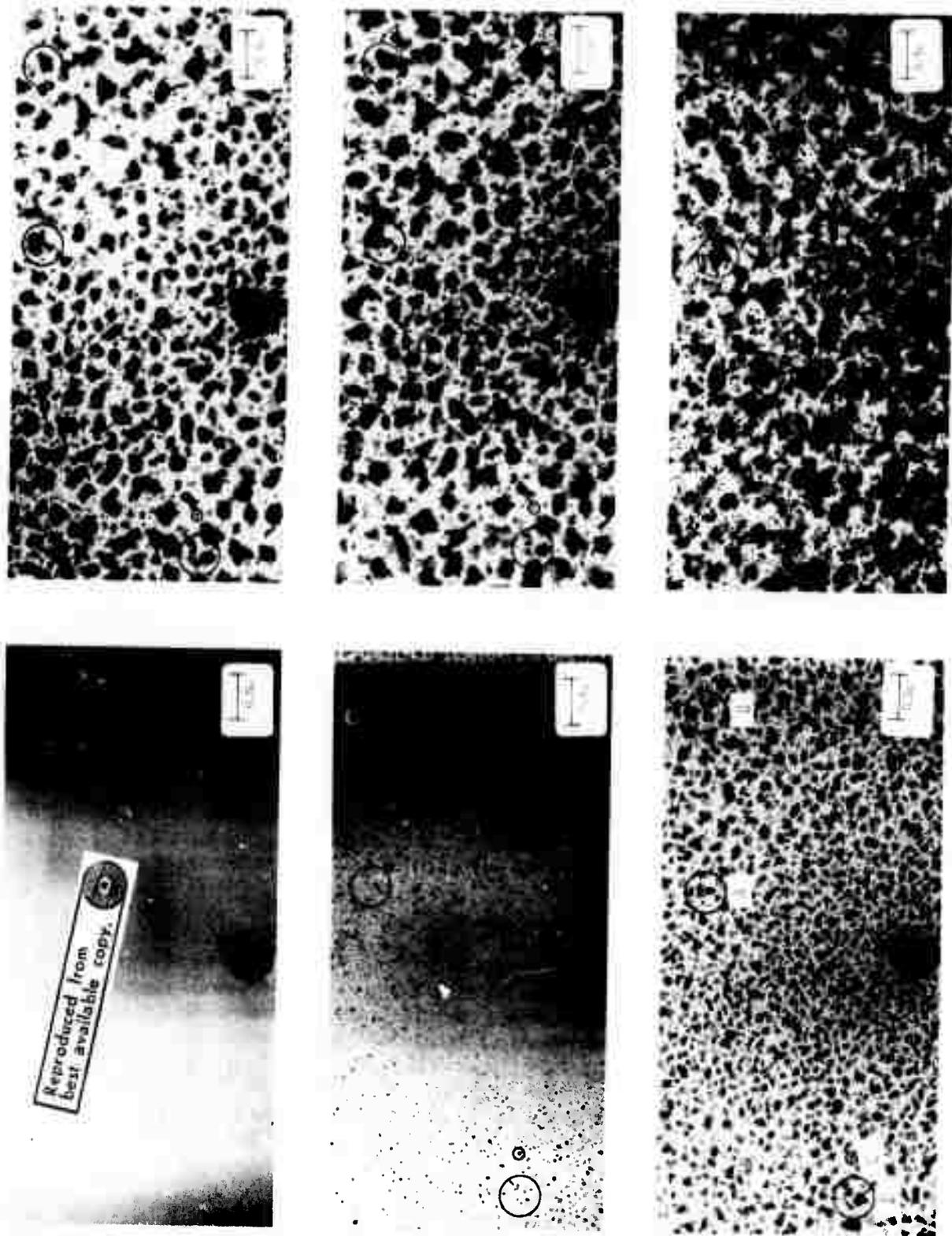
Figure 24. Sequence of Electron Micrographs Recorded during $A\ell$ PVD at Times of (a) 0 sec, (b) 110 sec, (c) 130 sec, (d) 150 sec, (e) 190 sec, (f) 10 min Oxidation.

52

At B, it is seen that the original crystals grew at different rates, resulting in one orientation becoming dominant. The dark portion of the top crystal in Figure 24c is almost completely developed in Figure 24b, and no further growth has occurred except in the light portion. The bottom crystal, however, shows the reverse behavior. (All four crystals are of different orientations.) Note at location C that not all crystals have grown at the same rate. At location D, the large extent to which rearrangement occurs during film growth is visible.

Some areas of the substrate originally covered with Aℓ may become bare when several islands coalesce and secondary nucleation will then occur in these bare areas. Such an area can be seen immediately outside and to the upper left of location B in Figures 24c and 24d. The presence of secondary nuclei causes some of the apparent "clutter" in the photographs; the remainder is caused by oxidation of the Aℓ.

Aℓ deposition was stopped after 190 sec in this particular experiment but the substrate and deposited film were permitted to remain at an elevated temperature for an additional 10 min. Almost total oxidation of the Aℓ occurred, completely changing the character of the film. All the O_2 required for the reaction was supplied by the residual O_2 and water vapor present in the electron microscope vacuum of $<1 \times 10^{-5}$ torr. Much of the water vapor originates in the photographic plates used for still pictures, a problem which can not be eliminated until the external motion picture camera system has been made to operate satisfactorily. In view of the serious oxidation problem with Aℓ deposits, no further in situ PVD experiments with this material are being performed.

c. In situ PVD Experiments with Au

When Au was deposited inside the microscope, an interesting effect was noted. The nuclei were extremely small in that area of the substrate exposed to the electron beam. The resulting Au film was extremely fine-grained in this region, but considerably larger-grained outside the irradiated area. Various repeats of the earlier experiments yielded the same final results, an example of which is shown in Figure 25. Figure 25a shows the region visible during the experiment. Figure 25b, taken after completion of the experiment, shows an adjacent area which was outside of the field of view and not struck by the electron beam during the deposition experiment. Figure 25c is a lower magnification view taken with the electron beam expanded to include both of the areas shown in a and b.

In addition to the restricted size of the Au nuclei, the substrate region irradiated by the electron beam was darkened by a deposit of hydrocarbon contamination. The deposit is formed from residual hydrocarbon vapors in the microscope striking the substrate and becoming polymerized by the incident electron beam. The carbonaceous deposit thus formed gradually builds up, eventually obscuring the sample being examined. Hydrocarbon vapors which strike the sample outside the area irradiated by the electron beam will reevaporate without effect. These residual hydrocarbon vapors, present to varying extent in all electron microscopes, originate from the vacuum oils and greases used in the pumping system, sealing gaskets, organic insulation on interior electrical wires, fingerprints, and residues of cleaning solvents.

The first hypothesis presented for the unusual nucleation behavior was that, for some unknown reason, the microscope contamination rate had increased greatly between the final Aℓ PVD experiment and the first Au PVD experiment. The diffusion of individual Au atoms on the sample surface – and thus the rates of the nucleation, growth

53
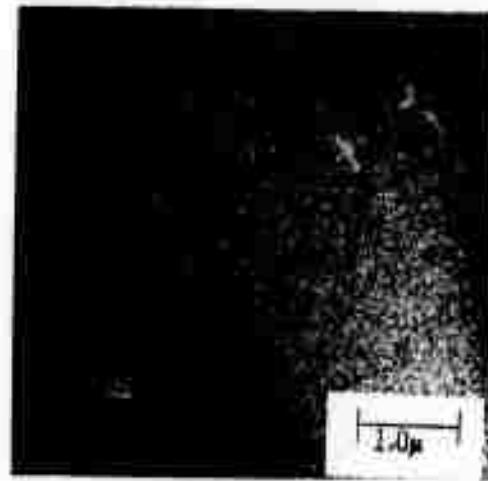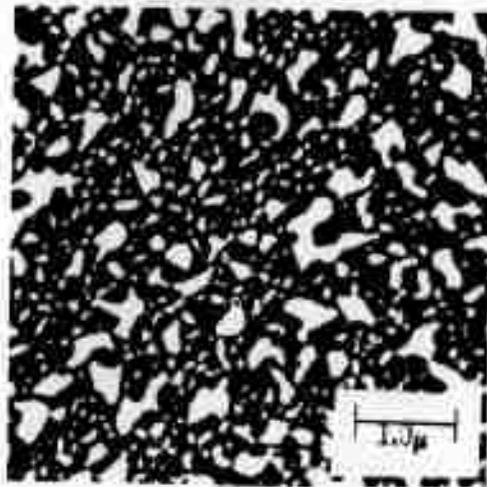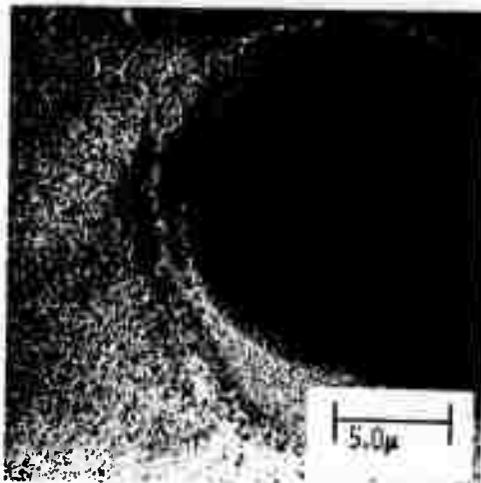
Figure 25. PVD Au Film Grown in Electron Microscope.
(a) Region Observed during Growth; (b) Adjoining Region not Irradiated
by Electron Beam; (c) Lower Magnification View of Regions of (a) and (b)

54

and coalescence stages – would then be seriously affected. However, this hypothesis was discarded when the contamination rate was remeasured and found to be 140 Å/min, only slightly larger than previously measured values.

Since the contamination rate decreases rapidly with increasing temperature, it was logical to question if the substrate was actually being heated to the intended temperature of ~500C (at which temperature the hydrocarbon vapors adsorbed on the substrate are thermally reevaporated before the electron beam polymerizes them). Examination of the substrate heater revealed a partial short circuit, which had resulted in reduced heater grid current and correspondingly lower temperature. Repair of the heater stage reduced somewhat the abnormal nucleation behavior, but it did not completely eliminate the effect.

The heating stage was again repaired, this time to improve the electrical contact between the heating grid and the electrodes. The original cap, which made pressure contact to the grid, was removed and No. 70 NM screw threads were tapped directly into the electrodes. Testing in the electron microscope indicated a loss of resolution which prohibited usage above ~20,000X. As mentioned earlier, the stainless-steel screws apparently contained a trace of ferromagnetic material which distorted the electromagnetic field of the objective lens around the specimen. Various heat-treating procedures failed to reduce the ferromagnetic content appreciably, so nonmagnetic Ti screws are being used.

Experiments have continued with the same results; greatly altered Au nucleation and growth behavior still occurs in regions irradiated by the electron beam. Two hypotheses are currently being considered: (1) Au nucleation and growth are intrinsically more susceptible to contamination effects than for Aℓ, and (2) the substrate is still not making adequate thermal contact with the heating grid. The first suggestion is intuitively difficult to accept and appears contrary to the experimental evidence of related nucleation and growth studies. Furthermore, it would be indicated only upon elimination of all other possible causes. Experiments are currently underway to test the second hypothesis, with no results to date.

d. Characteristics of Transmission Phosphor Screens

The transmission phosphor screen is an integral component of the motion picture recording set-up on the modified AEI EM6 electron microscope. It is a glass plate with a coating of an electron-activated phosphor material on the side internal to the electron microscope, e.g., the vacuum side. To date, five screens from three manufacturers have been tested; one of these is marginally adequate but the others have been unsuitable.

The first four screens tested used a "P11" phosphor coated with a thin layer of Aℓ to prevent charging by the electron beam. The P11 phosphor was chosen because its maximum spectral efficiency occurred in the blue at 0.46 μm, nearly the wavelength to which Kodak RAR 2479 film is most sensitive. The intensity available on the screen, even when struck with a maximum-intensity electron beam, was inadequate to obtain an image on the film using a Switar f1.6 lens and a shutter speed of 1/30 sec. Presumably the phosphor layer and/or the Aℓ coating was too thick. In addition, the resolution was less than desired, due either to a large phosphor grain size or to structure in the Aℓ coating.

The best screen tested to date is of S2 green F2 phosphor material coated with a conducting layer of amorphous carbon. The resolution is more than adequate. The intensity is better than that obtained with previous screens and is just sufficient to record images on the film when the developing process is "forced," i.e., the developing time extended.

The camera lens and film being utilized are the best commercially available, so solution of the problem appears to be in increasing the exposure time of a single frame. This has the unattractive feature of requiring a more elaborate and more costly (but commercially available) motion picture camera. This alternative is now being pursued.

6. SUBTASK 6. EVALUATION OF FILM PROPERTIES

During the first year, the routine evaluation of film properties was carried out by established methods of X-ray and electron diffraction analysis, metallographic analysis, and electrical measurements of transport properties. In addition, a new technique for evaluating the characteristics of the interfacial region of heteroepitaxial films was developed, involving measurement of the photoelectron emission from monochromatically-illuminated films in the MIS configuration on insulating (viz., Al_2O_3) substrates. Relatively large photocurrents due to electron transport through thick (~10 mils) single-crystal Al_2O_3 substrates were measured as a function of photon energy. Photoelectric threshold energies, escape length (mean free path) of excited electrons, and band bending in the semiconductor film adjoining the interface were determined in the Si/Al_2O_3 and $GaAs/Al_2O_3$ systems. Observation of the energy spectrum of back-scattered proton or alpha-particle beams injected in channeling directions in heteroepitaxial semiconductor films was also investigated as a means of measuring the density and the location of structural defects in the films. Experiments indicated that Si/insulator films have less imperfect interfacial regions than do GaAs/insulator films. The best structures of those examined to date were found in (100) Si films on (01$\bar{1}$2) Al_2O_3 substrates and in (111) Si films grown on near-(11$\bar{2}$0) Al_2O_3 substrates.

In the first six months of the second year the study of the effects of changes in deposition parameters on Si/Al_2O_3 film properties continued. These studies led to considerable insight into the factors which most profoundly influence film quality, and identification of conditions for optimized film growth on the various Al_2O_3 orientations progressed well. The importance of reactor geometry was recognized and demonstrated. The extent of Al autodoping from the substrate was established, and appropriate annealing procedures for minimizing these effects were determined. The use of new Al_2O_3 orientations for Si growth led to substrates which yielded epitaxial films of as good or better quality than those previously obtained. The measurements of photoemission of electrons from heteroepitaxial semiconductor films and transport of electrons in Al_2O_3 was carried further; work functions of additional metals were determined, and the mechanism of electron transport through the insulator was studied further. Measurements of high-field transport properties of Si and GaAs heteroepitaxial films were also initiated in that period.

During the past six months a major part of the contract effort has been expended on this subtask. The specific areas investigated, described in further detail below, include (1) a study of the variation in the electrical properties of Si/Al_2O_3 with temperature; (2) an extensive study of the anisotropy of the electrical properties of Si films on Al_2O_3, involving both theoretical (see Subtask 1) and experimental investigations; (3) an evaluation of the electrical properties of Si films on $MgAl_2O_4$

56

substrates; (4) further evaluations of the electrical properties of Si/Al_2O_3 to establish parametric relationships among temperature, growth rate, and substrate orientation; (5) further study of the photoelectric effects observed in the Si/Al_2O_3 system, particularly in the Al_2O_3 substrates; and (6) investigation of the high-field transport properties of heteroepitaxial films.

a. Variation of Electrical Properties of Si/Al_2O_3 with Temperature

The availability of a computer program for the analysis of low temperature Hall-effect data has provided a technique for deducing information about electrically active impurities and defects in Si/Al_2O_3 films. This information, coupled with knowledge of the carrier scattering mechanisms in Si films that can be gained from low-temperature studies, has suggested a study of the feasibility of using low-temperature data as a measure of film quality and a means to assist in optimizing film growth. The first phase of this study, the detailed examination of two n-type Si/Al_2O_3 films, has been completed during this reporting period. The electrical properties of two As-doped n-type $Si/(01\bar{1}2)Al_2O_3$ films having thicknesses of 0.72 and 3.9 μm were measured between room temperature and ~40K. The growth conditions and substrates were identical for the two samples (with the exception of length of time of growth), so that a meaningful comparison of thin and thick Si films could be made. It was expected that any differences in electrical behavior in the two samples could be attributed to the difference in strain and/or defect structure in the two samples. After growth, both samples were annealed for a total of 1.5 hr in O_2 followed by a 2-hr anneal in N_2 at 1100C. (As determined previously, this annealing sequence assures the electrical deactivation of any Al impurities present in the film.)

The electrical characteristics of the two samples at room temperature are shown in Table XII along with data on bulk single-crystal Si obtained from the literature (Ref 13). The major differences to be noted are those in the mobilities of the thick sample (~470 cm^2/V-sec), the thin sample (~290 cm^2/V-sec), and bulk Si (~1400 cm^2/V-sec). Although the room-temperature mobilities of the two Si/Al_2O_3 samples are not grossly different there is a marked difference in the variation of mobility with temperature. As can be seen from Figure 26, the thicker sample initially shows an increasing mobility with decreasing temperature and becomes nearly temperature-independent from 100 to 40K. The mobility of the thin sample is nearly constant from 300 to 100K, but decreases with decreasing temperature from 100 down to 40K. These data suggest that the ratio of the low-temperature to the room-temperature mobility may be a good measure of the extent of defect structure. Accordingly, this ratio has been computed for 77 and 300K (temperatures easily obtained in the laboratory) and has been included in Table XII.

The variation of net carrier concentration with temperature appears to be slightly different from that obtained for bulk samples; smooth experimental curves are plotted in Figure 27 for the 3.9μm-thick sample and for bulk Si. The difference in shape between the two curves is manifested in the different values for the parameters used to fit the data theoretically by the computer analysis discussed in the Second Semiannual Report (Ref 2); these parameters are given in Table XII. The smaller energy level E_D found for the As donor in the Si/Al_2O_3 samples compared with that for bulk material is primarily a result of the difference in the slopes of the curves in Figure 27 at low temperatures. Another significant difference between the properties of the bulk material and those of the epitaxial samples is in the effective mass, where there is an order of magnitude difference. This suggests that the mass may also be useful as a parameter for characterizing film properties.

57

TABLE XII
Electrical Charateristics of Two As-doped Si/(01$\bar{1}$2)Aℓ_2O$_3$ Films Used for Low-temperature Measurements

Sample Number and Thickness	Resistivity at 300K (ohm-cm)†	Net Carrier Conc. at 300K (cm^{-3})†	Mobility at 300K (cm^2/V-sec)†	N_D Donor Conc. (cm^{-3})	N_A Acceptor Conc. (cm^{-3})	Effective Mass m*	E_D Donor Energy Level (eV)	$\dfrac{\text{Mobility (77K)}}{\text{Mobility (300K)}}$
No. 11-4A-71 (LH-130) t = 3.9μm	0.64	2.1×10^{16}	470	2.4×10^{16}	2.6×10^{15}	$0.26m_o$	0.037	2.0
No. 11-2C-71 (LH-20) t = 0.72μm	1.5	1.5×10^{16}	290	1.7×10^{16}	1.3×10^{15}	$0.11m_o$	0.034	0.74
Bulk As-doped Si	-	1.75×10^{16}	~1400	$\sim 1.8 \times 10^{16}$	1.5×10^{15}	$1.2m_o$	0.048	5.7

†Numbers represent single determination of electrical parameter by standard technique.
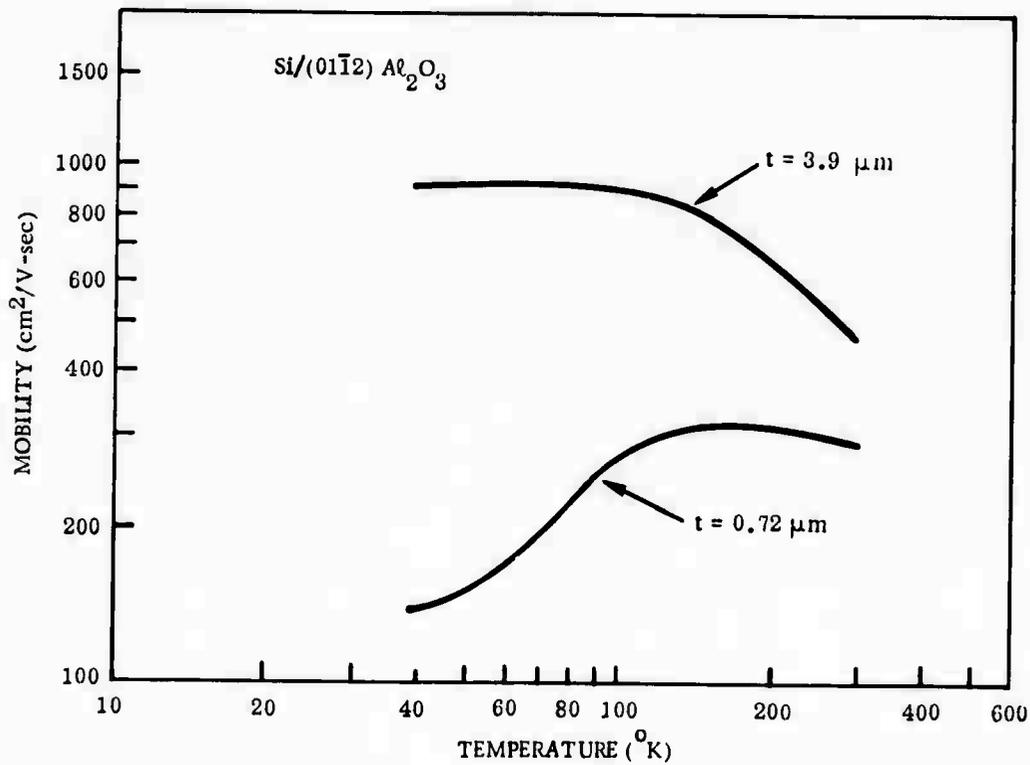
Figure 26.   Electron Mobility as Function of Temperature for Two Samples of
Arsenic-Doped n-Type Si/Aℓ_2O$_3$ Grown under Identical Conditions.
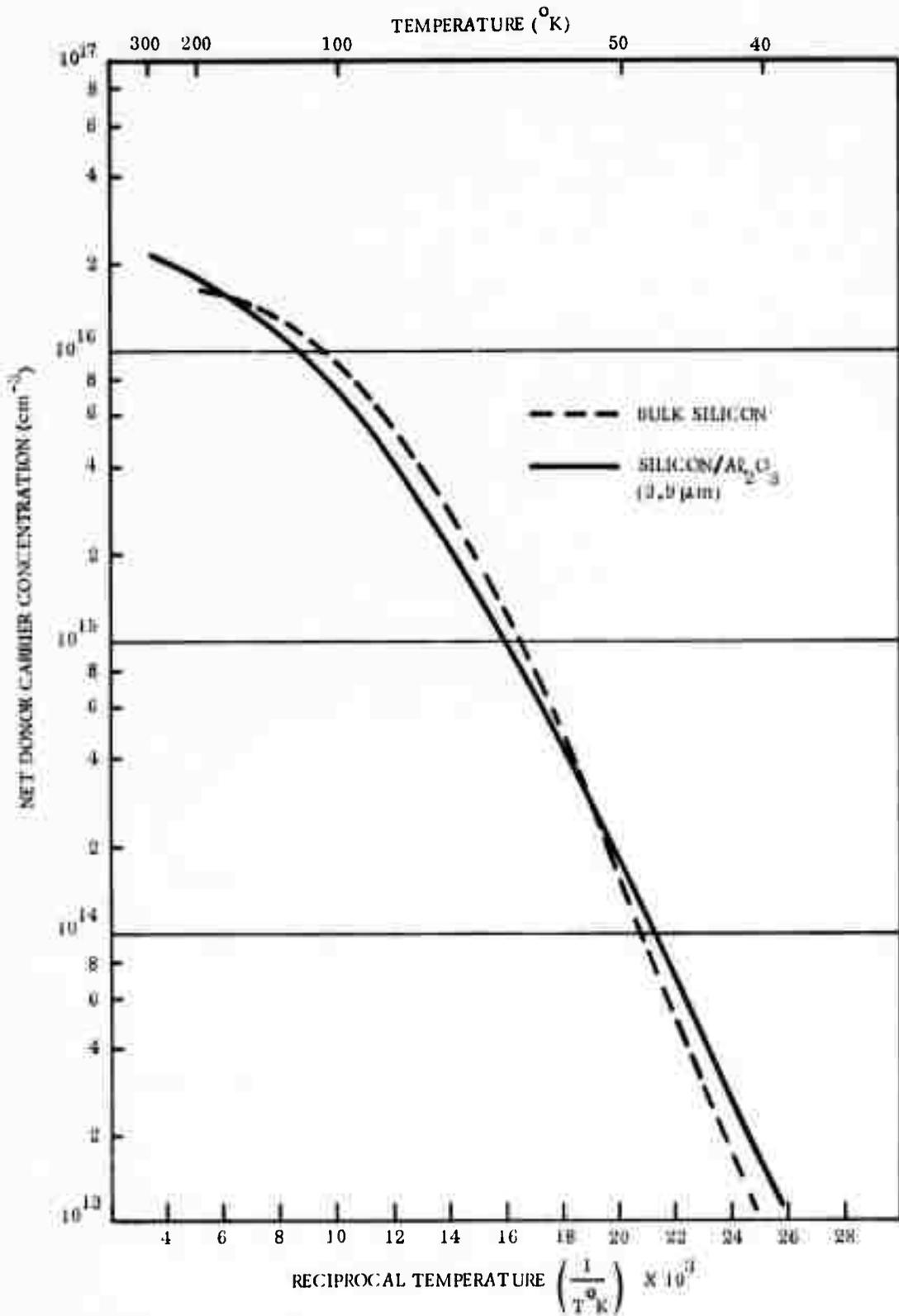
Figure 27. Net Carrier Concentration as Function of Temperature for 3.9μm-Thick Si/Aℓ₂O₃ Film and for Bulk Single-Crystal Si
(Smooth curves drawn through experimental data points)

60

It was originally intended that these measurements of carrier concentration might yield a value of minority carrier concentration (N_A for these n-type films) that could be related to defect structure. The slight difference in this parameter for the two films (thick and thin) shows this not to be the case. The negative result here is probably due to one of the following characteristics of the defect centers involved: (1) they do not act as acceptor centers; (2) they can act as both acceptor and donor centers; (3) they act as deep donors; or (4) they are electrically neutral. Additional measurements on p-type samples should indicate which of the first three is the more likely possibility. The fourth alternative is considered unlikely since defects appear to be too effective as scattering centers. It should be noted that if (2) is the correct explanation then the model used in the analysis of the data is not correct, and the resulting parameters, although possibly useful, are not physically meaningful.

It is important to attempt to understand the reason for the discrepancy in the activation energy deduced from the data. At the present time it appears that this result may be a consequence of inhomogeneous strain in the film. It is well known that strain can lower both the conduction-band minimum and the ground-state energy of an impurity. For large homogeneous strains these effects tend to lead to an increase in measured ionization energy; however, if the film has a high locally-inhomogeneous strain field, as might be expected with a large number of defects, the situation would be different. If, for example, the strain "smears out" the donor energy level and "smears out" or lowers the conduction-band minimum, the energy measured might then be expected to be lower than in an unstrained crystal or in a homogeneously strained crystal, and would be approximately equal to the amount the conduction-band minimum is lowered. Estimates of this shift have been given as ~0.015 eV (Ref 14) and from 0.040 to 0.070 eV (Ref 12), either value of which could easily account for the difference in As level of ~0.014 eV that is observed between the bulk Si value and that for the thinner film. Further experiments with films of different thicknesses should provide additional insight into this problem. The continuation of these studies has been temporarily postponed due to the importance of the anisotropy studies discussed below. It is anticipated that these studies, including measurements on p-type Si/Al$_2$O$_3$, will be resumed during the next reporting period.

b. Anisotropy in the Electrical Properties of Si/Al$_2$O$_3$ Films

A detailed examination of the variation of the electrical properties in the plane of Si heteroepitaxial films has been undertaken during the last report period, and has received the major portion of the effort devoted to Subtask 6. The results are potentially very significant to the preparation of heteroepitaxial semiconductor films for device use. Intensive study of these effects is still in progress, because of the amount of work involved and the importance of these results to the entire program.

The study to date has basically been in two areas: first, a study of anisotropy in a relatively low-symmetry Si plane, represented by the (221)Si/(11$\bar{2}$2)Al$_2$O$_3$ system; and second, a similar study of a high-symmetry plane, (100)Si/(01$\bar{1}$2)Al$_2$O$_3$. The two Si planes are basically different in the sense that the anisotropy in the (221) plane can be expected for any Si heteroepitaxial system, while the anisotropy seen in the (100)Si plane is a result of the anisotropic thermal expansion of Al$_2$O$_3$ and would not in general be present for (100)Si growth on other substrates - MgAl$_2$O$_4$, for example. The results obtained in these two areas are described in the following paragraphs.

The data reported below are from measurements taken on Si grown on an Al_2O_3 orientation ~3 deg from the $(11\bar{2}2)$ plane. Previous orientation studies have shown that $(221)Si//(11\bar{2}2)Al_2O_3$ and the $[\bar{1}10]Si//[1\bar{1}00]Al_2O_3$ in the plane of the film. For this experiment, As-doped films having thicknesses from 1.9 to 2.5 μm and net donor concentrations of $2-7\times10^{16}$ cm^{-3} were grown at 1100C at a growth rate of approximately 2μm/min. After growth, the samples were annealed in O_2 for 30 min followed by a N_2 anneal for 2 hr in order to stabilize film properties and electrically neutralize any Al impurities present in the film.

Electrical measurements were carried out on a specially designed double Hall-bridge pattern etched in the Si film using photolithographic techniques. This bridge pattern is shown in Figure 28. The legs in each bridge are spaced 72 deg apart and the two bridges are rotated with respect to each other by 18 deg. The bridge thus allows an independent measurement of Hall mobility (μ_H) every 18 deg in the plane of the film.

Plots of Hall mobility (μ) vs angle (θ) measured from the $[1\bar{1}0]Si$ direction are shown for representative samples in Figure 29. For each sample, a least-squares fit is obtained from a computer analysis by fitting the data to the equation $(\mu_H)^{-1} = a + b\cos 2\theta$ (see below). An anisotropy factor A can be defined according to

$A = (\mu_{max} - \mu_{min}/\mu_A) \times 100 = \dfrac{200b}{a}$, where μ_{max} and μ_{min} are the maximum and minimum mobilities determined from the least-squares fit, and $\mu_A = 1/2\,(\mu_{max} + \mu_{min})$. Table XIII shows the values of these parameters for a number of samples. The observed anisotropy is seen to be appreciable, as evidenced by an average room temperature anisotropy factor A of approximately 39 percent.

In order to explain this behavior the reduction in mobility due to the piezoresistance effect resulting from the difference in thermal expansion coefficients of Si and Al_2O_3 has been calculated. For the sake of completeness the difference in thermal expansion coefficients for Al_2O_3 parallel and perpendicular to the $[0001]$ axis has also been taken into account. Using representative values for the piezoresistance coefficients $\pi_{11} = -102$, $\pi_{12} = 54$, $\pi_{44} = -14$, $\times 10^{-12}$ cm^2/dyne, values of elastic constants $C_{11} = 16.5$, $C_{12} = 6.4$, $C_{44} = 7.93$, $\times 10^{11}$ dynes/cm^2, thermal expansion coefficients $\alpha_{Si} = 3.9 \times 10^{-6}$/deg C, $\alpha_{Al_2O_3}$ ($//c$) = 9.30×10^{-6}/deg C, $\alpha_{Al_2O_3}$ ($\perp c$) = 8.31×10^{-6}/deg C, and a temperature difference of 1100C over which the thermal contraction takes place, it is found that $(\mu/\mu_0)^{-1} = 1.06375 - 0.21891 \cos 2\theta$, where μ_0 is the mobility in the absence of stress and θ is defined as above. The theory predicts an anisotropy factor of 41 percent, in good agreement with the experimental values given in Table XIII.

An interesting feature of the piezoresistance in this plane is that the mobility is predicted to be larger than the unstressed mobility for 0 deg $\leq \theta \leq 37$ deg (if only the first quadrant is considered). At 37 deg, theory predicts that the mobility reduction due to thermal stress is zero, so that $\mu(37$ deg$) = \mu_0$. At this angle the experimental value of mobility can be used to estimate the mobility degradation due to causes other than thermally induced stress.
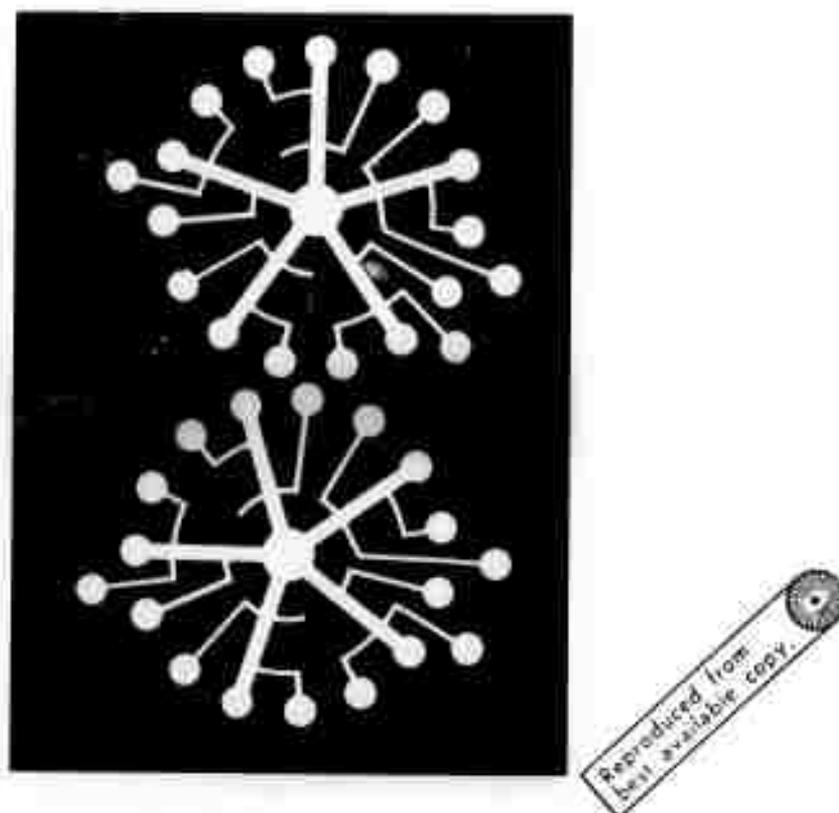
Figure 28. Double Hall-Bridge Pattern for Studying Anisotropic Electrical Parameters

TABLE XIII

Anisotropy Parameters of Several (221)Si/(11$\bar{2}$2) Aℓ_2O$_3$ Films

Sample No.	Temp (°K)	A (%)	μ_{max} (cm^2/V-sec)	μ_{min} (cm^2/V-sec)	μ_o (cm^2/V-sec)	RMS Error (%)
HJ-1	300	30.4	671	494	597	2.7
HJ-58	300	32.2	700	506	615	3.3
HJ-58	77	84.9	1900	769	1250	3.8
HJ-16	300	35.5	690	483	600	2.3
HJ-15	300	39.5	686	460	585	2.8
HJ-0	300	40.1	679	452	575	2.6
HJ-6	300	46.3	737	460	607	3.4
HJ-25	300	48.6	708	431	575	3.5
HJ-25	77	108.6	1680	497	900	6.0
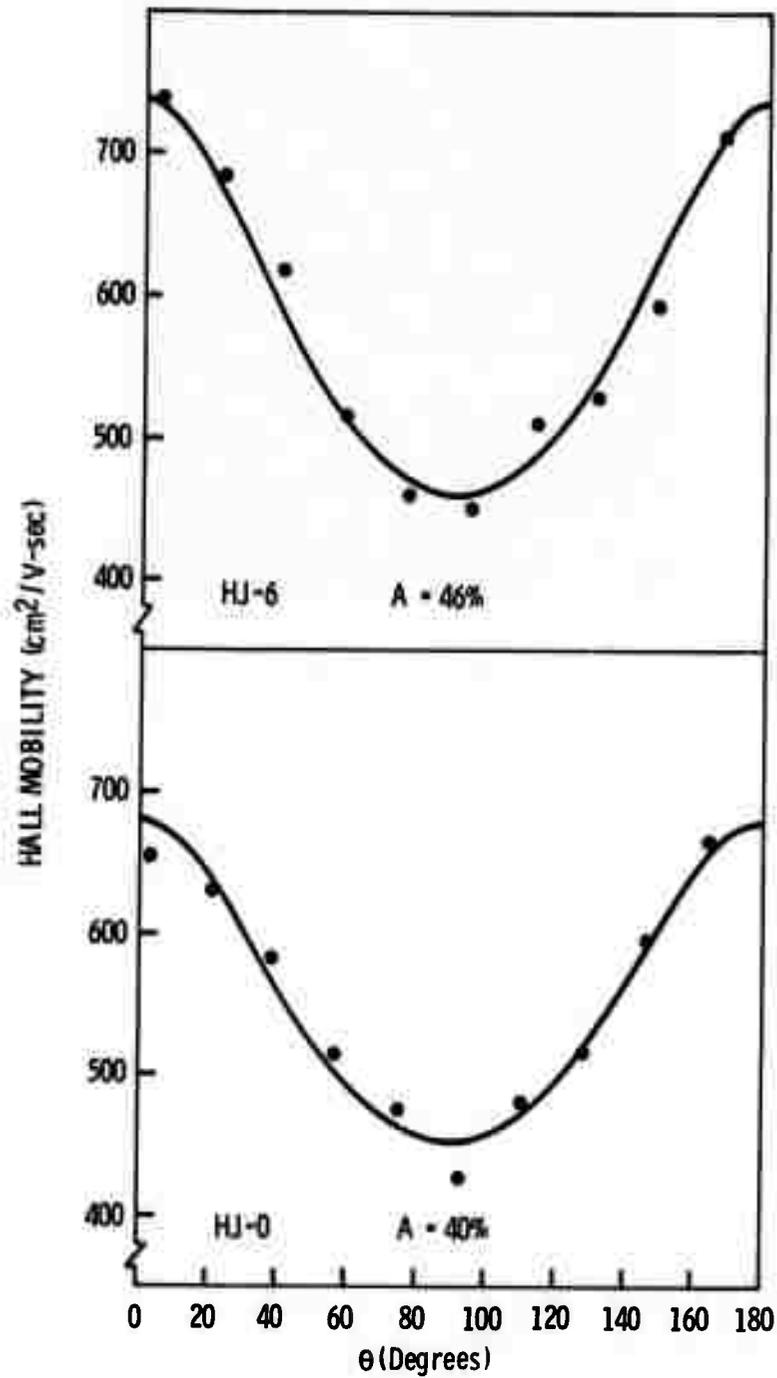
Figure 29. Variation in Hall Mobility as Function of Direction in $(221)Si/(11\bar{2}2)A\ell_2O_3$

64

If it is assumed that the film mobility at 37 deg (i.e., $\mu_0 \simeq 600$ cm^2/V-sec for the films used in this study) is given by $(1/\mu_0) = (1/\mu_B) + (1/\mu_D)$, where μ_B is the bulk mobility ($\simeq 1000$ cm^2/V-sec), then $\mu_D \simeq 1500$ cm^2/V-sec represents the limiting value of mobility due to all mechanisms other than thermally induced stress. However, μ_D probably is related almost entirely to defect structure in the film. The fact that the value of mobility μ_0 is much smaller than the bulk mobility strongly suggests that thermally induced stress is not the dominant mechanism in lowering the mobility.

The piezoresistance theory also predicts, in the absence of any externally applied magnetic field, an electric field in the plane of the film but orthogonal to the current direction. This transverse field E_T is given theoretically by $E_T/j\rho_0 = 0.21227 \sin 2\theta$, where j is the current density and ρ_0 is the resistivity in the absence of stress. Accordingly, this transverse field has been measured (across the same terminals used to measure the Hall voltage); the quantity $E_T/j\rho_0$ is shown plotted for two samples in Figure 30. The quantity ρ_0 is found from $\rho_0 = R_H/\mu_0$, where R_H is the Hall constant and μ_0 as before is the mobility at $\theta = 37$ deg. A least-squares fit of the data to the predicted equation yields an average value for the coefficient of $\sin 2\theta$ of 0.2, in good agreement with theory.

The temperature dependence of the anisotropy has not been examined in detail, although measurements on selected samples at 77K show a much larger anisotropy, as evidenced by the data in Table XIII. Such an increase is consistent with what might be expected for the variation of piezoresistance with temperature. Although detailed measurements of all of the piezoresistance coefficients are not available in the literature, π_{11} appears to be the order of three times greater at 77K than at 300K. If it is assumed that all of the coefficients vary by the same amount, it can be shown that the anisotropy factor A would be expected to be the order of 2.7 times greater at 77K. The data on two samples show an average increase of a factor of 2.4, consistent with that predicted.

The enhanced mobility predicted for some current directions suggests that the (221) plane of Si/Aℓ_2O$_3$ may yield superior electron mobilities. In comparison with (100)Si and (111)Si grown at this laboratory, the (221) plane has indeed yielded higher mobilities. It would be expected that some types of devices would show improved performance if oriented in such a way as to take advantage of this improved mobility.

Since the mobility is unaffected by thermal stress for one current direction in the (221) plane, insight may be gained into the scattering mechanisms in Si/Aℓ_2O$_3$ by judicious studies of the mobility versus temperature. For example, the comparison of such data at various angles may make it possible to separate the contributions of various scattering mechanisms to reduction in the mobility.

The films used for the study of the (001)Si/01$\bar{1}$2)Aℓ_2O$_3$ system were grown in two different reactor systems. One of these is the vertical system normally used in this program, and the other is a horizontal system of a type used for commercial preparation of epitaxial Si. As in the study described above, the films were formed from the thermal decomposition of SiH$_4$, with H$_2$ used as a carrier gas. Intentional doping to concentrations from 1 to 6 x 10^{16} cm^{-3} was achieved with the use of AsH$_3$ as the dopant gas. Growth temperatures ranged from 955C in the horizontal system to 1075C in the vertical system, and film thicknesses varied from 1.5 to 1.8μm.
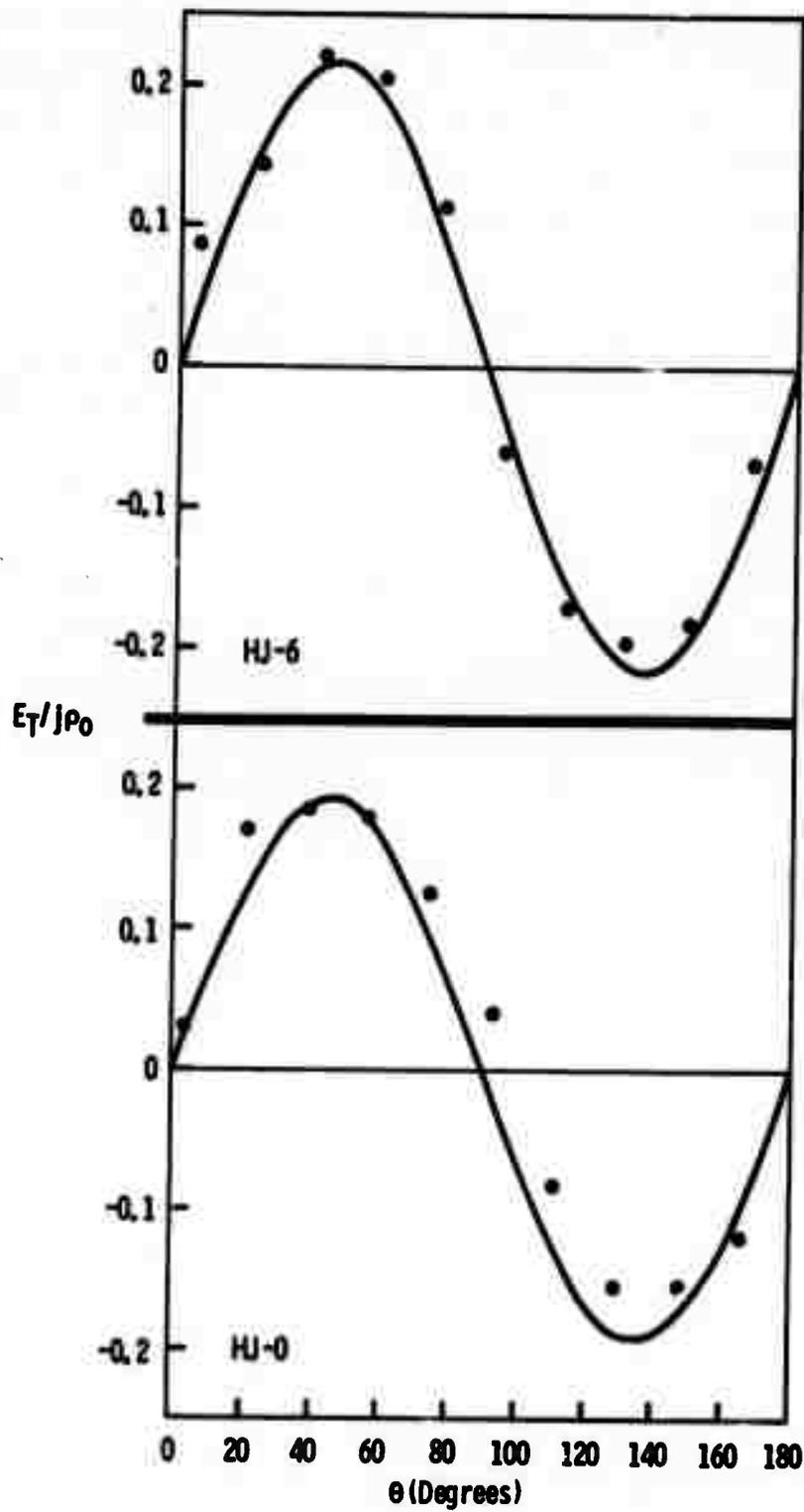
Figure 30. Transverse Electric Field Associated with Piezoresistance Effect and Thermally Induced Stress in $(221)Si/(11\bar{2}2)A\ell_2O_3$

66

Electrical data were taken on eight samples of $(001)Si/(01\bar{1}2)A\ell_2O_3$. For every sample, the orientation of each leg of the Hall pattern was determined with respect to the $<100>$ Si direction which is parallel to the $[2\bar{1}\bar{1}0]A\ell_2O_3$ direction in the plane of the substrate. The mobility in each leg could then be plotted vs the angle θ between the current direction and the $<100>$ Si axis. Typical mobility data are shown plotted in Figure 31 for two samples. The mobility can be seen to vary with angle and appears to approach a maximum at 0 deg.

As in the case of the (221)Si plane discussed above, theoretical treatment of piezoresistance predicts a mobility variation of the form $\mu/\mu_0 = (a+b\cos 2\theta)^{-1}$, consistent with the qualitative behavior observed. Accordingly, a least-squares fit of the data to the above equation is shown by the solid curve in the figure. The calculated maximum and minimum mobilities along with the anisotropy parameter A are tabulated in Table XIV.

It can be seen that the anisotropy varies between approximately 7 and 11 percent; the average value is 9.2 percent. Also shown is the RMS error (in percent) between the experimental points and theoretical curve for each sample.

Measurements were taken at 77K on several selected samples, and representative data for one sample are shown in Figure 32; the parameters deduced from the curve fitting procedure are also shown in Table XIV. The anisotropy is found to increase in going from room temperature to 77K by roughly a factor of three for those samples measured. This is consistent with the variation of the peizoresistance coefficients in Si with temperature.

The theoretical piezoresistance in the (001)Si plane is found to be

$$\frac{\Delta\rho}{\rho_0} = K + K' \left[\alpha_{A\ell_2O_3 \perp c} - \alpha_{A\ell_2O_3 //c} \right] \cos 2\theta,$$

where K and K' are constants. The anisotropy in this plane is thus proportional to the difference in thermal expansion coefficients of $A\ell_2O_3$ parallel and perpendicular to the c-axis. Such effects would therefore be expected to be absent for (001)Si on $MgA\ell_2O_4$. From the above equation it follows that, numerically,

$$\frac{\mu}{\mu_0} = (1.44192 - 0.04449 \cos 2\theta)^{-1}.$$

For each sample measured, μ_0 has been calculated from this equation, and these values are also given in Table XIV. Comparison with Table XIII shows that the values of μ_0 are very similar for both the (001) and (221)Si planes.

The theory also predicts a transverse electric field effect in the (001)Si plane, given by $E_T/j\rho_0 = 0.04449 \sin 2\theta$. Attempts have been made to measure this voltage; however, the small voltage involved makes the determination extremely difficult. Representative data on one sample are shown in Figure 33. A least-squares fit to the data gives a coefficient of ≈ 0.08, which is somewhat larger than predicted; however, the fit is not good. The value of μ_0 used in this expression is found from the value of μ_0 determined from the longitudinal mobility measurements described above. This transverse voltage also increases at 77K and is also shown in Figure 33. The magnitude of the increase is a factor of between 2 and 3, similar to that for the longitudinal effect. Note that the fit to theory is much better at 77K, due to the larger signal.
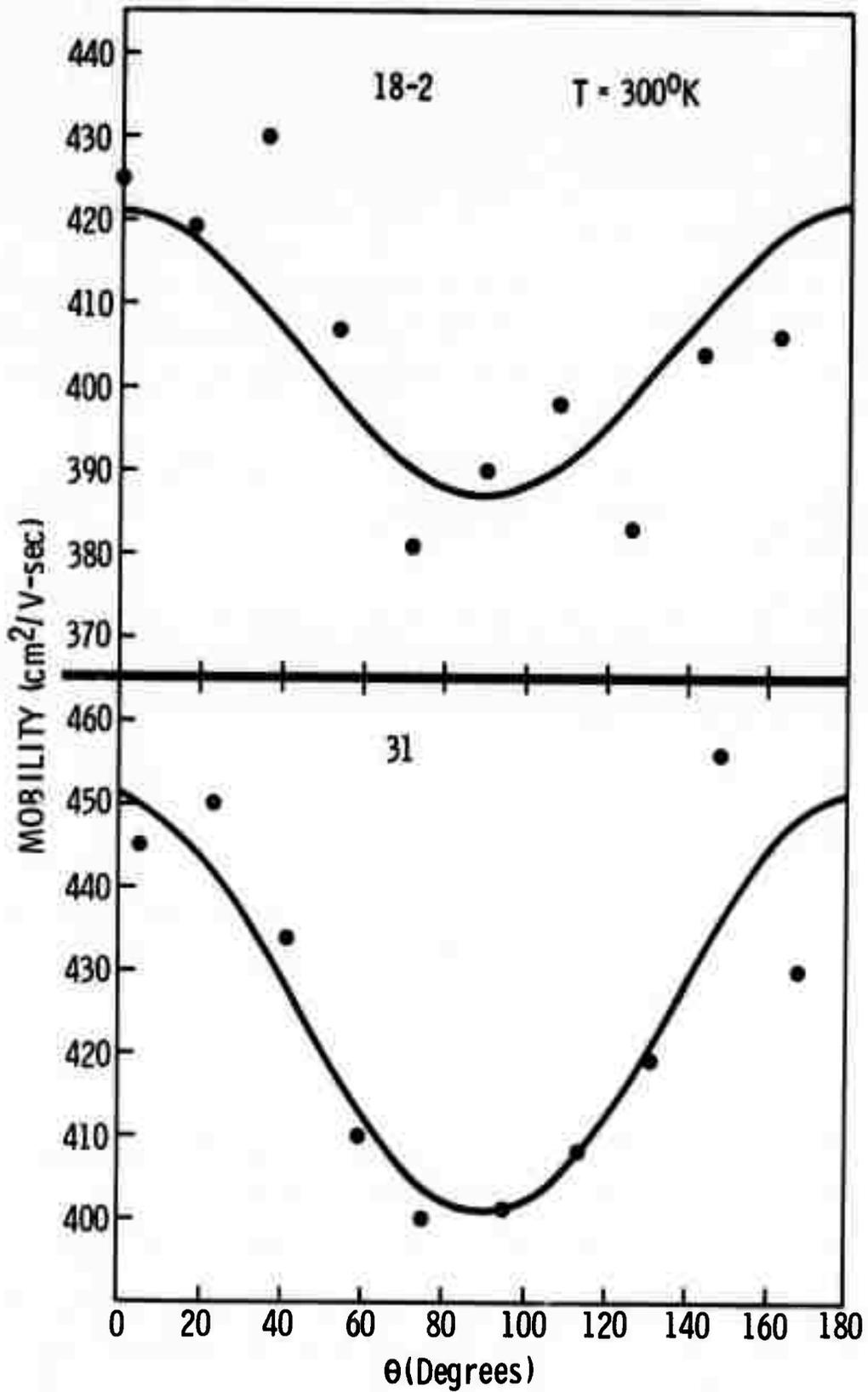
Figure 31. Variation of Hall Mobility with Direction in $(001)Si/(01\bar{1}2)A\ell_2O_3$

TABLE XIV
Anisotropy Data for $(001)Si/(01\bar{1}2)Al_2O_3$

Sample	μ_{max}	μ_{min}	μ_A	A (%)	RMS Error (%)	μ_0
Room Temperature Data						
102	446	408	427	6.7	1.6	615
18-1	432	397	415	8.6	1.4	598
15	472	425	449	10.5	2.5	648
3412-3	513	472	493	8.2	1.9	711
3411-1	516	478	497	7.6	2.1	717
18-2	422	387	405	8.6	2.5	584
31	451	401	426	11.6	2.2	614
13	443	394	419	11.7	2.9	604
(Average)	(462)	(420)	(441)	(9.2)		(636)
Liquid-N_2 Temperature Data						
18-1	1014	797	906	24	5.7	1305
31	1063	832	948	24	7.0	1367

69
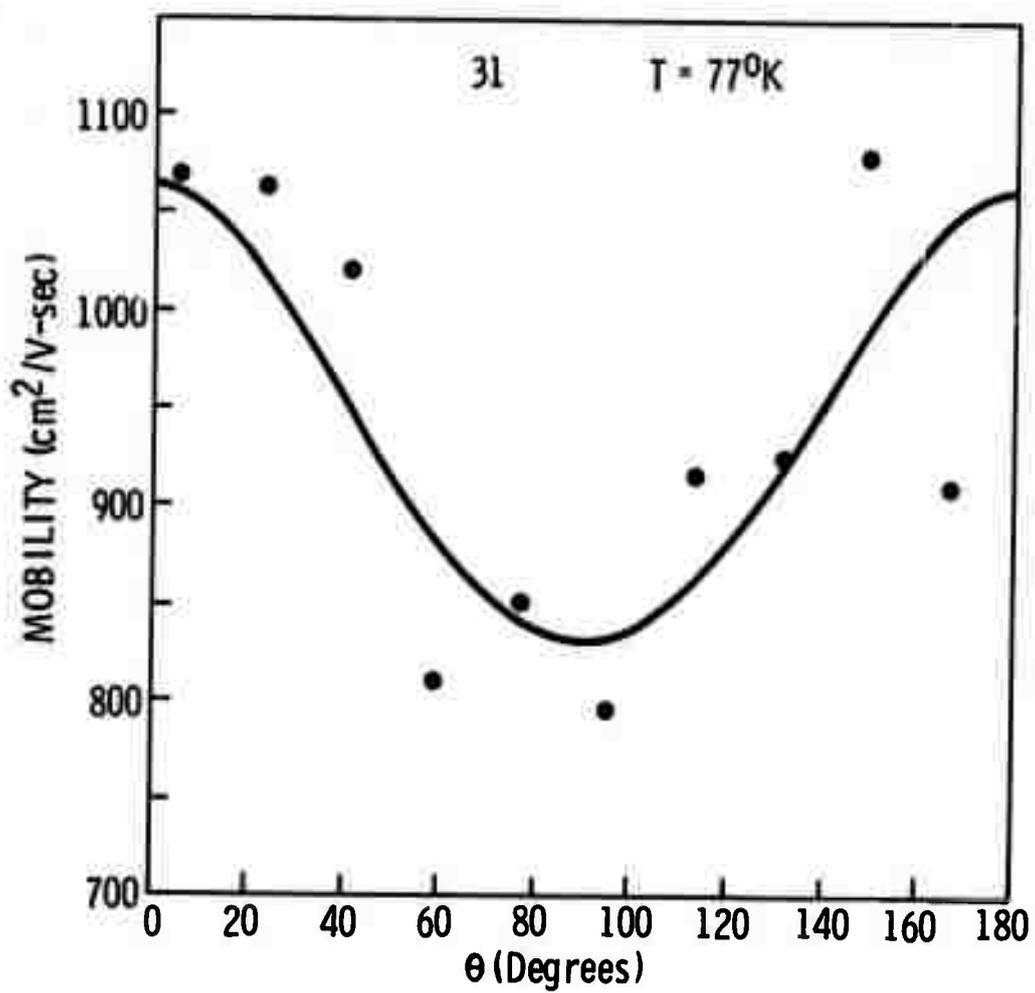
Figure 32. Variation in Hall Mobility with Direction at 77K in $(001)Si/(01\bar{1}2)A\ell_2O_3$
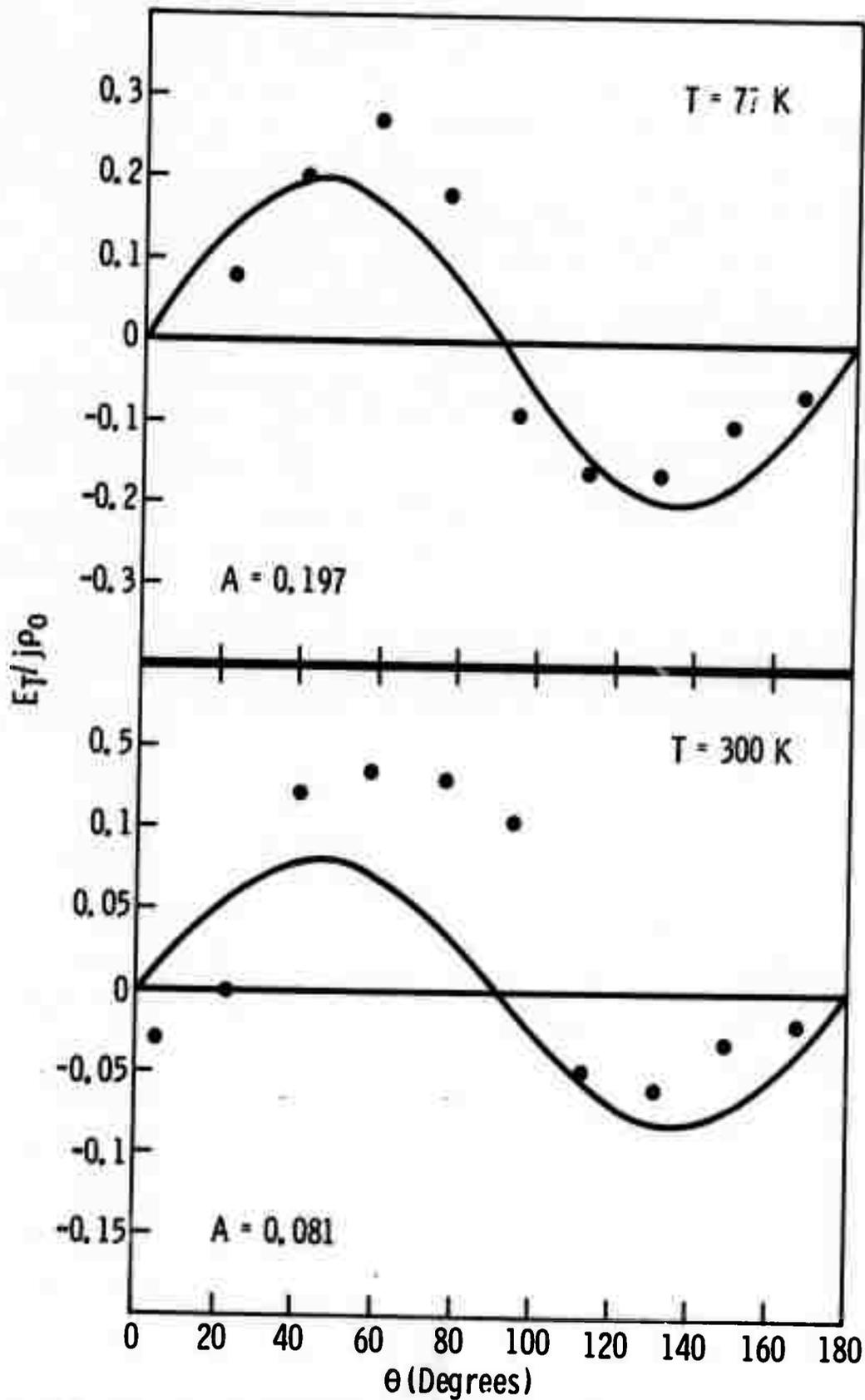
Figure 33. Transverse Electric Field Associated with Thermally Induced Stress and Piezoresistance Effect in $(001)Si/(01\bar{1}2)A\ell_2O_3$

c. Electrical Properties of Si Grown on $MgA\ell_2O_4$

Additional studies of the $Si/MgA\ell_2O_4$ system have recently been undertaken, with emphasis on the growth of $(111)Si/(111)MgA\ell_2O_4$ in a mixed H_2-He atmosphere (Subtask 2). Preliminary data indicate that good quality n-type films can be grown on $(111)MgA\ell_2O_4$ with carrier mobilities higher than those achieved in the $Si/A\ell_2O_3$ system. Mobilities as high as 925 cm^2/V-sec have been measured in ~2μm-thick films, which approaches bulk Si mobilities. The variation of electrical properties with growth conditions for these films is discussed in the following paragraphs.

Since growth temperature has been shown to be an important parameter in determining film quality, the electrical properties of a group of $(111)Si/MgA\ell_2O_4$ samples having net donor concentrations in the $10^{16}cm^{-3}$ range were examined as a function of growth temperature between 950 and 1050 C. Low growth rates (<1μm/min) were used for this study, in a mixed 0.8 percent H_2-He atmosphere. The data are shown in Table XV, and indicate that equivalent quality films can be grown over a wide temperature range. No optimum growth temperature is suggested by the data; however, the use of more desirable growth rates may lead to a more definitive answer to this question.

The variation in electron mobility with growth rate for a growth temperature of 1025 C is shown in Figure 34. Growth rates were controlled by changing SiH_4 flows and also by varying the concentration (see Subtask 2) from approximately 0.8 percent to 4 percent. It is apparent from this data that excellent quality Si can be grown at the higher growth rates (>2μm/min).

Additional mobility data are shown in Figure 35, which illustrates a limited amount of data at higher growth rates. This figure also demonstrates the effect of different tanks of SiH_4 on film quality; the open and solid circles are data obtained from samples grown with different sources of SiH_4. The purity of the SiH_4 was evaluated by growing a thick (~100 μm) film of Si on p-type Si substrates and measuring the film characteristics. The open circles were grown with a tank of SiH_4 which yielded films having the following characteristics: $\rho = 25$ ohm-cm, $n = 2 \times 10^{14}cm^{-3}$, and $\mu = 1300$ cm^2/V-sec. The closed circles were grown with SiH_4 which produced films with $\rho = 47$ ohm-cm, $n = 1.0 \times 10^{14}$ cm^{-3}, and $\mu = 1300$ cm^2/V-sec. The purity of the two tanks thus appears to be equivalent based on Si growth on Si, but the quality of Si films produced on $MgA\ell_2O_4$ is markedly different.

An $A\ell_2O_3$ substrate was included in several of the $Si/MgA\ell_2O_4$ growth runs in order to compare the quality of the resulting films. However, it should be kept in mind that (111)Si may tend to have a higher mobility since stress in the film produces a less deleterious effect on the mobility for (111)Si growth. This data is recorded in Table XVI for two growth temperatures. At 1025 C the growth on $(111)MgA\ell_2O_4$ was consistently superior to that on $(01\bar{1}2)A\ell_2O_3$; however, the lower mobilities on $A\ell_2O_3$ are consistent with those found previously in the H_2 system at 1025C. At 1050C, where the growth on $(01\bar{1}2)A\ell_2O_3$ improves in the H_2 system, the films are comparable in quality.

TABLE XV

Variation of Electrical Properties with Temperature
for (111)Si/(111)MgAℓ_2O$_4$ for Low Growth Rates

Growth Temperature (C)	Substrate*	Growth Rate (μm/min)	Thickness (μm)	Net Donor Carrier Concentration (cm^{-3})	Mobility (cm^2/V-sec)
950	LO	0.23	2.3	2.2×10^{17}	490
955	LO	0.67	2.0	2.0×10^{16}	510
	LO	0.44	2.2	1.4×10^{17}	550
	LOT	0.42	2.1	9.6×10^{16}	460
975	LO	0.33	2.3	7.3×10^{16}	640
	LOT	0.34	2.4	7.3×10^{16}	660
	LOT	0.33	2.3	7.0×10^{16}	520
	LOT	0.36	2.5	5.5×10^{16}	590
1000	LO	0.29	2.0	2.7×10^{16}	480
	LOT	0.31	2.2	1.4×10^{16}	390
1025	LO	0.23	1.6	3.4×10^{16}	560
	LOT	0.21	1.5	3.2×10^{16}	420
	LOT	0.23	1.6	2.9×10^{16}	300
	LO	0.33	2.3	5.7×10^{16}	660
	LOT	0.27	1.9	1.5×10^{16}	480
1050	LO	0.33	2.0	2.3×10^{16}	630

*LO: Substrate purchased from Union Carbide Corp.

 LOT: Substrate supplied by Crystal Technology, Inc., for evaluation; surface finish poor on these substrates.
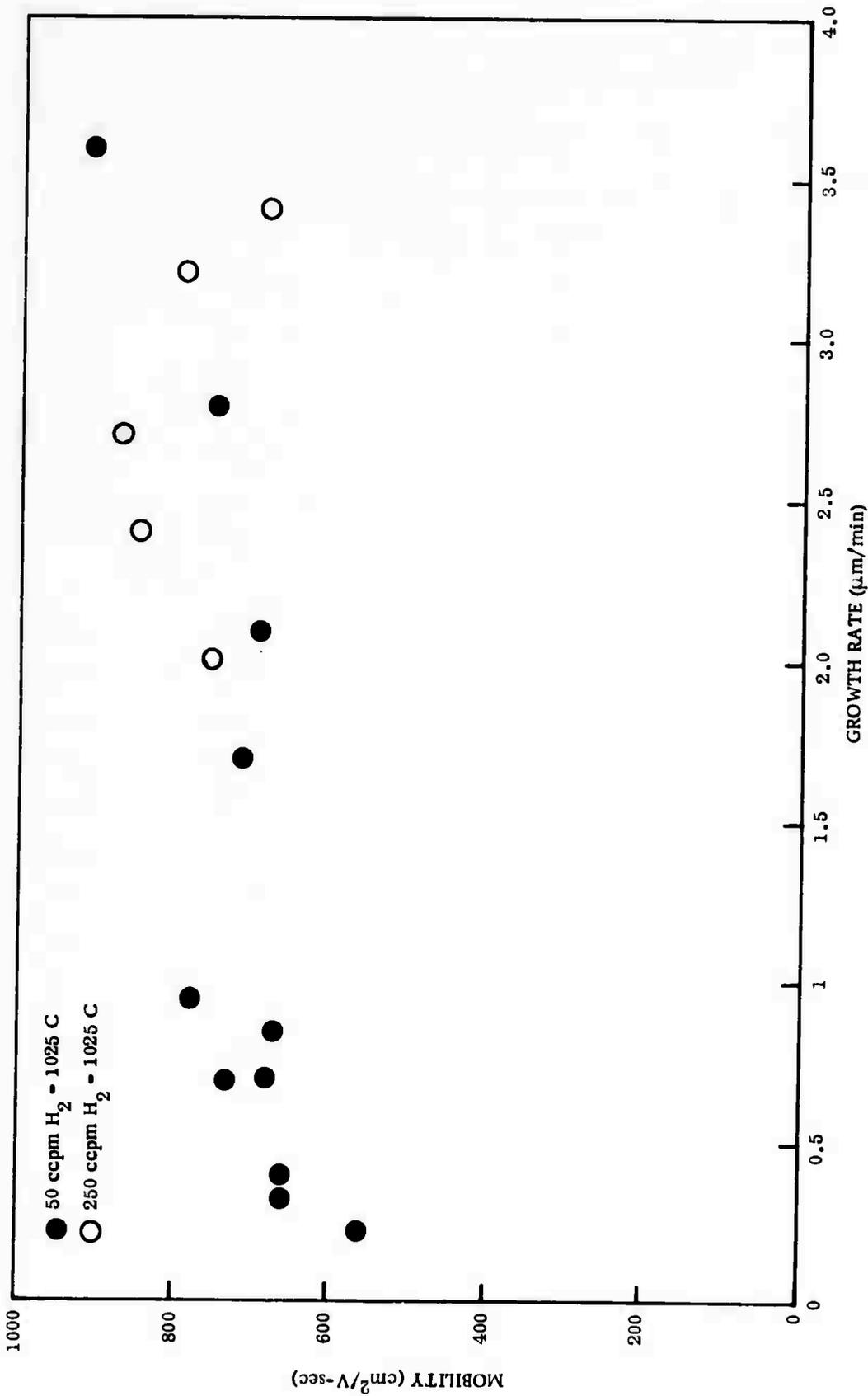
Figure 34. Variation in Hall Mobility with (Low) Growth Rate for (111)Si/(111)MgAℓ$_2$O$_4$ (Growth Temperature 1025 C)

74
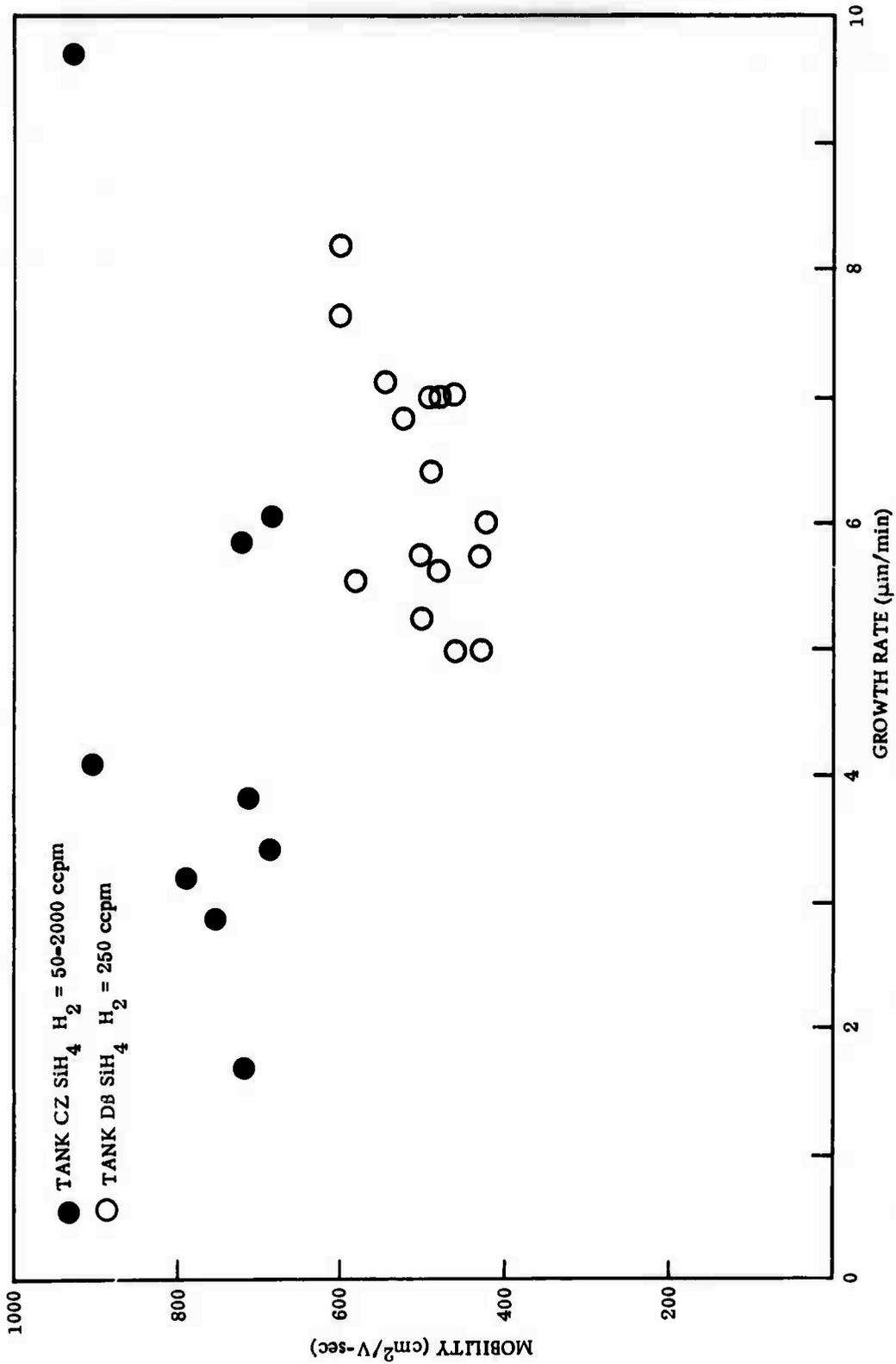
Figure 35. Variation in Hall Mobility with (High) Growth Rate for (111)Si/(111)MgAl_2O$_4$ (Growth Temperature 1025 C)

75

TABLE XVI
Comparison of Properties of Si/Aℓ_2O$_3$ and Si/MgAℓ_2O$_4$
Grown at Two Different Temperatures

Growth Temp (C)	Percent H$_2$ in He	Growth Rate (μm/min)	Thickness (μm)	Resistivity (ohm-cm)	Net Donor Carrier Concentration (cm^{-3})	Mobility (cm^2/V-sec)	Substrate
1025	0.8	0.40	1.95	0.20	7.6×10^{16}	410	(01$\bar{1}$2)Aℓ_2O$_3$
		0.41	1.93	0.25	3.8×10^{16}	660	(111)MgAℓ_2O$_4$
1025	4.2	2.2	1.6	1.2	1.3×10^{16}	411	(01$\bar{1}$2)Aℓ_2O$_3$
		2.4	1.8	0.77	1.1×10^{16}	744	(111)MgAℓ_2O$_4$
	4.2	2.9	2.2	0.10	1.4×10^{17}	440	(01$\bar{1}$2)Aℓ_2O$_3$
		3.1	2.3	0.11	9.4×10^{16}	598	(111)MgAℓ_2O$_4$
1050	0.8	0.27	1.60	0.35	2.7×10^{16}	650	(01$\bar{1}$2)Aℓ_2O$_3$
		0.33	1.96	0.43	2.3×10^{16}	630	(111)MgAℓ_2O$_4$

d. Electrical Properties of Si/Aℓ_2O$_3$

Additional experiments to evaluate further the parametric relationships among growth temperature, growth rate, and substrate orientation have been carried out for the Si/Aℓ_2O$_3$ system. For the experiments examining the effects of growth rate, the amount of dopant gas added to the gas stream was adjusted for each growth rate so that the carrier concentration in the film was nearly constant for the film orientation being grown.

The mobilities of ~2 μm-thick, n-type (100)Si/(01$\bar{1}$2)Aℓ_2O$_3$ films grown at various temperatures are plotted versus growth rate in Figure 36. The data show the increasing mobility with increasing growth rate observed previously (Third Semiannual Report, Ref 3), although the maximum mobility values are not as high as previously reported. The explanation for these smaller values is not known, but may relate to the successive reuse of the substrates employed for these studies. As seen from Figure 36, there appear to be no significant differences for growth in the range 1050 to 1100 C.

The effects of growth rate for (100)Si at higher and lower temperatures are recorded in Table XVII. These data do not suggest appreciable differences in mobility for the various growth rates. The generally lower values of mobility with respect to those shown in Figure 36, however, indicate that the growth temperature is out of the optimum range for growth of (100)Si. The fact that thinner samples were grown at 1125 C, however, also leads to lower mobilities in those instances.

The effect of growth rate for (111)Si is shown in Table XVIII. As in the case of (100)Si, the higher growth rates lead to improved films. The high mobilities obtained in these films with thicknesses less than 2 μm are evidence of the desirability of high
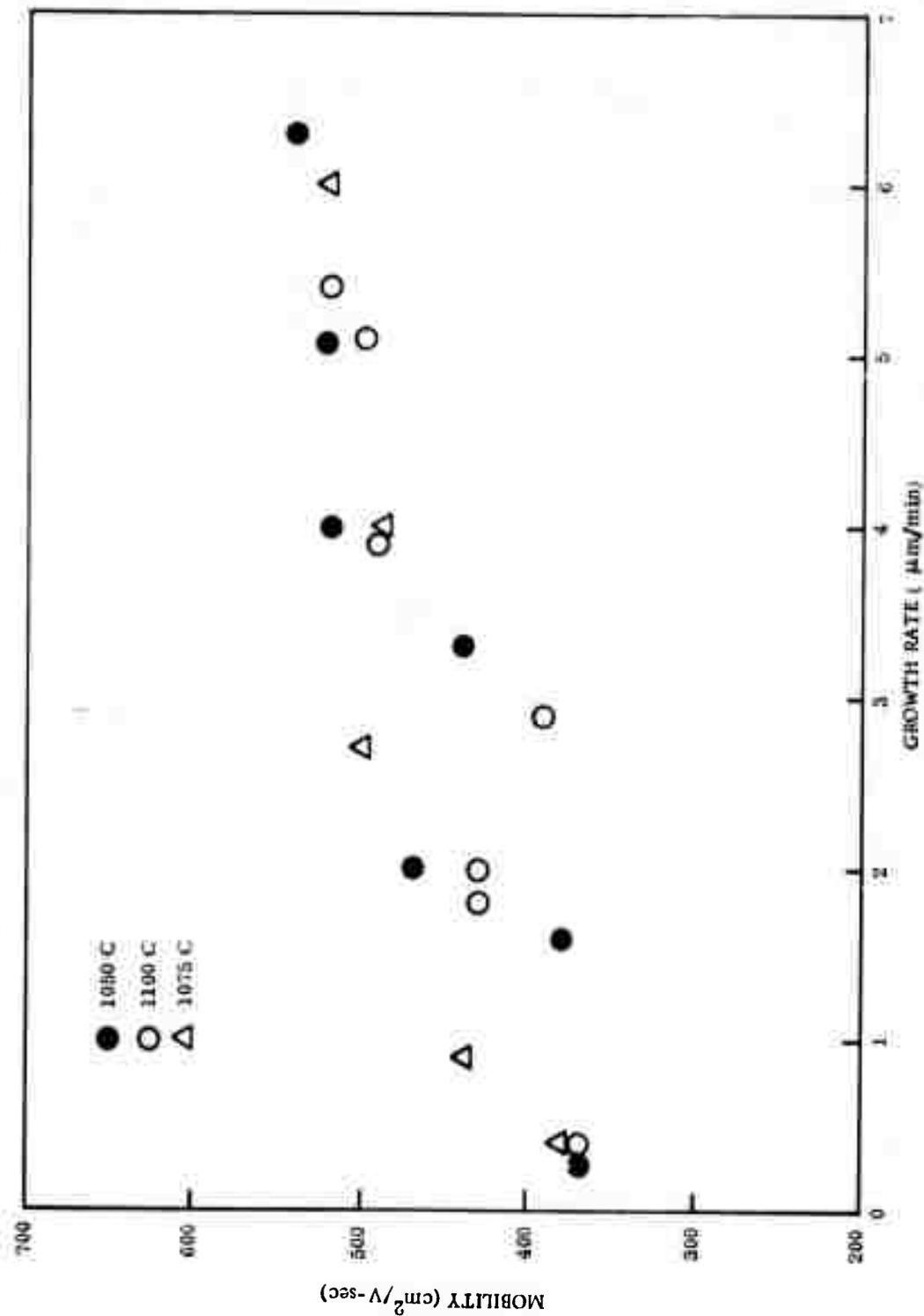
Figure 36. Hall Mobilities of (100)Si/(01$\bar{1}$2)Al$_2$O$_3$ as Function of Growth Rate (Grown at Three Different Temperatures)

77

growth temperatures for (111)Si growth. Although the amount of $A\ell$ autodoping from the substrate is severe at this growth temperature (Ref 3), the $A\ell$ does not appear to affect severely the mobility in annealed n-type films.

TABLE XVII
Effect of Growth Rate on the Electrical Properties of
$(100)Si/(01\bar{1}2)A\ell_2O_3$ Films Grown at 1025 and 1125 C

Growth Temp (°C)	Growth Rate (μm/min)	Film Thickness (μm)	Resistivity (ohm-cm)	Carrier Concentration (cm^{-3})	Mobility (cm^2/V-sec)
1025	0.36	1.8	0.12	1.5×10^{17}	360
1025	1.7	1.7	0.36	3.4×10^{16}	450
1025	1.8	1.8	0.19	7.9×10^{16}	420
1025	2.8	1.9	0.18	8.6×10^{16}	400
1025	3.9	2.0	0.19	7.2×10^{16}	460
1025	4.9	2.0	0.20	7.7×10^{16}	400
1025	5.6	1.9	0.25	5.9×10^{16}	420
1125	0.27	1.4	0.33	4.7×10^{16}	400
1125	1.5	1.5	1.6	9.5×10^{15}	400
1125	1.9	1.3	1.5	1.0×10^{16}	410
1125	2.3	1.2	0.82	1.9×10^{16}	400
1125	2.9	1.3	1.6	9.4×10^{15}	420

TABLE XVIII
Effect of Growth Rate on the Electrical Properties of
$(111)Si/A\ell_2O_3$ Films Grown at 1125 C

Growth Rate (μm/min)	Thickness (μm)	Resistivity (ohm-cm)	Carrier Concentration (cm-3)	Mobility (cm^2/V-sec)
0.20	1.0	0.21	5.3×10^{16}	560
0.31	1.6	0.60	2.3×10^{16}	450
1.7	1.7	1.0	1.1×10^{16}	560
1.7	1.7	0.90	1.2×10^{16}	600
2.2	1.5	1.1	9.7×10^{15}	610
3.8	1.3	0.34	2.5×10^{16}	730
4.5	1.5	0.75	1.2×10^{16}	690

e. Measurement of Photoelectric Effects in Heteroepitaxial Films on Al_2O_3 Substrates

The experiments on photoinjection of electrons from metal films into Al_2O_3 substrates have been continued at UCLA during this reporting period. Further experiments were carried out to ensure that the current observed in the photoelectric experiments (Ref 3) is indeed due to photoinjection of electrons from the metal films into the insulator.

In one such experiment, six Al film stripes, each ~300Å thick and 1 mm wide, were depostited on one side of the substrate, with a spacing of approximately 1 mm between adjacent stripes (Figure 37). A Au film was deposited uniformly on the other side of the substrate. A sharply focussed light beam was scanned at a slow rate across the face of the substrate having the semitransparent Al stripes, and the photoelectic current was recorded by an X-Y recorder as a function of the position of the light beam.

Six peaks, with well-defined minima between, were observed in the photoelectric current for both polarities of the bias voltage, as shown in Figures 38 and 39. The peaks correspond to incidence of light on a stripe and the minima correspond to incidence of light in the spaces between stripes. Observation of the six peaks even when the Al films were biased positive clearly demonstrates that (1) electrons were injected into Al_2O_3 from the Au film, and (2) such injection occurs only in those regions of Al_2O_3 where an electric field exists, viz., the regions under the Al stripes.
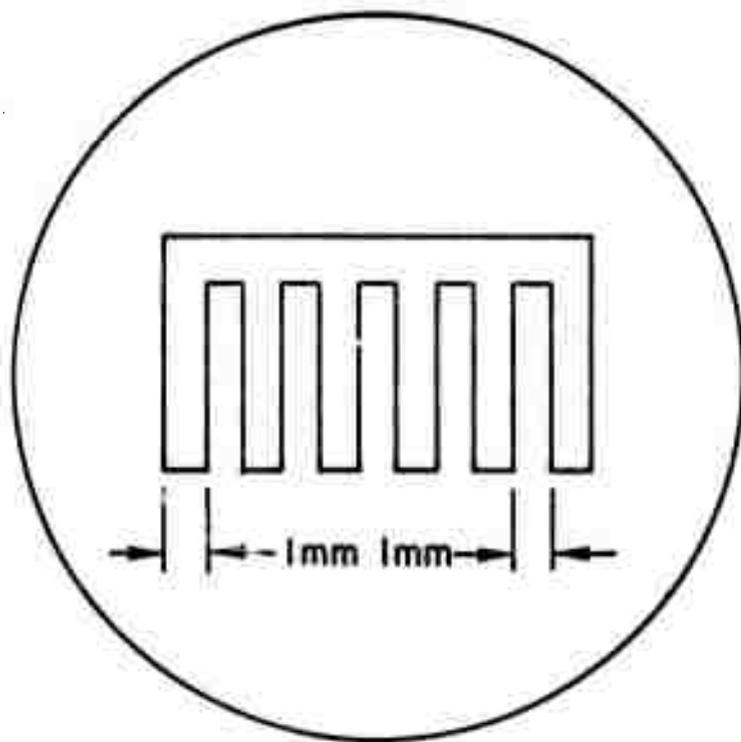
Figure 37. Configuration of Semitransparent Al Stripes Deposited on Al_2O_3 Substrate

79
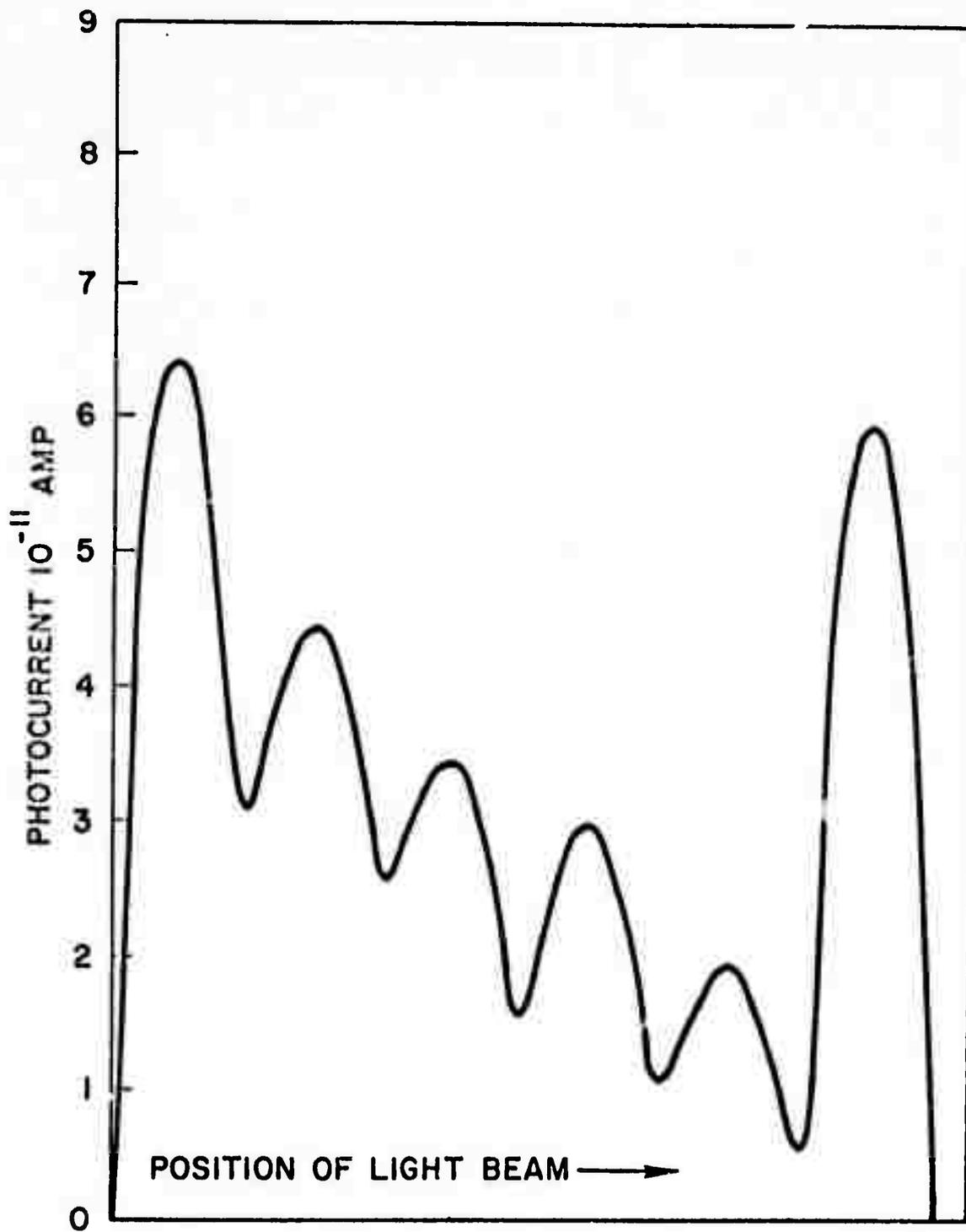
Figure 38. Photocurrent as Function of Position of Scanning Light Beam, with Aℓ Biased Negative

80
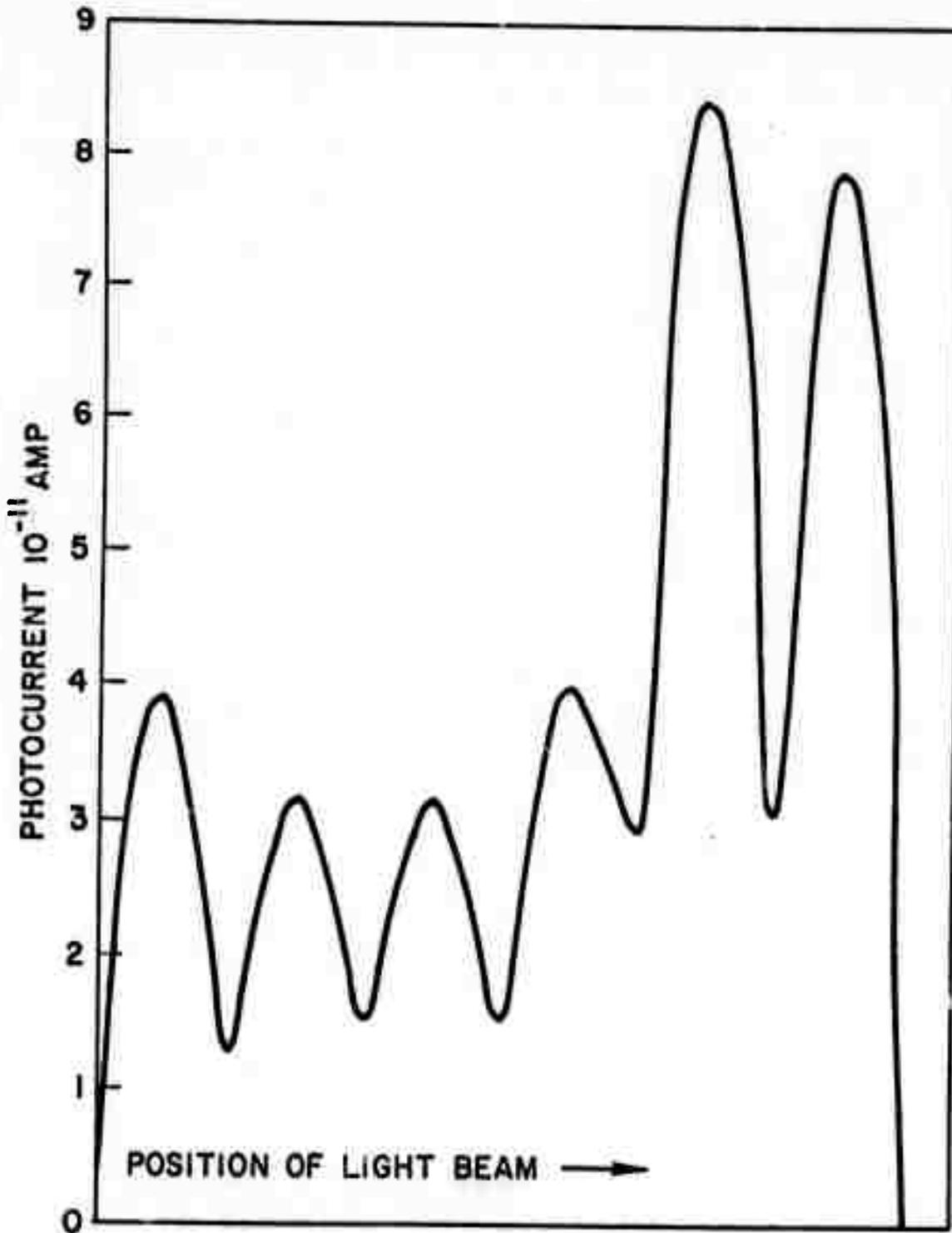
Figure 39. Photocurrent as Function of Position of Light Beam,
with A*l* Biased Positive

For a given bias voltage, as soon as the light beam was directed onto the metal electrode, the photocurrent reached a peak value in a time interval the order of a few milliseconds and then decayed as a function of time, reaching a steady-state value after several minutes, thereby indicating that traps were being filled. The higher the bias voltage, the larger was the number of traps that were filled.

For the case of electron emission from the $A\ell$ electrode to the $A\ell_2O_3$, the steady-state current values were measured for various photon energies with the bias voltage kept constant. The square root of the photoelectric current was then plotted as a function of the photon energy to obtain a Fowler plot, as shown in Figure 40. Two linear regions corresponding to two threshold energy values of 3.15 and 4.3 eV, respectively, were observed. Taking the lower value as that corresponding to the height of the interface barrier between $A\ell$ and $A\ell_2O_3$, the energy-band diagram shown in Figure 41 was constructed. The work function of $A\ell$ was taken to be 4.1 eV (Ref 15), and this gives a value of 1.0 eV for the electron affinity of $A\ell_2O_3$, which agrees well with the value quoted by Pong (Ref 16) for amorphous $A\ell_2O_3$. The value of 3.15 eV for the interface barrier height agrees well with the value 3.05 eV measured by Szydlo and Poirier (Ref 17) for the polycrystalline $A\ell_2O_3$-$A\ell$ interface.

When the photoelectric current corresponding to emission of electrons from other metals, such as Au, Ag, and Cu, was measured as a function of photon energy, the resulting Fowler plots were again characterized by two linear regions. The lower threshold energy values, again taken as the interface barrier heights, when combined with the value of 1.0 eV for the electron affinity of $A\ell_2O_3$ gave work function values (Ref 18) agreeing with previously published values for the metals involved.

In all these cases, the threshold energy value corresponding to the second linear region was 1 to 1.1 eV higher than the interface barrier height. This suggests the possibility that the higher threshold energy might correspond to vacuum emission of electrons from the metal into pinholes in the metal film. Further experiment is needed to verify this.

The fact that a photoelectric current is observed in $A\ell_2O_3$ layers several mils thick clearly establishes that the range of photoinjected electrons is much larger than the value of 130 Å reported for amorphous $A\ell_2O_3$ layers (Ref 16). It is possible to measure the range of the injected electrons by carrying out measurements with $A\ell_2O_3$ substrates of several different thicknesses.

The magnitude of the current as a function of the thickness of $A\ell$ films deposited on the same $A\ell_2O_3$ substrate was also measured, with the light incident on the $A\ell$ films. A peak was observed around 2500 Å thickness, and the current was found to be an appreciable fraction of the peak even when the thickness of the $A\ell$ layer was as large as 5000 Å. This result is in contrast to the mean range for electrons in $A\ell$ as measured by other workers (Ref 19).

Using this technique, it is possible to measure the transport properties of electrons injected into ordered insulators and to determine the range of electrons in metal films. All the measurements described above were conducted at room temperature; it is planned that similar experiments be carried out at various other temperatures.
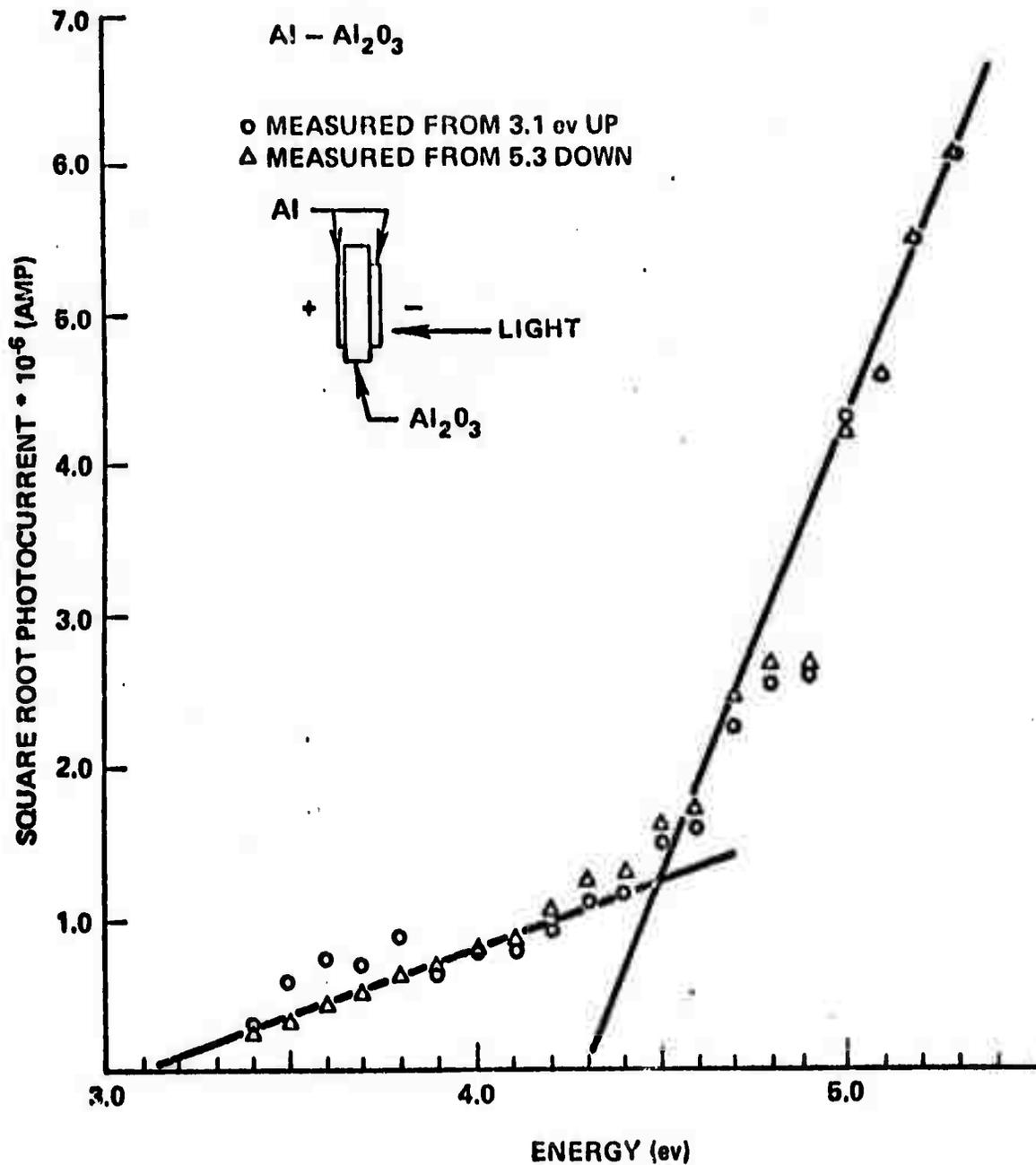
Figure 40. Fowler Plot of Photocurrent as Function of Photon Energy
for Al-Al₂O₃ Interface

83
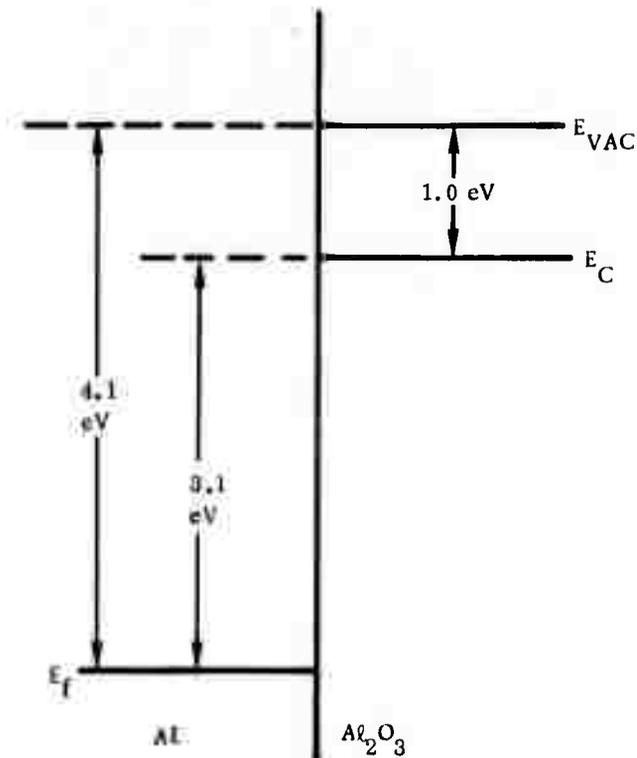
Figure 41. Energy-Band Diagram for Aℓ-Aℓ$_2$O$_3$ Interface

The effect of annealing on the photoinjection properties of metal films was also investigated. A metal-insulator-metal sandwich consisting of semitransparent Au films (300 to 400 Å thick) deposited on the two opposite faces of an (01$\bar{1}$2) Aℓ$_2$O$_3$ substrate 0.016 in. thick was fabricated. Photoelectric measurements were made on this sample under four different experimental conditions, corresponding to opposite polarities of bias voltage first with light incident on one metal film and then with light incident on the other metal film. The samples were then annealed for 30 min at 500C in vacuum, after which the photoelectric measurements were repeated.

It was found that the photoelectric characteristics had changed considerably as a result of the annealing. For example, the plot of the square root of the photo-current as a function of photon energy appeared much smoother (i.e., devoid of fine structure) after annealing, for electron injection from the illuminated film.

Some experiments were carried out in an attempt to determine the mobility of injected electrons in the insulator by using a pulsed N$_2$ gas laser for transient internal photoemission studies. Due to a high noise pick-up in the measuring circuit from the switching circuit of the laser the signal could not be observed. The experiments have not yet been repeated.

f. Measurement of High-Field Transport Properties of Heteroepitaxial Films

Experiments to determine the high-field transport properties of heteroepitaxial semiconductor films on insulating substrates have been continued at UCLA during this reporting period. The experimental arrangement was shown in Figure 27 of the Third Semiannual Report (Ref 3). Measurements made in the first half of the second year had not yet revealed the presence of high-field effects.

Considerable difficulty was experienced initially in fabricating the device structures required for these measurements. However, a few test devices were successfully made and were tested. It was found that the metal pads deposited on the semiconductor films did not provide a good ohmic contact. Finally, after considerable additional experimentation, good ohmic contacts were obtained on GaAs films by evaporating an alloy of Ag, In and Ge (90 percent - 5 percent - 5 percent) onto the GaAs film and heating the sample for two minutes at 700C in He gas ambient.

Some results of the high-field transport measurements are given in Figure 42. It can be seen that the current deviates from linear behavior for electric fields beyond ~1.4 kV/cm and exhibits a peak around 3 kV/cm. However, because of heating effects (a low-resistivity sample was used), the current tends to increase again at fields higher than 3.4 kV/cm. In addition, significant sparking was observed at field strengths of 6 to 8 kV/cm.
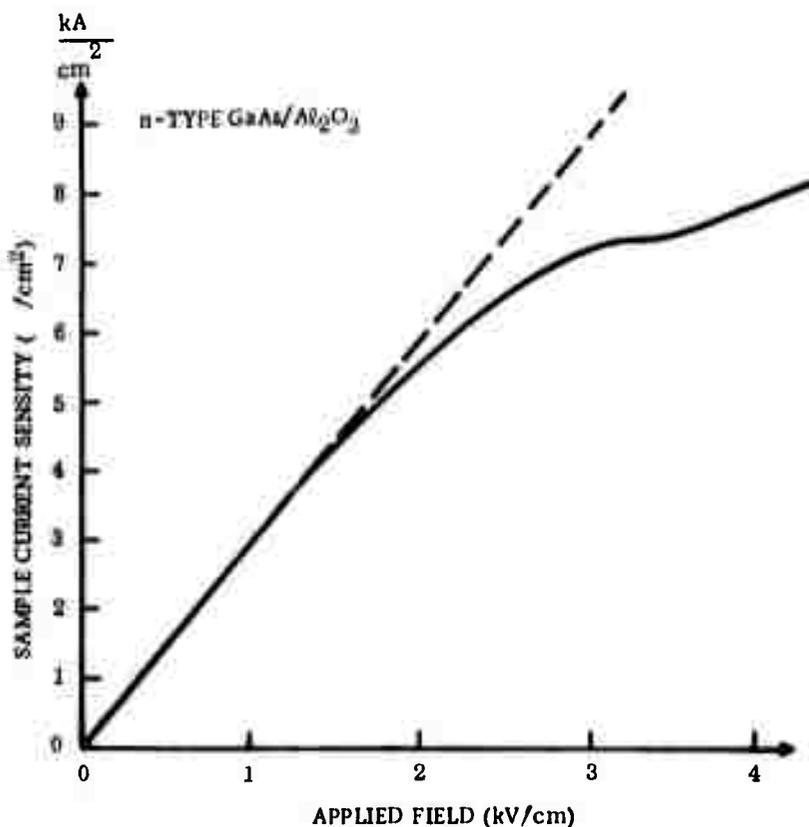
Figure 42. High-Field Transport Effects in Heteroepitaxial GaAs/Aℓ_2O$_3$

85

In the case of Si films on $A\ell_2O_3$, electrodes of Au doped with 1 percent Sb were deposited on the Si films and heated to 700C for two minutes in a N_2 ambient. Ohmic contacts were still not obtained, however, and this prevented the observation of high-field characteristics. Further experimentation is progressing directed toward achieving good ohmic contact. It was noted that the nonohmic contacts did become ohmic after a few occurrences of the sparking referred to above. If necessary, such a "forming" process will be systematically employed for preparing the required ohmic contacts.

7. SUBTASK 7. DESIGN AND FABRICATION OF DEVICES

During the first year apparatus for determining carrier lifetime by C-V measurement in MOS structures was designed, constructed and tested. A special MOS structure was designed for measurement of channel conductance, high- and low-field transport properties, and various interface characteristics of heteroepitaxial films. Initial attempts to fabricate Schottky-barrier diodes in $Si/A\ell_2O_3$ films as a means of evaluating their electrical properties were not successful.

In the first six months of the second year preliminary design of a Schottky-barrier type of FET was completed for use in making experimental FET structures in GaAs/, insulator films for operation at 1 GHz. Preliminary results on carrier lifetime in $Si/A\ell_2O_3$ films were obtained, after initial development of the measurement technique on bulk single-crystal Si samples was completed and after impurity contamination problems encountered in the oxide growth process were solved.

The main device-oriented effort has centered about the carrier lifetime studies using the MOS pulsed-capacitance technique and the attempts to fabricate a Schottky-barrier FET in $GaAs/A\ell_2O_3$. Both activities are being carried out at UCLA.

The GaAs FET work was hampered seriously earlier in this reporting period by difficulties encountered in processing the heteroepitaxial samples through the photolithography steps using the new device masks, fabrication of which was completed shortly after preparation of the Third Semiannual Report. It is believed that these processing problems are now successfully resolved, after several sessions in which the procedures being used at UCLA were critically reviewed and empirically modified by NR personnel in NR laboratories. The device fabrication work has been resumed, although some further delay is being encountered while heteroepitaxial samples are being prepared at NR as part of the Subtask 2 effort.

Lifetime studies using the technique of pulsed MOS capacitance have been continued during this report period. Many of the $Si/A\ell_2O_3$ samples received earlier were found to have a large number of pinholes, and this gave rise to device fabrication difficulties. The samples prepared more recently did not have many pinholes, containing typically about 20 pinholes of diameter larger than ~1 μm on each wafer. The number of pinholes was found to be larger in the (111) Si orientation than in the (100) orientation. The lower-resistivity samples had fewer pinholes and the number of pinholes seemed to progressively decrease as the thickness of the Si film was increased — not a surprising effect.

86

In the oxidation process used for making the MOS structure, the impurity distribution is changed in the bulk of the semiconductor in the region near the oxide interface. An analysis was made to consider the effect of impurity redistribution on the interpretation of lifetime measurement data using the pulsed MOS capacitance technique, and this is described in subsequent paragraphs.

The use of the pulsed MOS capacitance technique to determine the bulk generation lifetime τ_g and the surface recombination velocity s of both films and wafers of Si as well as GaAs has been reported by several authors (Refs 20 and 21). In this technique the capacitance C of the MOS structure is monitored as a function of time after the application of a depleting voltage step. Zerbst (Ref 20) has shown that for an ideal MOS structure having an oxide thickness x_0, corresponding to an oxide capacitance C_0, a plot of $-\dfrac{d}{dt}\left(\dfrac{C_0}{C}\right)^2$ vs $\left(\dfrac{C_F}{C} - 1\right)$ yields a straight line whose slope is related to τ_g and whose intercept on the $-\dfrac{d}{dt}\left(\dfrac{C_0}{C}\right)^2$ axis is related to s (Ref 3). C_F is the MOS capacitance at time $t = \infty$.

This technique has been suggested for in-process measurement of τ_g and s during device fabrication, and has recently been extended (Ref 22) for the case of Schottky-barrier diodes to determine the lifetime, energy level, and density of both deep and shallow impurity levels. In a study of the impurity redistribution in Si near the SiO_2-Si interface that occurs during thermal oxidation, Deal et al (Ref 23) used an "effective" surface doping concentration in examining the C-V characteristic of an MOS capacitor. However, this approach is unsuitable in pulsed measurements to determine lifetime since the depletion layer width W, and hence capacitance, changes with time t.

It is possible to illustrate quantitatively the effect of impurity redistribution on the interpretation of bulk generation lifetime using the pulsed MOS capacitance technique, and this is done as follows.

Grove et al (Refs 23 and 24) have shown that if a wafer of Si, initially uniformly doped with boron to a concentration N_B, is subjected to a thermal oxidation process, the resulting concentration N_S of boron in the Si at the SiO_2-Si interface will be lower than the bulk value by a factor typically from 2 to 7, depending on oxidation conditions. For a phosphorus-doped Si wafer N_S will be larger than N_B by a factor of from 1.1 to 4.

An exponential doping profile of the form

$$N(x) = N_B + (N_S - N_B)\, e^{-x/x_1} \tag{4}$$

was compared with the exact solution of Grove et al and was found to be in very close agreement (± 5 percent). The parameter x_1 is used to fit the exponential doping profile to the exact profile at Grove et al (Ref 24) and is plotted in Figure 43 against $\dfrac{N_S}{N_B}$ for both boron and phosphorus under various oxidation conditions. Using the exponential doping profile in a double integration of Poisson's equation, an expression for the voltage across the space charge region is obtained.
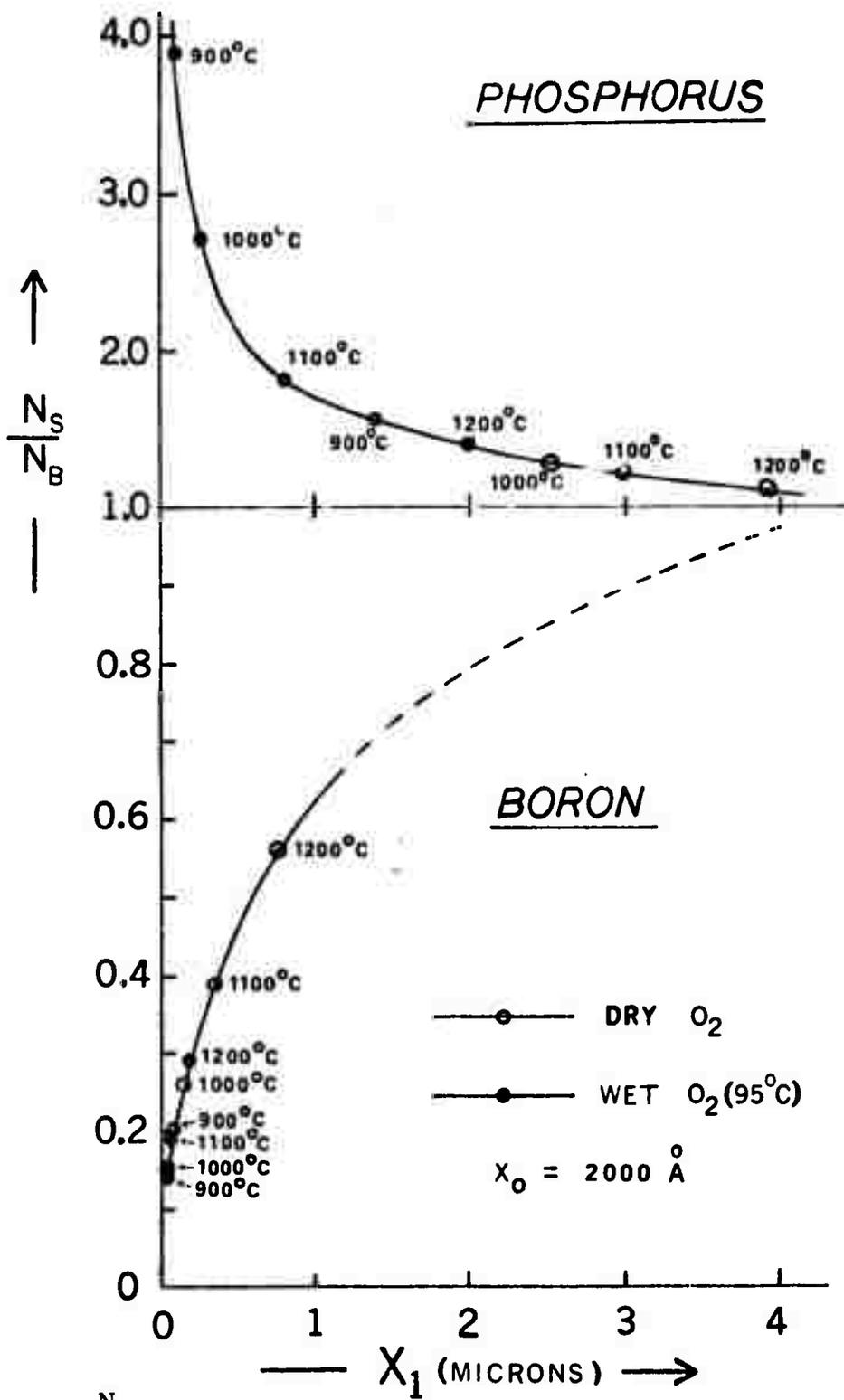
Figure 43. $\dfrac{N_s}{N_B}$ vs x_1 (in μm) for Phosphorus- and Boron-Doped Si Under Various Oxidation Conditions. (Compiled with the aid of data from Ref 24.)

Following the analysis of Zerbst (Ref 20) it can be shown that the rate of increase of charge Q_s at the SiO_2-Si interface is related to the MOS capacitance $C(t)$ by

$$\frac{dQ_s}{dt} = \frac{-qN_B \, \epsilon_s}{2C_o} \frac{d}{dt} \left(\frac{C_o}{C}\right)^2 - \frac{q(N_s - N_B) \, \epsilon_s \, e^{-\frac{W}{x_1}}}{2C_o} \frac{d}{dt} \left(\frac{C_o}{C}\right)^2 , \qquad (5)$$

where ϵ_s is the permittivity of the Si and q is the electronic charge. It has been assumed that the area A of the metal gate electrode is large enough to neglect surface effects and that the total capacitance may be represented by C_o in series with the depletion layer capacitance $C_d = \frac{\epsilon_s A}{W}$. The first term on the right-hand side of Eq 5 is the result due to Zerbst assuming a uniformly-doped sample, and the second term is the modification due to the exponential doping profile.

Setting Eq 5 equal to the bulk and surface generation current terms gives

$$-\left[\frac{N_B \, \epsilon_s}{2C_o} \frac{d}{dt}\left(\frac{C_o}{C}\right)\right]^2 B(C) = \eta_i s + \frac{\eta_i \, \epsilon_s}{\tau_g \, C_F}\left[\frac{C_F}{C} - 1\right] , \qquad (6)$$

where η_i is the intrinsic carrier concentration in the semiconductor and the function $B(C)$ is given by

$$B(C) = \left[1 + \left(\frac{N_s}{N_b} - 1\right) \exp\left(\frac{C_1}{C_o} - \frac{C_1}{C}\right)\right] = \left[1 + \left(\frac{N_s}{N_b} - 1\right) \exp\left(-\frac{W}{x_1}\right)\right] , \qquad (7)$$

where $C_1 = \frac{\epsilon_s A}{x_1}$.

A plot of the left side of Eq 6 as ordinate versus $\left(\frac{C_F}{C} - 1\right)$ yields a straight line whose slope is related to τ_g and whose intercept on the vertical axis is related to s. A Zerbst plot assuming uniform doping yields a lifetime value $\tau_g' \neq \tau_g$, due to the function $B(C)$. If $W \leq x_1$ then the entire space-charge region is located within a region of impurity redistribution, and $B(C)$ departs from unity.

Figure 44 shows the variation of $B(C)$ during the capacitance transient for various oxidation conditions. From Eq 6 and 7, and Figures 43 and 44 it can be seen that for boron the function $B(C) < 1$ and $\tau_g > \tau_g'$. For phosphorous the function $B(C) > 1$ and $\tau_g < \tau_g'$.
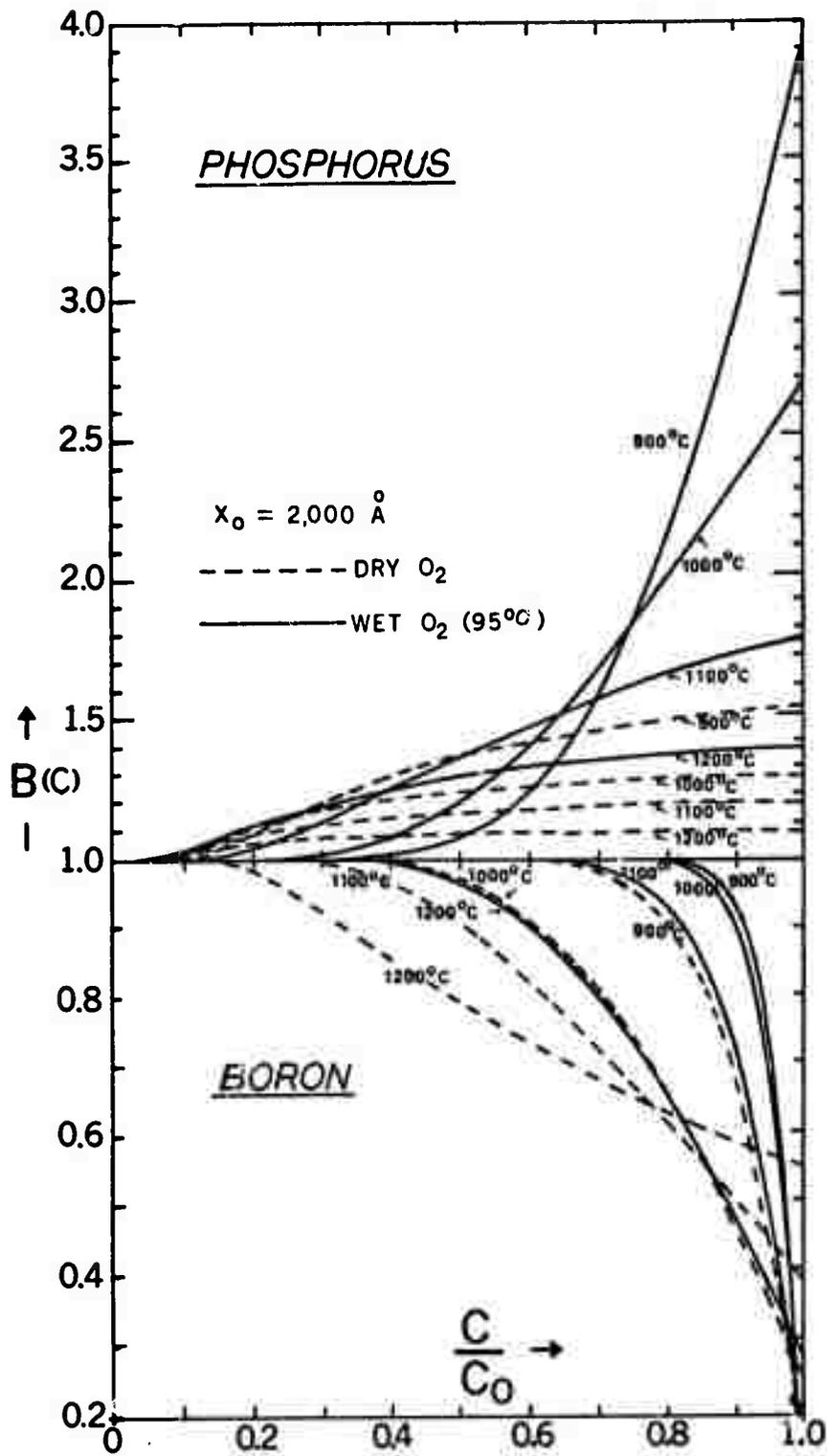
Figure 44. Impurity Redistribution Function B(C) vs Normalized MOS Capacitance C/C$_o$ for Phosphorus- and Boron-Doped Si under Various Oxidation Conditions

For $W >> x_1$ then $B(C) \simeq 1.0$ and $\tau_g' \simeq \tau_g$ for the entire transient response.

The exponential doping profile used in this analysis illustrates the effect of impurity redistribution on the interpretation of lifetime measurements from pulsed MOS capacitance experiments. Further high temperature processing such as annealing, gettering, or a second oxidation step may cause departures in the impurity redistribution profile, thereby leading to apparent changes in lifetime unless the actual doping profile is used in the analysis.

However, the actual doping profile may be obtained from the C-V characteristic (Ref 25). As a computer calculation is usually used to extract the doping profile from the C-V characteristic, it is convenient simply to incorporate this measured doping profile into the computer program analyzing the capacitance-time response, thereby obtaining more precise measurements of τ_g and s. Alternatively, thermal oxide growth conditions may be chosen from Figures 43 and 44 that result in negligible impurity redistribution, thereby allowing the simpler uniform doping approximation to be used in the waveform analysis.

The lifetime measurements on both Si and GaAs films on substrates primarily of Al_2O_3 are continuing. Detailed results as functions of film thickness, carrier concentration, and crystallographic orientation are being obtained and will be described in the next semiannual report.

SECTION III

WORK PLANNED FOR NEXT SIX MONTHS

The planned effort during the next six months in the seven subtasks will include the following. Deviations from these activities will be introduced when and as the progress of the total program requires it.

1. SUBTASK 1. THEORY OF EPITAXY AND HETEROEPITAXIAL INTERFACES

The investigation of surface reconstruction of the Al_2O_3 lattice using the previously determined potentials will be continued and completed. An existing Morse potential for Si will be investigated for suitability in the heteroepitaxial problem, and the adatom potential interaction between Si and the Al_2O_3 will be parameterized. Computer simulation of the growth of Si on Al_2O_3 using previously determined potentials, surface reconstruction, and parameterized adatom interactions will then be initiated; it is intended that the simulation work will begin late in the coming six-month period, although it may be delayed until early in the final six months of the program.

The extensive theoretical study of the anisotropy in mobility due to differential thermal contraction at the interface between film and substrate will be completed and a detailed paper will be prepared and submitted for publication. Further work in this area may be performed as required to complement and further advance the experimental studies of film mobility and other electrical properties.

2. SUBTASK 2. DEPOSITION STUDIES AND FILM PREPARATION

Because of the very encouraging electrical results obtained to date for Si grown on $MgAl_2O_4$ substrates in H_2-He mixtures this system will be explored further, not only for $MgAl_2O_4$ but also for Al_2O_3. This study will encompass various substrate orientations, and conditions will be established for optimized growth to permit identification of the preferred substrate. Further investigation of the autodoping phenomenon as a function of growth atmosphere (H_2-He ratio), temperature, substrate orientation, and growth rate will be carried out with both Al_2O_3 and $MgAl_2O_4$ substrates. The nature of the autodoping mechanism will be explored using bulk Si wafers and Al_2O_3 and $MgAl_2O_4$ substrates as sources of dopant, in various gaseous atmospheres. Some further attention will be given to the effects on the properties of Si/Al_2O_3 films of gas flow patterns, reactor geometries, and temperature and gas flow-rate control. Studies of film nucleation phenomena in the Si/Al_2O_3 system will be resumed and additional deposition experiments at low pressures (≤ 0.1 torr) will be carried out especially to complement the in situ CVD experiments in the electron microscope (Subtask 5). A p-type doping capability for Si films on insulators will be developed so as to study multilayer film interfaces and permit fabrication of multi-layer device structures. Methods for optimizing the controlled doping of thin epitaxial layers of GaAs on insulators will be developed in order to prepare composite samples for other subtasks of the program, particularly those which involve device fabrication and evaluation.

92

3. SUBTASK 3. ANALYSIS AND PURIFICATION OF CVD REACTANTS

Analysis of CVD reactants for impurity content will be continued, primarily by mass spectrometric techniques. The efforts to obtain reactants of improved purity will continue, depending heavily upon cooperation from the vendors involved. The previously planned analysis of the impurity content of a series of Si and GaAs films as a function of distance from the film-substrate interface, as an indirect measure of the purity of the reactants used, will be carried out during this six-month period. The investigations of the basic chemistry involved in the formation of Si by SiH_4 pyrolysis and of GaAs by the trimethylgallium (TMG) - AsH_3 reaction at CSU San Diego will emphasize a study of the influence of Al_2O_3 surfaces on the mechanism of decomposition of SiH_4 and Si_2H_6 as a function of temperature and an examination of the decomposition modes and reaction products of TMG and AsH_3 as a function of temperature, concentration ratio, and H_2 partial pressure to determine the requirements for formation of optimum-quality GaAs.

4. SUBTASK 4. PREPARATION AND CHARACTERIZATION OF SUBSTRATES

Substrate surfaces of both Al_2O_3 and $MgAl_2O_4$ will be prepared for experimental use in the program using the best polishing and/or etching techniques developed to date. Additional effort will be devoted to improving the surface preparation techniques for both materials, with emphasis on chemical-mechanical polishing, liquid-phase etching procedures, and the use of annealing cycles in conjunction with liquid- and gas-phase etching procedures, for both Al_2O_3 and $MgAl_2O_4$. The effects of gas-phase etching of $MgAl_2O_4$ will be further examined and correlated with Si film growth characteristics and resultant film properties. Ion-beam sputtering will also be investigated as a means of removing damaged surface layers and contaminants from substrates prior to film deposition. The experiments with Rutherford backscattering of charged-particle beams, reflection electron diffraction, replica electron microscopy, and Auger electron spectroscopy will be continued in the attempt to correlate the properties of CVD Si films on insulator substrates with the pre-deposition properties of the substrate surfaces.

The development of the ion-beam sputtering technique for preparing thin ($\sim$200Å) substrates of Al_2O_3 for the in situ CVD experiments of Subtask 5 will continue. The emphasis will be on producing more uniform thickness of the Al_2O_3 in the thinned regions to be used in the deposition experiments and on developing mechanical or other polishing or etching procedures which will have higher yield for the preparation of the pre-ion-thinning substrates of thickness the order of 0.001 in. or less.

5. SUBTASK 5. STUDIES OF IN SITU FILM GROWTH IN THE ELECTRON MICROSCOPE

The CVD microchamber will be installed and tested early in the coming six months; upon completion of the focus, resolution, alignment, heating and gas-flow tests, the initial CVD experiments will begin. The first in situ work will concentrate on the temperature and substrate orientation variables of the Si CVD process based on SiH_4 pyrolysis; the effect of SiH_4 gas pressure will be examined later. The nucleation and early-stage growth processes will be studied to determine the mechanism whereby structural defects are incorporated into the growing film. Improvements in the CVD microchamber and the motion picture recording system will be made

as required. It is anticipated that numerous changes will be made in the experimental apparatus and the procedures used as the work progresses; this period of exploratory work will probably occupy the entire six-month period.

6. SUBTASK 6. EVALUATION OF FILM PROPERTIES

The routine evaluation of the structural and electrical properties of Si and GaAs heteroepitaxial films will be continued by means of various methods of X-ray and electron diffraction analysis, metallographic analysis, and measurement of both fundamental and device-related electrical properties. Rutherford backscattering analysis using charged particle beams will be continued for establishing the depth and density of defects in the films and the results correlated with characteristics of the substrates used to grow the films.

Studies of the anisotropy in electrical properties in the Si/Al_2O_3 system will be continued with emphasis on Si films grown on or near the (111) orientation. In addition, further studies will be made of films having orientations near the (100) Si plane. Low-temperature studies of the electrical properties of Si/Al_2O_3 will be resumed and compared with similar studies to be undertaken on the $Si/MgAl_2O_4$ system, using both n- and p-type films. Attempts will be made to identify experimentally the stress conditions in these films using X-ray techniques. The comparison of the properties of Si films on Al_2O_3 and $MgAl_2O_4$ substrates will continue so that the goal of selecting the preferred substrate species for optimized properties in the Si/insulator system can be realized.

Measurements of the escape length in Si and GaAs films are to be completed. Studies of transient internal photoemission and the charge transport properties in Al_2O_3 at various temperatures will be continued. Observations will be made of the effect of various annealing treatments on the photoinjection properties measured in Al_2O_3 - based systems. In addition, the photoelectric current in these same configurations will be measured at very low electric fields. Finally, the high-field transport properties in both Si and GaAs will be measured as a function of temperature, film resistivity and thickness, and crystallographic orientation.

7. SUBTASK 7. DESIGN AND FABRICATION OF DEVICES

Determination of carrier lifetimes in Si and GaAs films on both Al_2O_3 and $MgAl_2O_4$ substrates by the MOS pulsed C-V techniques will be continued. Systematic measurements will be made of lifetime as a function of film thickness, resistivity, and crystallographic orientation; attempts will also be made to observe lifetime dependence on temperature of measurement. The variation of the properties of simple junction diodes, MOS structures, and FET's with conditions of growth of the films will be used as a measure of film quality. Comparison device structures will be made and evaluated in the Si/Al_2O_3 and $Si/MgAl_2O_4$ systems to help select the preferred substrate for optimized Si film properties. The Schottky-barrier FET fabrication experiments will continue in $GaAs/Al_2O_3$ and $GaAs/MgAl_2O_4$ structures; following successful fabrication and appropriate evaluation of these devices at ~1GHz (design frequency), attempts will be made to extend the operation into the microwave region. Some attention will also be given to the fabrication of other special experimental device structures to be used to characterize heteroepitaxial film quality and utilize the unique properties of these films.

94

SECTION IV

PROGRAM SUMMARY TO DATE

The overall objective of the program, for which this is the Fourth Semiannual Report, is to carry out a fundamental study of the nucleation and film growth mechanisms in heteroepitaxial semiconductor thin films, leading to new knowledge and understanding of these processes, and then to apply these results to the preparation of improved semiconductor thin films and thin-film devices on insulating substrates.

The specific technical objectives of the three-year program are the following:

1. Investigation of the many aspects of the mechanisms of heteroepitaxial film growth, to establish (through accumulation of basic knowledge) sets of technical guidelines for the preparation of better films which can then be applied to real situations.

2. Preparation of improved, high-quality, device-grade heteroepitaxial films of Si and GaAs on insulating substrates by chemical vapor deposition (CVD) methods.

3. Development of methods of characterizing heteroepitaxial films as to their suitability for subsequent device fabrication.

4. Design and fabrication of selected thin-film devices which take advantage of the unique properties of such films.

The general plan for accomplishing these objectives involves the study of the fundamentals of heteroepitaxial semiconductor film growth on insulating substrates, with specialized device fabrication used as a means of evaluating certain film properties (and thus as a measure of film quality as the program progresses) and as a means of exploiting those properties unique to heteroepitaxial semiconductor-insulator systems.

The determination of the fundamental mechanisms, properties, and processes to be investigated is based on extensive background knowledge of epitaxy and thin-film device difficulties encountered for many years in many laboratories. The problems under study are not restricted to those identified a priori; experimental and theoretical attention is shifted as needed as the program progresses.

The program involves both theoretical and experimental investigation of the nucleation and growth mechanisms of heteroepitaxial films in semiconductor-insulator systems. The theoretical studies consist of two types of activity: (1) direct interaction with the experimental program involving data analyses, suggestion of definitive experiments, and postulation of specific models to explain experimental observations, and (2) development of original contributions to the theory of heteroepitaxial growth, with the goal of generating significant advances in fundamental epitaxy theory.

The experimental investigations are also of two types: (1) fundamental explorations to delineate mechanisms and general empirical principles of the heteroepitaxial growth process, and (2) practical studies that accompany the fundamental investigations so that any new developments can be immediately applied to the improvement of semiconductor films and thin-film devices on insulating substrates.

95

The work has emphasized the CVD method of growing semiconductor thin films because of its importance in the semiconductor industry. Specifically, the program emphasis is on films of Si and GaAs and substrates of sapphire (Al_2O_3) and spinel ($MgAl_2O_4$). The initial emphasis has been on the Si-on-Al_2O_3 system, with increasing attention being given to the Si-on-$MgAl_2O_4$ and GaAs-on-Al_2O_3 systems. Si and GaAs have been chosen because of the preeminence of the former in the semiconductor industry and the high-frequency and high-temperature attributes of the latter.

The program is carried on primarily at the facilities of the North American Rockwell (NR) Electronics Group in Anaheim. Parts of three of the subtasks have been performed by personnel of the University of California at Los Angeles (UCLA), in the Department of Electrical Sciences and Engineering and in the Chemistry Department, and by personnel of the California State University, San Diego (CSUSD), by means of subcontracts from NR.

The accomplishments of the contract program to date are summarized by subtask as follows.

1. SUBTASK 1. THEORY OF EPITAXY AND HETEROEPITAXIAL INTERFACES

During the first year a formal theoretical method of replacing overgrowth atoms on a substrate with Gaussian mass distributions was further developed for those cases where the effective interatomic potential is known. The technique, applicable to irregular-shaped islands or films of finite extent, was applied to a simplified model to determine preferred orientation relationships from calculated film-substrate interaction energies. The method was not pursued further, however, because it was not sufficiently adaptable to real systems. Several other possible approaches to the theoretical modeling of heteroepitaxial systems were critically reviewed, including the Frank-Van der Merwe model, a Green's function/Wannier-function approach, a contrived potential-energy model, and the two-body interactomic potential method. It was concluded that most existing theories are inadequate for application to real systems.

The feasibility of a molecular orbital development of the heteroepitaxial interface was then investigated. However, it was determined infeasible to apply this technique in a manner directly relevant to heteroepitaxy, so the effort was terminated. The interatomic potential approach to heteroepitaxy was then reinstigated, with the goal being the computer simulation of growth of Si on Al_2O_3. Mechanical stability conditions for an Al_2O_3 lattice modeled with two-body potentials were investigated and determined to the depth required for the applications. Computer programming of the Al_2O_3 lattice energy and elastic constants was begun for use in determining appropriate empirical potentials required for modeling the Al_2O_3 lattice, a major requirement for modeling Si growth on Al_2O_3. In addition, the application of the electron-on-network theory to the problem of determing surface configurations and interfacial binding energies in heteroepitaxial systems where the surface structure is allowed to relax was investigated and for a time appeared promising for the real systems of interest.

During the past six months the theoretical studies have been devoted to three main areas: (1) modeling of the Si/Al_2O_3 system by means of interactomic potentials and computer simulation; (2) use of the electron-on-network technique to calculate work functions and surface double-layer potentials of monovalent metals (although this

method will not be pursued further for possible application to heteroepitaxial systems); and (3) calculations relating the mobility of Si films on Al_2O_3 to stress effects arising at the heteroepitaxial interface and caused by differential thermal contraction of film and substrate.

The modeling of the Al_2O_3 lattice has been carried out in terms of Morse potentials; only anion-anion and cation-anion potentials have been employed. These have been chosen to conform to specific constraints related to the physical lattice. Investigation of surface reconstruction in basal-plane Al_2O_3 has also been initiated, using these potentials, since this phenomenon plays a major role in predicting Si film orientations on Al_2O_3.

The theoretically calculated changes in mobility and resistivity in the plane of the film in the Si/Al_2O_3 system caused by thermally induced stresses and the piezo-resistance effect have been found in excellent agreement with experimental results. Theoretical formulas have been developed for both Si and Ge and for Al_2O_3 and $MgAl_2O_4$ substrates and for a variety of crystallographic orientations.

2. SUBTASK 2. DEPOSITION STUDIES AND FILM PREPARATION

In the first year it was determined that the electrical properties of undoped n-type heteroepitaxial Si films grown on various orientations of Al_2O_3 (and also $MgAl_2O_4$) by the CVD method of pyrolysis of SiH_4 are dominated by surface-state conduction for carrier concentrations of $\sim 10^{15}$ cm^{-3} or below. Essentially equivalent (100)- and (111)-oriented Si films were grown on $(01\bar{1}2)$ and $(10\bar{1}4)$ Al_2O_3 substrates at deposition temperatures below the autodoping range (~ 1050 C). Al_2O_3 orientations near the $(11\bar{2}0)$ plane, not previously used in heteroepitaxy studies, were utilized as substrates for (111) Si heteroepitaxy; this resulted in electron mobilities of 600-700 cm^2/V-sec for carrier concentrations of $10^{15} - 10^{17}$ cm^{-3}, which exceeds mobilities obtained on either $(01\bar{1}2)$ or $(10\bar{1}4)$ Al_2O_3 substrates.

Analysis of the data revealed the strong interrelationships that exist among the various parameters considered as most meaningful for optimizing Si growth on insulators. Evaluation of the electrical properties of Si films on those Al_2O_3 orientations recognized years ago as providing reflective Si overgrowths has demonstrated that growth conditions (1) must be maximized for the substrate orientation chosen; (2) differ for those Al_2O_3 orientations which lead to the same Si orientation; (3) are dependent upon reactor geometry and gaseous atmosphere; and (4) should be optimized for the particular film thickness desired. Preliminary studies of Si growth by SiH_4 pyrolysis at reduced pressures (1 to 10 torr) have been very encouraging, indicating single-crystal growth can be obtained over a fairly wide temperature range, when conditions are optimized, on both Al_2O_3 and $MgAl_2O_4$ substrates. Investigation of the growth of Si films on Al_2O_3 and $MgAl_2O_4$ using He as the growth atmosphere and the carrier gas showed that epitaxial growth could be achieved, but the conditions for good quality growth remain to be established.

The effort on this subtask in the past six months was concentrated on continuing attempts to optimize the Si deposition process for growth on $\sim (11\bar{2}0)$ and $(01\bar{1}2)$ Al_2O_3 surfaces. In the couse of this work the effects of post-nucleation annealing during the deposition process on ultimate film properties have been examined, but no significant

97

improvement in overall quality of Si films resulting from these procedures has been demonstrated. The effects on film growth of gas-phase etching of Al_2O_3 surfaces prior to deposition have been evaluated further; there is some indication that surface damage may not be the primary factor in determining the quality of Si overgrowths, and this question is being examined in more detail. The effect of cooled reactor chamber walls on the Si growth process has also been investigated further, but no significant advantage of cooled walls in the vertical reactor systems used in this work has been observed. Considerable additional study has been made of the growth and properties of Si films on Czochralski-grown stoichiometric spinel ($MgAl_2O_4$). This work has indicated that Si films with electrical properties at least as good as those grown on Al_2O_3 can be obtained when $He-H_2$ gas mixtures are used for the growth environment. It has also been determined that autodoping is operative in the Si/ $MgAl_2O_4$ system (in $He-H_2$ atmospheres) at approximately the same temperatures as for Si/Al_2O_3.

3. SUBTASK 3. ANALYSIS AND PURIFICATION OF CVD REACTANTS

During the first year, techniques of gas chromatography were developed for analysis of the reactants used for semiconductor heteroepitaxy by CVD. A general-purpose gas-handling system was constructed for the highly volatile and reactive gases studied, with silicone oil and polymer columns used for the chromatography. Several extraneous impurity peaks were observed in the chromatograms of SiH_4 samples; diborane (B_2H_6) was tentatively identified as a significant impurity (~10 ppm), although not confirmed by mass spectrometer techniques. Small quantities of purified SiH_4, free of diborane, were prepared by successive injections in the chromatograph; quantities were too small, however, for use in laboratory CVD experiments.

Beginning in the second year of the program samples of SiH_4 and of trimethyl-gallium (TMG) used for Si and GaAs CVD experiments were analyzed for impurity content by sensitive mass spectrometric techniques. Disilane and trimethylsilane, together with several other impurities of less concern, were found in the SiH_4 samples. The analyses of TMG left some uncertainties regarding the actual impurity levels, and these are not yet fully resolved.

In the final half of the second year additional reactant analyses have been carried out by mass spectrometric techniques. Significant impurity concentrations in some of the reactants (especially SiH_4) have severely limited the accuracy of the study of the effects of deposition parameters on Si film properties on several occasions during this period. Cooperative efforts with vendors for preparation and analysis of improved-purity reactants have continued.

A significant new study of the chemistry and reaction kinetics of CVD processes used for growing Si and GaAs films in heteroepitaxial systems has been initiated; the first experiments undertaken are directed toward determining the role of the Al_2O_3 surface in catalyzing the pyrolysis of SiH_4. Other experiments with the trimethylgallium (TMG)-arsine (AsH_3) reaction used for GaAs growth will also be performed.

98

4. SUBTASK 4. PREPARATION AND CHARACTERIZATION OF SUBSTRATES

In the first year of the program it was demonstrated that Al_2O_3 surfaces prepared by mechanical polishing techniques and used routinely for semiconductor heteroepitaxy typically have severe surface and subsurface damage, with many scratches often several microns deep yet often rendered invisible to close inspection because of amorphous or fine-grained debris embedded in the scratches in the final polishing stages. Some improvement in mechanical polishing procedures was achieved in terms of the density and depth of such damage. Gas-phase etching/polishing procedures using SF_6 and various fluorinated halocarbons in the 1350 to 1500 C temperature range produced essentially scratch-free surfaces on $(01\bar{1}2)$ and near-$(11\bar{2}0)$ Al_2O_3 substrates. Extensive gas-phase etch rate data were obtained as a function of crystallographic orientation in this temperature range.

During the first part of the second year a much improved technique for polishing $(10\bar{1}4)$ Al_2O_3 was developed, and excellent surfaces in this orientation can now be obtained. Gas-phase etching/polishing techniques were further developed and exploited for (1) thinning Al_2O_3 substrates to thicknesses the order of 1 mil; (2) evaluating the effects of prolonged etching on $(01\bar{1}2)$, (0001), and $\sim(11\bar{2}0)$ Al_2O_3; and (3) assessing the subsurface damage caused by various mechanical polishing procedures. Routine characterization of substrate surfaces at various stages of preparation continued with techniques of X-ray and electron diffraction analysis, optical and electron microscopy, and charged-particle back-scattering measurements.

The most recent work on this subtask has involved verification of the improved polishing procedure for $(10\bar{1}4)$ Al_2O_3 as a reproducible process. Evaluation of polishing methods for $MgAl_2O_4$ surfaces has indicated that surface fill-in occurs for this material just as for Al_2O_3. Gas-phase etching experiments with $MgAl_2O_4$ surfaces have been initiated. Ion-beam sputtering techniques have been developed for preparing ultra-thin $(\sim200\text{Å})$ Al_2O_3 wafers for use as substrates in the in situ CVD experiments with Si. Wafers successfully thinned to ~0.002 in. by mechanical polishing techniques have been subsequently thinned by ion etching to the point of perforation in some areas, which results in adjoining regions of thicknesses suitable for transmission electron microscopy as applied in the in situ experiments. Typical thinning rates are 0.1 to 2.0 $\mu m/hr$. Three different Al_2O_3 orientations have been successfully thinned by this method – (0001), $(10\bar{1}4)$, and $(01\bar{1}2)$. Considerable study of properties of the resulting thinned substrates has been carried out and is discussed in detail.

5. SUBTASK 5. STUDIES OF IN SITU FILM GROWTH IN THE ELECTRON MICROSCOPE

In the first year of the program many of the modifications required in the electron microscope for in situ observation of the nucleation and early-stage growth of CVD semiconductor films on insulating substrates were completed. Provision for motion-picture recording of film growth was assembled and tested, and the heated specimen stage was installed and tested. The first in situ PVD experiments were also carried out near the end of the first year.

During the first six months of the second year a series of electron microscope modifications and tests was completed, culminating in a series of successful PVD experiments inside the electron microscope. Aluminum was deposited onto a heated

99

carbon substrate and a sequence of micrographs taken during the growth process, demonstrating the feasibility of performing in situ nucleation and growth studies in this equipment.

A transmission phosphor screen (for the motion picture camera) was installed, permitting motion picture photography which does not interfere with the normal still photography. The auxiliary vacuum pumping system for the specimen chamber was fabricated, installed and tested. The basic vacuum system of the microscope itself was improved by addition of a cooled baffle, by polishing numerous O-ring grooves, and by thoroughly cleaning the microscope interior. A PVD source assembly was fabricated, installed and used in conjunction with the specimen heater to perform the above PVD experiments. Calculations and design for the CVD microchamber were also completed, and the fabrication of the microchamber and the differential pumping apertures was begun. Work was also begun on the production of thin (200 Å) Al_2O_3 crystals required as substrates for the in situ CVD studies.

In the past six months the modified design of the CVD microchamber and associated hardware has been completed and fabrication is essentially complete, with testing and the first CVD in situ experiments now planned for early in the third-year program. Numerous in situ PVD experiments have been carried out, with both Al and Au deposited onto amorphous carbon substrates to delineate further the necessary techniques and experimental problems to be encountered in the CVD experiments. Extensive oxidation occurred with the Al films when grown at elevated temperatures, and unusual nucleation effects were observed in the portions of the Au films exposed to the electron beam; further experiments are in progress.

6. SUBTASK 6. EVALUATION OF FILM PROPERTIES

During the first year, the routine evaluation of film properties was carried out by establishing methods of X-ray and electron diffraction analysis, metallographic analysis, and electrical measurements of transport properties. In addition, a new technique for evaluating the characteristics of the interfacial region of heteroepitaxial films was developed, involving measurement of the photoelectron emission from monochromatically-illuminated films in the MIS configuration on insulating (viz., Al_2O_3) substrates. Relatively large photocurrents due to electron transport through thick (~10 mils) single-crystal Al_2O_3 substrates were measured as a function of photon energy. Photoelectric threshold energies, escape length (mean free path) of excited electrons, and band bending in the semiconductor film adjoining the interface were determined in the Si/Al_2O_3 and $GaAs/Al_2O_3$ systems. Observation of the energy spectrum of back-scattered proton or alpha-particle beams injected in channeling directions in heteroepitaxial semiconductor films was also investigated as a means of measuring the density and the location of structural defects in the films. Experiments indicated that Si/insulator films have less imperfect interfacial regions than do GaAs/insulator films. The best structures of those examined to date were found in (100) Si films on (01$\bar{1}$2) Al_2O_3 substrates and in (111)Si films grown on near-(11$\bar{2}$0) Al_2O_3 substrates.

In the first part of the second year the study of the effects of changes in deposition parameters on Si/Al_2O_3 film properties continued. These studies have led to considerable insight into the factors which most strongly influence film quality; identification of conditions for optimized film growth on various Al_2O_3 orientations appeared nearly complete. The importance of reactor geometry was recognized and demonstrated.

The extent of Al autodoping from the substrate was established, and appropriate annealing procedures for minimizing these effects were determined. The use of new Al_2O_3 substrate orientations for Si growth led to epitaxial films of as good or better quality than those previously obtained.

The measurements of photoemission of electrons from heteroepitaxial semiconductor films and of the transport of electrons in Al_2O_3 were carried further. Work functions of additional metals were determined, and the mechanism of electron transport through the insulator was studied further. Measurements of high-field transport properties of Si and GaAs heteroepitaxial films were initiated.

The evaluation work in the past six months has included (1) study of the variation of the electrical properties of Si/Al_2O_3 with temperature, in which some effects attributed to high defect densities or inhomogeneous strains were observed; (2) an extensive experimental study of the anisotropy of the electrical properties in Si/Al_2O_3; (3) evaluation of the electrical properties of Si films on $MgAl_2O_4$, with evidence that n-type films with mobilities higher than those obtained in the Si/Al_2O_3 system can be obtained; (4) additional measurements of the electrical properties of Si/Al_2O_3 to establish parametric relationships among temperature, growth rate, and substrate orientation; (5) further study of the photoelectric effects observed in the Si/Al_2O_3 system, particularly in the substrate material, including verification that the observed phenomena do result from photoinjection of electrons from metal films into the Al_2O_3 and determination of the work functions of several metals and the heights of the metal-Al_2O_3 interface barriers, and (6) measurement of the high-field transport properties of heteroepitaxial films.

The anisotropy studies have been concentrated in the $(221)Si/(11\bar{2}2)$ Al_2O_3 system and in the (100) $Si/(01\bar{1}2)$ Al_2O_3 system. The two Si planes are basically different in that the anisotropy in the (221) plane can be expected for any Si heteroepitaxial system, while that in the (100) Si plane results from the anisotropic thermal contraction of Al_2O_3 and would not be present, e.g., in the $Si/MgAl_2O_4$ system. The mobility anisotropy factor A, defined as the ratio of the difference between the maximum and minimum values of carrier mobility in the plane of the film to the average value of the mobility in that plane, was found to be about 39 percent for the (221) plane and about 9 percent for the (100) plane. Results of calculations based on the piezoresistance effect in Si resulting from the difference in the thermal expansion coefficients for Si and Al_2O_3 are given and agree well with the experimental data. The calculations and the experimental results also indicate that (221) Si probably exhibits higher electron mobilities than other more commonly used orientations. The results of the anisotropy studies are highly significant to preparation of device structures in heteroepitaxial semiconductor films.

7. SUBTASK 7 DESIGN AND FABRICATION OF DEVICES

In the first year of the contract apparatus for determining carrier lifetime by C-V measurement in MOS structures was designed and constructed and tests were begun. A special MOS structure was designed for measurement of channel conductance, high- and low-field transport properties, and various interface characteristics of heteroepitaxial films. Initial attempts to fabricate Schottky-barrier diodes in Si/Al_2O_3 films as a means of evaluating their electrical properties were not successful.

In the first half of the second year the preliminary design of a Schottky-barrier type of FET was completed, with experimental FET structures to be fabricated in GaAs/insulator films for operation at 1 GHz. Preliminary results on carrier lifetime in Si/Aℓ_2O$_3$ films were obtained, after initial development of the measurement technique on bulk single-crystal Si samples was completed and after impurity contamination problems encountered in the oxide growth process were solved.

During the past six months of the program the device-oriented effort has centered about the determination of carrier lifetimes using the MOS pulsed-capacitance technique and attempts to fabricate a Schottky-barrier FET in GaAs/Aℓ_2O$_3$. Processing defects have been encountered in both of these investigations, most of which are now resolved. An analysis was made to evaluate the effect of the impurity redistribution in the Si in the region near the oxide interface (resulting from the oxidation process used for making the MOS structures) on the interpretation of lifetime data obtained by this technique. Lifetime measurements in both Si and GaAs films as a function of film thickness, carrier concentration, and crystallographic orientation are being obtained.

REFERENCES

1. R. P. Ruth, "Fundamental Studies of Semiconductor Heteroepitaxy," First Semiannual Report, 28 January 1971, ARPA Order No. 1585, Contract No. DAAH01-70-C-1311. Prepared by North American Rockwell, Autonetics Division, Anaheim, CA, for USAMICOM, Redstone Arsenal, AL.

2. R. P. Ruth, "Fundamental Studies of Semiconductor Heteroepitaxy," Second Semiannual Report, July 1971, ARPA Order No. 1585, Contract No. DAAH01-70-C-1311. Prepared by North American Rockwell, Autonetics Division, Anaheim, CA, for USAMICOM, Redstone Arsenal, AL.

3. R. P. Ruth, "Fundamental Studies of Semiconductor Heteroepitaxy," Third Semiannual Report, January 1972, ARPA Order No. 1585, Contract No. DAAH01-70-C-1311. Prepared by North American Rockwell Electronics Group, Research and Technology Division, Anaheim, CA, for USAMICOM, Redstone Arsenal, AL.

4. R. A. Swalin, J. Phys. Chem. Solids $\underline{18}$, 290 (1961).

5. J. H. Gieske and G. R. Barsch, Phys. Stat. Sol. $\underline{29}$, 121 (1968).

6. O. L. Anderson, in Physical Acoustics, ed. by W. P. Mason, Vol. III, Part B (Academic Press, Inc., New York, 1965), p. 43.

7. C. C. Chang, J. Appl. Phys. $\underline{39}$, 5570 (1968); J. Vac. Sci. Tech. $\underline{8}$, 500 (1971).

8. P. A. Tick and A. F. Witt, Surface Sci. $\underline{26}$, 165 (1971).

9. E. W. Montroll, J. Math. Phys. $\underline{11}$, 635 (1970); with R. G. J. Mills, 2525 (1970).

10. A. C. Thorsen and A. J. Hughes, Paper No. 146, Second National Conference on Crystal Growth, Princeton, NJ, July-August 1972.

11. A. C. Thorsen and A. J. Hughes (Appl. Phys. Letters, to be submitted for publication).

12. H. Schlötterer, Sol. St. Electronics $\underline{11}$, 947 (1968).

13. F. J. Morin and J. P. Maita, Phys. Rev. $\underline{96}$, 28 (1954).

14. H. F. Mataré, private communication.

15. S. M. Sze, Physics of Semiconductor Devices (Wiley, N.Y., 1969), p. 469.

16. W. Pong, J. Appl. Phys. $\underline{40}$, 1733 (1969).

17. N. Szydlo and R. Poirier, J. Appl. Phys. $\underline{42}$, 4880 (1971).

18. C. R. Viswanathan and R. Y. Loo, International Conference on Thin Films, Venice, Italy, May 15-19, 1972.

19. J. Antula, J. Appl. Phys. 43, 1830 (1972).

20. M. Zerbst, Z. Angew. Phys. 22, 30 (1966).

21. F. P. Heiman, IEEE Trans. ED-24, 781 (1967).

22. G. H. Glover, IEEE Trans. ED-19, 138 (1972).

23. B. E. Deal, A. S. Grove, E. H. Snow, and C. T. Sah, J. Electrochem. Soc. 112, 308 (1965).

24. A. S. Grove, O. Leistiko, Jr., and C. T. Sah, J. Appl. Phys. 35, 2695 (1964).

25. W. Van Gelder and E. H. Nicollian, J. Electrochem. Soc. 118, 138 (1971).

APPENDIX I

WORK FUNCTIONS AND SURFACE DOUBLE LAYER POTENTIALS OF MONOVALENT METALS FROM A NETWORK MODEL*

ABSTRACT

The model described in this paper uses an electronic wave function which is defined to be nonzero only along the lines connecting first nearest neighbors in the metallic lattice. The electrons are assumed to move freely along the lines between nearest neighbors. No electron-electron or electron-nucleus force is included in the model calculations (except for forces arising from the Pauli exclusion principle). The work function is defined as the amount of energy required to move an electron from a point slightly inside the crystal to a point slightly outside. The contribution of the electronic double layer is included in the calculation of the work function as well as the dependence of the double layer potential on the surface geometry. Surface states, where the electron is localized in the neighborhood of the face of the crystal, are found to have energies sufficiently above the Fermi level to eliminate the possibility that they make any contribution to the double layer potential for the case of the (100) crystal plane. Consequently, surface states have been ignored in all the calculations. The surface double layer is assumed to be caused by the presence of a finite potential barrier at the surface of the crystal. Bulk electronic wave functions can penetrate this barrier and decay exponentially outside the crystal. The only parameters required by the model are the nearest neighbor distance for the lattice and the height of the potential barrier at the surface. The former quantity is fixed by the lattice structure (body centered cubic for the alkali metals) and by the density, while the latter quantity can be adjusted to give the best agreement between the model calculations and experiment. For the alkali metals, lithium through sodium, the best value of the barrier height is about 50 percent of the sum of the ionization potential energy, the heat of vaporization, and the calculated Fermi level for the corresponding metal. In addition, the value of the double layer potential for sodium agrees very well with a more sophisticated calculation by Bardeen and is reasonably close to the experimental measurement.

1. INTRODUCTION

The free electron molecular orbital method (FEMO) has been successfully applied by Kuhn (Ref 1) and by Rudenberg and Scherr (Ref 2) to the treatment of π-electron systems in conjugated molecular systems. As in the case of Hückel theory (Ref 3), the free electron orbital method is directed towards the development of a "relative" internally consistent theory for these complicated systems. In the case of Hückel theory, parameters such as overlap integrals are determined by experiment in one molecule and are assumed to have the same magnitude in others. Strictly speaking, in the FEMO method there are no adjustable parameters (unless the distances between atoms are allowed to depart from the values actually observed in the molecule). Nevertheless, both methods provide a reasonable semi-quantitative picture of the electronic state of affairs within π-systems, and have been useful for making semi-quantitative estimates concerning the chemical and spectroscopic properties of π-systems.

Recently Montroll and his coworkers (Ref 4) have expanded the FEMO method to include the treatment of local potentials due to individual atoms. The theory of course remains highly schematic, as well as parameterized, but it does allow relatively simple analytical solutions to be obtained for previously complicated problems. In this way, Montroll and his collaborators have been able to explore the qualitative features of many interesting solid state phenomena including the electronic properties of defects and surfaces. Since the original FEMO method proved useful in the semi-quantitative discussion of the electronic properties of molecules, it is interesting to see whether both the FEMO and Montroll's modification of it can be used in the semi-quantitative study of solids. We have in mind not only the examination of schematic relationships (Montroll and his collaborators have already done that), but also the development of an internally consistent parameterized theory in the same spirit as Hückel theory.

In order to study this question, we have elected to apply the network theory to the estimation of the work functions of monovalent metals, especially the alkalis. Our principal objective has been to determine the work function and its variation with crystal orientation. The approach is as simple as possible, involving a single adjustable parameter, namely the difference between the energy of a free electron in vacuum and the lowest level of the conduction band. This parameter is invariant to crystal orientation and could in principle be determined from measurements on a single crystal plane. All refinements, such as exchange and correlation effects, are explicitly ignored but should be implicitly involved within the barrier height which constitutes the adjustable parameter mentioned above. The detailed explicit treatment of these additional effects would be inconsistent with the severe approximations already contained within the theory. One would hope, however, that the network model would give a reasonable semi-quantitative account of the variation of work function with crystal orientation, once the adjustable parameter is determined, by using the experimental data available for one crystal plane. Furthermore, one would hope that there would be an orderly relationship between the predictions of the theory for one alkali metal as compared to another.

2. THE NETWORK MODEL

Our treatment actually makes use of the FEMO method coupled with the Green's function approach developed by Montroll for the treatment of defects and surfaces in connection with his more elaborate network model. The one electron wave function is chosen to be nonzero only along the lines connecting the first nearest neighbors in the metallic lattice. This is equivalent to requiring that the potential be infinite everywhere within the crystal except on these lines. The electrons are assumed to move freely, i.e., we do not associate potential wells (as in the Montroll modification) with the individual atoms. To this extent, our model is more like the original FEMO method. However, we shall have to make use of the Bloch theorem (Ref 5) in order to deal with the crystal and the Green's function approach will have to be used to treat the extended defect represented by the surface. The crystal symmetry enters the problem through the nodal conditions, Eq (11) and (12) below, and through the Bloch theorem.

The work function is defined as the amount of energy required to move an electron from the point slightly inside the crystal to a point slightly outside, and is effected by the electronic double layer (Ref 6) which in turn depends on crystal surface. One of our main tasks will involve calculating the strength of this double layer.

As long as an electron remains on a line joining two nearest neighbor atoms inside the lattice, it has no force acting on it, and its potential energy may be set equal to zero. We assume that an abrupt change in potential occurs as the electron moves on to a dangling surface bond where it experiences a constant potential V_B ($V_B > 0$). The surface barrier V_B is the only parameter in the theory and will have to be determined through reference to some single experiment. In fact, the form of the potential barrier in the real crystal is not abrupt, but since we are searching for the simplest possible parameterized theory (and also because of the severe approximation already contained within the network model itself), we assume that it is abrupt. The dangling bonds for surface atoms have the same direction as if they were joined to another lattice site; but instead of being of length R (where R is the nearest neighbor distance), they extend all the way to infinity. The wave equation for this system may be expressed in the following form:

$$\nabla^2 \psi - (\alpha^2 - k^2) \psi = 0, \tag{8}$$

in which $\alpha^2 = \dfrac{2mV}{\hbar^2}$, $k^2 = \dfrac{2mE}{\hbar^2}$ and ψ is the electronic wave function, m the mass of the electron, E the energy of the state described by ψ, V the potential, and $\hbar$ is Planck's constant divided by 2π. Clearly V (and α) equals zero for positions along bonds in the bulk, while $V = V_B$ on the dangling bonds. The solutions of Eq (8) for the surface and bulk bonds, respectively, are:

$$\psi_s = a_s \exp \left\{ - (\alpha^2 - k^2)^{1/2} x \right\}, \tag{9}$$

$$\psi_B = a_s \cos \left\{ kx + \delta_B \right\}. \tag{10}$$

Each ψ is defined only on a particular bond and is zero elsewhere. Where several bonds meet at a lattice point, the wave functions associated with them must be equal. In addition, there are requirements associated with the conservation of momentum. These restrictions may be expressed as follows: (Ref 2)

$$\psi_1 (o) = \psi_2 (o) = \psi_3 (o) = \ldots = \psi_n (o) \quad , \tag{11}$$

$$\sum_{i=1}^{n} \left(\frac{\partial \psi_i}{\partial x}\right)_{x=o} = 0 \; . \tag{12}$$

In these equations n is the number of bonds meeting at a particular lattice site.

If the quantity $\phi(\ell, m, n)$ is the value of the wave function at the lattice site (ℓ, m, n), Eq (11-12) require, for a body centered cubic lattice, the following relationship:

$$8 \cos (kR) \, \phi(\ell, m, n) = \phi(\ell+1, m+1, n+1) + \phi(\ell+1, m-1, n+1) + \phi(\ell-1, m+1, n+1)$$

$$+ \phi(\ell-1, m-1, n+1) + \phi(\ell+1, m+1, n-1) + \phi(\ell+1, m-1, n-1) + \phi(\ell-1, m+1, n-1)$$

$$+ \phi(\ell-1, m-1, n-1) \; . \tag{13}$$

In addition, for the bulk crystal we make use of periodic boundary conditions:

$$\phi(\ell m, n) = \phi(\ell, N, m, n) = \phi(\ell, m+N, n) = \phi(\ell, m, n+N) \; . \tag{14}$$

A possible solution to Eq (13) and (14), which also satisfies Bloch's theorem, is:

$$\phi(\ell, n, n) = A \exp\left\{\frac{2\pi i}{N} (\ell s_1 + m s_2 + n s_3)\right\} \quad , \tag{15}$$

where s_1, s_2, $s_3 = 1, 2, 3, \ldots N$. Substitution of Eq (15) into (13), with appropriate collection of terms, yields:

$$\cos (kR) = \cos \left(\frac{2\pi s_1}{N}\right) \cos \left(\frac{2\pi s_2}{N}\right) \cos \left(\frac{2\pi s_3}{N}\right) = E. \tag{16}$$

Since the energy of an electron depends on k, and s_1, s_2, and s_3 are indices denoting possible states of the system, Eq (16) determines the density of states for network. The density of sets (s_1, s_2, s_3), satisfying Eq (16) in the range dE, has been derived, in another context, by Jelitto (Ref 7) (see Figure 45). The density-of-states function is symmetric about $\cos (kR) = 0$, and it follows that the Fermi level of the network corresponds to an energy level such that $kR = \pi/2$. Therefore, the Fermi level is given by:

$$\mu_F = \frac{h^2}{32mR^2} \; . \tag{17}$$
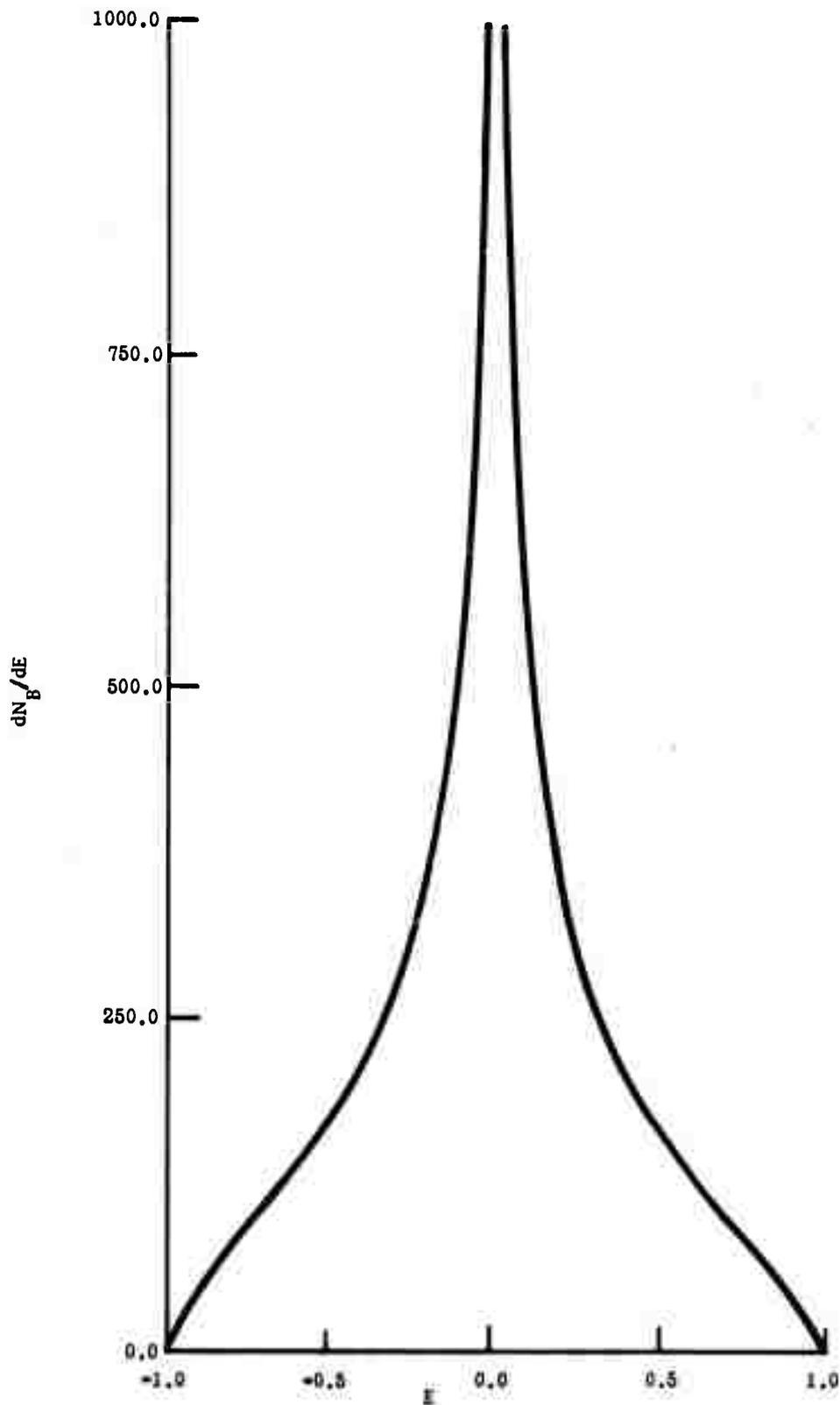
Figure 45. The Density of States, dN_B/dE, for a Body Centered Cubic Lattice Plotted as a Function of E, where E is Defined to be the Cosine of the Reduced Momentum Wave Vector, kR. (This graph is given by Jelitto, Ref 7)

In order to deal with surface states, we assume that the network is infinite in both the x and y directions, but has a finite thickness in the z direction. It is possible to write a general relationship (analogous to Eq (13)) which applies to either bulk or surface sites. Thus, we have:

$$8\cos\,(kR)\,\phi(\ell,m,n) - \phi(\ell+1,m+1,n+1) - \phi(\ell+1,m-1,n+1) - \phi(\ell-1,m+1,n+1)$$

$$- \phi(\ell-1,m-1,n+1) - \phi(\ell+1,m+1,n-1) - \phi(\ell+1,m-1,n-1) - \phi(\ell-1,m+1,n-1)$$

$$- \phi(\ell-1,m-1,n-1) = H\,(\ell,m,n)\,,\tag{18}$$

$$\phi(\ell+N,m,n) = \phi(\ell,m+N,n) = \phi(\ell,m,n)\,,\tag{19}$$

where

$$H\,(\ell,m,n) = [\delta_{n,1} + \delta_{n,N_Z}]\,[4\cos\,(kR) - 4A\,(kR)]\,\phi\,(\ell,m,n)$$

$$- \delta_{n,1}\,[\phi(\ell+1,m+1,N_Z) + \phi(\ell+1,m-1,N_Z) + \phi(\ell-1,m+1,N_Z) + \phi(\ell-1,m-1,N_Z)]$$

$$- \delta_{n,N_Z}\,[\phi(\ell+1,m+1,1) + \phi(\ell+1,m-1,1) + \phi(\ell-1,m+1,1) + \phi(\ell-1,m-1,1)$$

$$A\,(kR) = [\frac{(\alpha R)^2 - (kR)^2}{(kR)^2}]^{1/2}\,\sin\,(kR)$$

and the δ's are Kronecker delta functions. An equation of this general form was introduced by Montroll (Ref 3) although he did not specifically treat the case in which an abrupt barrier of finite height V_B was located at the surface. We assume that the z-direction is the [001] direction and that the exposed surfaces are (001) surfaces having coordinates $z = 1$ and $z = N_Z$, respectively.

Because of the finite extent of the crystal in the z direction, we can no longer demand that ϕ satisfy the Bloch theorem in that direction. However, this requirement may still be applied to the x and y directions. A solution to Eq (18), which satisfies the Bloch theorem in these directions, is:

$$\phi(\ell,m,n) = A\,\exp\left|\frac{2\pi i}{N}\,[s_1,\ell + s_2,m]\right|\,\phi\,(n)$$

$$s_1,\,s_2 = 1,\,2,\,3,\,\ldots N\,.\tag{20}$$

If we substitute this into Eq (18) and collect terms, the result is

$$2F_B\,\phi(n) - \phi(n+1) - \phi(n-1) = H_B\,(n)\,,\tag{21}$$

110

in which

$$H_B(n) = [\delta_{n,1} + \delta_{n,N_Z}] \eta \phi(n) - \delta_{n,1} \phi(N_Z) - \delta_{n,N_Z} \phi(1),$$

$$F_B = \cos(kR)/[\cos(\frac{2\pi s_1}{N}) \cos(\frac{2\pi s_2}{N})] \ ,$$

$$\eta = [\cos(kR) - A(kR)]/[\cos(\frac{2\pi s_1}{N}) \cos(\frac{2\pi s_2}{N})] \ .$$

A difference equation having the same form as Eq (21) has been solved by Montroll (Ref 4) using an appropriate Green's function, g(n). In terms of g, this solution may be expressed as:

$$\phi(n) = \sum_{j=1}^{N_z} (g(j-n) H_B(j) \ , \tag{22}$$

where the Green's function is defined as:

$$g(n) = \frac{1}{2N_Z} \sum_{\delta=1}^{N_Z} \frac{\exp\left|\frac{2\pi i s n}{N_Z}\right|}{F_B - \cos(\frac{2\pi s}{N_Z})} \ . \tag{23}$$

For the $|F_B| > 1$, $\phi(n)$ decays exponentially as n refers to sites further from the surface, i.e., deeper in the bulk of the crystal. Therefore, this range of F_B is the range for surface states; and by substitution of the solution in this range back into Eq (21), it may be shown that the following relation holds:

$$[\cos^2(kR) - A^2(kR)]^{1/2} = \cos(\frac{2\pi s_1}{N}) \cos(\frac{2\pi s_2}{N}). \tag{24}$$

This equation is, for surface states, the equivalent of Eq (16) for bulk states and, like Eq (16), determines the density of states.

The bulk wave functions may be normalized as follows. First, the square of the wave function (square of the modulus) is integrated over each individual bond, yielding a quantity proportional to the fraction of electrons residing on the bond. This fraction is then summed over all bonds and the sum is set equal to unity. The fact that each state is occupied by two electrons is then taken into account at a later step by multiplying the density of states function, Eq (29), by 2. The integral for the square of the wave function on a dangling surface bond is, according to Eq (9):

$$D_s = |\psi_s(o)|^2 \int_0^\infty \exp\{-2\beta x\} dx = \frac{|\psi_s(o)|^2}{2\beta}. \tag{25}$$

In the above equation, $\beta = (\alpha^2 - k^2)^{1/2}$ and $|\psi_s(0)|$ is the value of the wave function at the surface node. The integral for the square of the wave function on a bond connecting two nearest neighbor lattice sites is, from Eq (10):

$$D_B = \int_0^R \cos^2(kx + \delta_B) = 2\left\{R + \frac{\sin[2(kR + \delta_B)] - \sin[2\delta_B]}{2K}\right\}, \qquad (26)$$

where R is again the distance between nearest neighbors. It should be noted that although both the above integrals depend on the kinetic energy of the electron, D_s is also a function of the surface barrier height, while D_B is a function of the distance R. In a body centered cubic lattice, each site has eight first nearest neighbors and therefore eight radiating bonds. However, for interior sites, each of these eight bonds is shared by one other lattice site and thus each interior site has only four bonds on the average.

In accordance with the prescription laid out above, we therefore write the following expression:

$$4D_B |a_B|^2 N^3 + \ldots + 0(N^2) = 1, \qquad (27)$$

where N^3 is the number of sites in the lattice and N^2 is proportional to the number of surface sites. All terms on the left of Eq (27), except the first, are of order N^2 or less; and since the size of the network can be thought of as being arbitrarily large, only the cubic term needs to be considered. Consequently, the following expression is obtained:

$$|\alpha_B|^2 = \frac{1}{4D_E N^3}. \qquad (28)$$

It turns out that for reasonable values of the barrier height, V_B, surface states on the (001) plane have energies above the Fermi level and are consequently unoccupied. As a result, surface states do not influence the surface double layer potential or the work function, at least not within the requirements of the network model. Thus, the properties of the surface states need not be included in the calculations for the double layer and work function which follow. We can therefore make full use of the density of states derivable by the method of Jelitto (Ref 7).

This density of states in reduced momentum space is:

$$\rho(kR) = C_N \sin(kR) \frac{dN_B}{dE}, \qquad (29)$$

where dN_B/dE has been expressed rigorously by Jelitto in terms of elliptic integrals. It may also be approximated using more elementary functions as follows:

$$\frac{dN_B}{dE} \approx 2[1 - |E|]^{1/2} \left[\ln\left(\frac{5.845}{|E|}\right)\right]^2 \left[16.679 + 3.6364 \cdot |E| + 2.4880 \cdot |E|^2\right];$$

112

an expression good to four significant figures over the range $0.005 \leq |E| \leq 1.0$. $E = \cos(kR)$ and C_N is a normalizing constant such that the total number of quantities in the region $0 \leq kR \leq \pi$ is N^3, i.e.,

$$\int_0^\pi \rho(kR)\, d(kR) = N^3.$$

Because the expression for $\rho(kR)$ is rather complicated, the above integral is evaluated most conveniently by numerical means. Unfortunately, the value of dN_B/dE is infinite for $|E| = 0$, and the numerical integration cannot be performed over the entire integral even though the integral converges. The density of states function, $\rho(kR)$, is symmetric on the integral about the point $kR = \pi/2$, and consequently the numerical integrations need only be performed from $kR = 0$ to $kR = u$, where $u < \pi/2$. There will be some uncertainty about the exact value of C_N, depending on the choice of upper limit for the integral. For the calculations in this paper, u has been set equal to 0.4985π. This particular value was chosen for two reasons: (1) the approximation for dN_B/dE is known to be reasonably accurate over this range of integration, and (2) the value of C_N differs by only a few percent from the value assumed when the upper limit on the integral is changed from 0.4985π to 0.49999π.

3. ESTIMATION OF SURFACE CHARGE

The charge on each dangling surface bond may be calculated in a straightforward manner, being proportional to D_S. Multiplying this ratio by 2 to account for electron spin and finally integrating over all states (all possible values of momentum) gives the fraction of the total number of electrons residing on a surface bond. We call this quantity $G(\alpha R)$:

$$G(\alpha R) = \int_0^{\pi/2} 2\rho(kR)\, D_S\, d(kR) = \int_0^{\pi/2} \frac{\dfrac{\cos^2(\delta_B)}{\left[(\alpha R)^2 - (kR)^2\right]^{1/2}}\left(\dfrac{\rho(kR)}{2N^3}\right)}{1 + \dfrac{\sin[2(kR+\delta_B)] - \sin[2\delta_B]}{2kR}}\, d(kR). \qquad (30)$$

In this equation, D_S and D_B are defined by Eq (25) and (26), respectively, and:

$$\tan(\delta_B) = \frac{\cos(kR) - 1}{\sin(kR)}$$

$$|\psi_s(0)|^2 = |a_B|^2 \cos^2(\delta_B).$$

These two relations are derived from the requirement that the square of the modulus of the standing waves represented by Eq (9-10) must be the same at all lattice sites for wave functions associated with the bulk energy states.

113

Because of the difficulties already discussed in connection with ρ(kR), the actual upper limit of integration used in these calculations was 0.4985π instead of $\pi/2$. The bulk wave functions are assumed to differ only by a phase factor from one lattice site to another even at the surface. Because G(αR) is normally a few tenths of an electron or less, and because the conductivity of the metal is high, all the positive charge, balancing the negative charge located outside the lattice, is assumed to reside on the crystal surface. The total positive surface charge is therefore:

$$\sigma_s = \frac{1}{4} n_s \, G(\alpha R) \left(\frac{N_s}{A_s} \right) e, \tag{31}$$

where n_s is the number of dangling surface bonds and (N_s/A_s) is the number of sites per unit area, while e is the charge on an electron.

4. CALCULATION OF THE DOUBLE LAYER POTENTIAL

The work required to move an electron from the surface to some point outside the crystal may be calculated using Gauss' theorem. Since the distribution of electric charge is uniform parallel to the crystal surface, the field acting on any electron is perpendicular to the surface and has an intensity:

$$E(x) = \frac{\sigma(x)}{\epsilon_0}, \tag{32}$$

where $\epsilon_0 = 1.811 \times 10^{-8}$ coulombs/Newton/meter^2 and $\sigma(x)$ is the net amount of positive charge lying between the surface and the point x on the dangling bonds. The charge $\sigma(x)$ is evaluated from the expression:

$$\sigma(x) = \frac{n_s}{2N^3} \int_0^{\pi/2} \frac{\dfrac{\cos^2(\delta_B) \exp\{-2\beta x\}}{\left[(\alpha R)^2 - (kR)^2\right]^{1/2}}}{1 + \dfrac{\sin\left[2(kR+\delta_B)\right] - \sin\left[2\delta_B\right]}{2kR}} \tag{33}$$

in which we have combined Eq (30) with (9). The work performed against the double layer is then:

$$W_D = K_G \int_0^\infty E(\ell) \, d\ell \tag{34}$$

In this equation, $d\ell$ represents distance along the direction of the surface bond, and K_G is a factor such that $K_G d\ell$ is the distance normal to the surface. The integral in Eq (34) is most conveniently evaluated in terms of the reduced distance ℓ/R, and the exact value of the upper limit is not very important because essentially all of the contribution to the double layer potential occurs within less than five times the nearest neighbor spacing from the surface. Thus, within the limitations of this model, changes in the double layer potential from one surface to another are determined by

114

the variations in three factors: (1) the number of lattice sites per unit area of surface, (2) the number of dangling surface bonds at each site, and (3) the geometric factor K_G.

5. THE WORK FUNCTION

As indicated earlier, the work function is defined as work necessary to move an electron from the point just inside the lattice to a point just outside. The energy required for this process depends on the geometry of the surface through which the electron passes because of the contribution of the double layer. In keeping with the simplicity of the network model, the work function W_E is defined as:

$$W_E = V_B - \mu_F - W_D ; \tag{35}$$

whereas before V_B is the surface barrier, μ_F is the Fermi level, and now we denote the double layer potential by W_D. The first two quantities on the right of Eq (35) are independent of surface orientation, and the variation of work functions with surface is therefore due to W_D.

The double layer potential, Eq (34), can be expressed most conveniently in the following form:

$$W_D(\alpha R) = A_L I(\alpha R) \tag{36}$$

where

$$A_L = K_G R \left(\frac{n_s}{4} \right) \left(\frac{e}{\epsilon_o} \right) \left(\frac{N_s}{A_s} \right).$$

and is only a function of the nearest neighbor distance and surface geometry, while $I(\alpha R)$ is an integral which depends only on the product αR. The values of $I(\alpha R)$ for various αR have been listed in Table XIX. In Table XX, the densities of the alkali metals and their first nearest neighbor distances are given, as well as the values of A_L for the (001) and (011) planes.

The surface barrier V_B may be estimated by the following expression:

$$V_B \approx I + H + \mu_F . \tag{37}$$

Here I is the ionization potential for an atom in gas phase, H is the heat of sublimation per atom, and μ_F the Fermi level which can be estimated from Eq (17). Equation (37) approximates an equation given by Bardeen (Ref. 8) and has its origin in comparing certain electronic integrals which occur in the expression for V_B with integrals which also occur in expressions for I and II. The barrier height may also be estimated by adjusting V_B so that the value predicted by the network theory agrees with experiment. This was done for the alkali metals using the work function calculated for the (001) plane. The experimental heats of vaporization, ionization potentials, and work functions have been compiled from various sources by Wigner and Bardeen (Ref. 6).

115

TABLE XIX

αR	$I(\alpha R)$
0.6	0.10553
0.7	0.05890
0.8	0.03944
0.9	0.02879
1.0	0.02215
1.1	0.01765
1.2	0.01447
1.3	0.01207
1.4	0.01025
1.5	0.00882
1.6	0.00767

TABLE XX

Element	Density (gm/cm^3)	Nearest Neighbor Distance $(\overset{\circ}{A})$	A_L (001)	A_L (001)
Lithium	0.534	3.038	25.82	18.26
Sodium	1.007	3.666	21.39	15.12
Potassium	0.870	4.594	17.08	12.07
Rubidium	1.532	4.937	15.88	11.23
Cesium	1.873	5.349	14.67	10.37

In Table XXI, we compare the barrier heights estimated from Eq (37) with those obtained through adjustment of V_B to make the work function calculated by the network model agree with experiment. The best fit value obtained from the network model is always about one-half the value derived from Eq (37). On the other hand, Eq (37) is itself by no means precise. Considering the simplicity of the network model, the results are not very disparate. In fact, in the case of both Hückel theory and the FEMO method applied to molecules, the same order of magnitude is observed for the mismatch between theory and experiment.

Also included in Table XXI are double layer potentials for two different surfaces. Bardeen, (Ref. 8) using the free electron model, calculates that the surface double layer for the (110) plane of sodium is 0.4 volt. The network model predicts a value of 0.37 volt (using the value of V_B which brings the theoretical and experimental work functions into register) as compared with an experimental value (Ref. 8) of 0.15 volt.

From these results, it appears as though the simple network model possesses about the same quantitative degree of validity with respect to surface state problems that the FEMO model possesses with respect to molecules. This suggests that it may be used to make ballpark estimates in a variety of solid state situations.

TABLE XXI

Element	αR	V_B (volts)	μ_F (volts)	$\phi_{(001)}$ (volts)	$D_{(001)}$ (volts)	$\phi_{(001)}$ (volts)	$D_{(011)}$ (volts)	$I+H+\mu_F$ (volts)	$\dfrac{V_B}{I+H+\mu_F}$
Lithium	0.979	0.3903	1.018	2.310	0.575	2.479	0.406	8.06	0.484
Sodium	1.107	0.3426	0.699	2.355	0.372	2.464	0.263	6.95	0.493
Potassium	1.271	0.2876	0.445	2.214	0.217	2.230	0.153	5.72	0.503
Rubidium	1.334	0.2743	0.385	2.177	0.181	2.230	0.128	5.42	0.506
Cesium	1.344	0.2373	0.328	1.881	0.164	1.929	0.116	5.03	0.472

REFERENCES

[1] H. Kuhn, Helv. Chim. Act. $\underline{31}$, 1441 (1948); J. Chem. Phys. $\underline{18}$, 840 (1948); Ibid., $\underline{22}$, 2098 (1954).

[2] K. Ruedenberg and C. W. Scherr, J. Chem. Phys. $\underline{21}$, 1565 (1953); C. W. Scherr, J. Chem. Phys. $\underline{21}$, 1582 (1953).

[3] C. A. Coulson and H. C. Longuet-Higgens, Proc. Roy. Soc. (London) $\underline{A191}$, 39 (1947).

[4] E. W. Montroll, J. Math. Phys. $\underline{11}$, 635 (1970); R. G. J. Mills and E. W. Montroll, J. Math. Phys. $\underline{11}$, 2525 (1970); E. W. Montroll, private communication to be published.

[5] J. Callaway, Energy Band Theory (Academic Press, New York 1965).

[6] E. Wigner and J. Bardeen, Phys. Rev. $\underline{48}$, 84 (1935).

[7] R. J. Jelitto, J. Phys. Chem. Solids $\underline{30}$, 609 (1969).

[8] J. Bardeen, Phys. Rev. $\underline{49}$, 653 (1936).